AD-A155 259 AN INVESTIGATION INTO THE FLUIDIZATION AND HEAT TRANSFER OF LOW DENSITY P.. (U) ARMY MILITARY PERSONNEL CENTER ALEXANDRIA VA J M MODLIN 10 MAY 85 1/2

UNCLASSIFIED F/G 10/1 NL

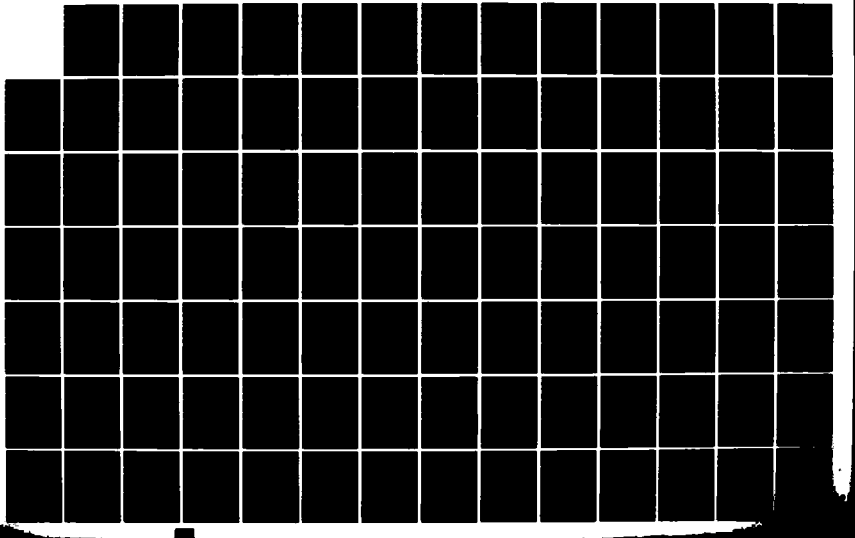

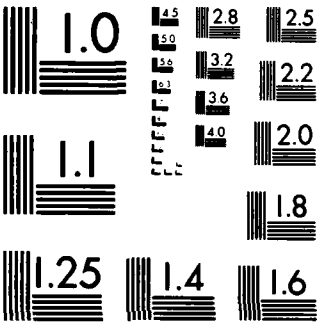

An Investigation Into the Fluidization and Heat Transfer of Low Density Particles in a Fluidized Bed with Applications

CPT James M. Modlin
HQDA, MILPERCEN (DAPC-OPA-E)
200 Stovall Street
Alexandria, VA 22332

Final Report 10 May 1985

A thesis submitted to the Massachusetts Institute of Technology in partial fulfillment of the requirements for the degrees of Mechanical Engineer and Master of Science in Mechanical Engineering.

SECURITY CLASSIFICATION OF THIS PAGE *(When Data Entered)*

REPORT DOCUMENTATION PAGE

READ INSTRUCTIONS BEFORE COMPLETING FORM

1. REPORT NUMBER	2. GOVT ACCESSION NO. / 3. RECIPIENT'S CATALOG NUMBER
4. TITLE *(and Subtitle)*: An Investigation Into the Fluidization and Heat Transfer of Low Density Particles in a Fluidized Bed with Applications.	5. TYPE OF REPORT & PERIOD COVERED: Final Report 10 May 85
	6. PERFORMING ORG. REPORT NUMBER
7. AUTHOR(s): CPT James M. Modlin	8. CONTRACT OR GRANT NUMBER(s)
9. PERFORMING ORGANIZATION NAME AND ADDRESS: Student, HQDA, MILPERCEN (DAPC-OPA-E) 200 Stovall Street Alexandria, Virginia 22332	10. PROGRAM ELEMENT, PROJECT, TASK AREA & WORK UNIT NUMBERS
11. CONTROLLING OFFICE NAME AND ADDRESS: HQDA, MILPERCEN, ATTN: DAPC-OPA-E 200 Stovall Street Alexandria, Virginia 22332	12. REPORT DATE: 10 May 1985
	13. NUMBER OF PAGES: 180
14. MONITORING AGENCY NAME & ADDRESS *(if different from Controlling Office)*	15. SECURITY CLASS. *(of this report)*: UNCLAS
	15a. DECLASSIFICATION DOWNGRADING SCHEDULE

16. DISTRIBUTION STATEMENT *(of this Report)*

Approved for public release; distribution unlimited.

17. DISTRIBUTION STATEMENT *(of the abstract entered in Block 20, if different from Report)*

18. SUPPLEMENTARY NOTES

Report is a graduate thesis submitted to the Department of Mechanical Engineering at the Massachusetts Institute of Technology.

19. KEY WORDS *(Continue on reverse side if necessary and identify by block number)*

Fluidization, Heat Transfer, Fluidized Bed, Solar Collector, Efficient Building Energy Management

20. ABSTRACT *(Continue on reverse side if necessary and identify by block number)*

The lack of reliable data on the fluidization and heat transfer characteristics of low density particles in a fluidized bed has prompted an experimental and analytical investigation into this subject. Seven groups of particles have been successfully fluidized and have been shown to be generally well predicted by existing theory.

(continued on next page)

DD FORM 1 JAN 73 1473 EDITION OF 1 NOV 65 IS OBSOLETE

SECURITY CLASSIFICATION OF THIS PAGE *(When Data Entered)*

20. (cont.)

Using the experimental data and results as a basic of analysis, two applications of low density particle fluidization in a building efficient energy management program are discussed. A fluidized bed can be incorporated into the wall cavity of a building for use as either a collector of solar energy or as a heat exchange medium in a building space heating/cooling program. As a solar collector, it is shown that the low density particle fluidized bed would thermally perform between comparable conventional liquid and air-cooled flat plate solar collectors. It would require less water pumping power than the liquid collector and less air pumping power than the air collector.

As a heat exchanger, the low density particle fluidized bed would function in a building space comfort control capacity by providing a large wall surface area available for heat transfer to or from the space. It is shown that this rate of heat transfer provided by the fluidized bed is significantly greater than what is available for air alone flowing over the surface and at reduced air pumping power requirements.

AN INVESTIGATION INTO THE FLUIDIZATION AND HEAT TRANSFER OF LOW DENSITY PARTICLES IN A FLUIDIZED BED WITH APPLICATIONS

by

JAMES MICHAEL MODLIN

B.S., United States Military Academy
(1977)

Submitted to the Department of
Mechanical Engineering
in Partial Fulfillment of the
Requirements for the
Degrees of

MECHANICAL ENGINEER

and

MASTER OF SCIENCE in MECHANICAL ENGINEERING

at the

MASSACHUSETTS INSTITUTE OF TECHNOLOGY

May 1985

Signature of Author James M. Modlin
Department of Mechanical Engineering
May 10, 1985

Certified by Leon R. Glicksman
Leon R. Glicksman
Thesis Supervisor

Accepted by
Ain A.Sonin
Chairman, Mechanical Engineering Department Committee

AN INVESTIGATION INTO THE FLUIDIZATION AND HEAT TRANSFER OF LOW DENSITY PARTICLES IN A FLUIDIZED BED WITH APPLICATIONS

by

JAMES MICHAEL MODLIN

Submitted to the Department of Mechanical Engineering
on May 10, 1985 in partial fulfillment of the
requirements for the Degrees of Mechanical Engineer and
Master of Science in Mechanical Engineering

ABSTRACT

The lack of reliable data on the fluidization and heat transfer characteristics of low density particles in a fluidized bed has prompted an experimental and analytical investigation into this subject. Seven groups of particles ranging in diameter from 0.25 mm to 2.0 mm and density from 2.5 to 32 pcf have been successfully fluidized and have been shown to be generally well predicted by classical fluidization and fluidized bed heat transfer theory. Two other groups of particles, also in this approximate range of particle diameter and density, are, however, unable to be fluidized due to significant inter-particle and static electric attractions.

Using the experimental data and results as a basis of analysis, two application of low density particle fluidization in a building efficient energy management program are discussed. A fluidized bed can be incorporated into the wall cavity of a building for use as either a collector of solar energy or as a heat exchange medium in a building space heating/cooling program. As a solar collector, it is shown that the low density particle fluidized bed would thermally perform between comparable conventional liquid and air-cooled flat plate solar collectors. It would require less water pumping power and plumbing than the liquid collector and less air pumping power than the air collector.

As a heat exchanger, the low density particle fluidized bed would function in a building space comfort control capacity by providing a large wall surface area available for heat transfer to or from the space. It is shown that this rate of heat transfer provided by the fluidized bed is significantly greater than what is available for air alone flowing over the surface and at reduced air pumping power requirements.

Thesis Supervisor: Dr. Leon R. Glicksman
Title: Senior Research Scientist

ACKNOWLDGEMENTS

It is with great appreciation and thanks that I acknowledge those fine people who have made this work possible. I am truly indebted to Dr. Leon R. Glicksman, my thesis advisor, who not only conceived this thesis investigation, but who also time and again provided invaluable guidance and assistance during all stages of its completion.

Special thanks are in order to the Department of the Army of the United States for their faith and confidence in my abilities and financial support of my graduate studies. Similarly, thanks are extended to my numerous officemates and colleagues for their continued advice and support. Deep appreciation also goes to Sandy Tepper whose patience and expertise turned my handwritten drafts into a typed professional document.

Above all, my sincerest thanks and love are extended to my wife Cindy and sons Jim and Matt for their unyielding support and reassurance during this period of our lives. To you this work is dedicated.

TABLE OF CONTENTS

LIST OF FIGURES

LIST OF TABLES

NOMENCLATURE

A_c	:	solar collector surface area
A_f	:	total fin surface area
A_i	:	total inside surface area of a heat transfer tube
A_u	:	total unfinned surface area
A_x	:	cross-sectional area
d_p	:	particle diameter
g_c	:	gravitational constant
h_f	:	fin heat transfer coefficient
h_i	:	working fluid heat transfer coefficient inside a tube
h_u	:	unfinned heat transfer coefficients
I_c	:	solar insolation on a collector surface
mf	:	denotes minimum fluidization conditions
$\frac{\Delta P}{L}$	:	fluidized bed pressure drop per unit height of bed
Pr	:	Prandtl number of the fluidizing gas
q	:	rate of heat transfer
q_{loss}	:	rate of heat loss from a solar collector plate to the environment
q_u	:	rate of heat transfer from the solar collector plate to the working fluid (useful energy)
ΔT	:	the temperature difference between a heated surface and the fluidized bed
T_B	:	fluidized bed bulk temperature
T_w	:	heated surface temperature
U	:	fluidizing gas velocity at distributor

α_s : solar absorbance of a collector plate surface

ε : fraction of voids in a bed of particles

ε_w : emmissivity of a heated surface

η_f : fin efficiency

k_a : thermal conductivity of air

k_s : thermal conductivity of a fluidized particle

μ : dynamic viscosity of the fluidizing gas

ν : kinematic viscosity of the fluidizing gas

ρ_g : density of the fluidizing gas

ρ_s : density of the fluidized particles

σ : Stephan-Boltzman constant

τ_s : effective solar transmittance of the solar collector cover(s)

ϕ_s : particle sphericity

CHAPTER 1

INTRODUCTION

Fluidized bed technology has been successfully applied to various industrial process problems such as catalytic cracking and the removal of sulfur based pollutants associated with coal combustion. These successes have continued to spur research efforts into many other areas. One area, though, that has not been explored until now is the application of air fluidized bed technology in building energy management.

A review of the literature indicates that previous investigations of fluidized bed technology have used as a fluidizing material particles ranging in size from approximately 50 μm to 1 mm and densities from 500 - 2500 kg/m^3. These materials, which generally include sand, metallic grit, glass beads and limestone, were selected on the basis of being best suited for the intended applications and studies. Thus, the theories, practices, successes and failures of past work in fluidized bed technology have all been based on the use of these dense type materials.

As a result, this extensive amount of work has developed well known relations and theories relating such concepts as minimum fluidization velocities, bed pressure drops, and bed heat transfer to particle dimater and density.

A goal of this work, on the other hand, is to assess the feasibility of using a fluidized bed as part of a building efficient energy management program. The concept of using a fluidized bed in this manner consists of it being integrated into a building wall cavity to serve as a collector of solar insulation or as a heat exchange medium.

In these applications a building's wall cavity would be filled with a fluidizing material. As a solar collector, the exterior side of a south facing wall would serve as a solar insulation collector plate. The heat would be transferred by the fluidized particles to immersed heat transfer tubes. A working fluid, such as water, passing through the tube would collect this energy and transport it to another location out of the wall for storage or immediate use (see Figure 7.1).

As a heat exchange medium the fluidized bed could be used in either a building space heating or cooling scheme. Due to the fluidized bed isothermal characteristic, a constant temperature wall, either above or below room temperature, could be maintained to provide the desired path of heat transfer.

For either application, this use of a fluidized bed must provide thermal performance and operational requirements that are comparable, or better, to conventional alternatives in order to be feasible. Two operational requirements, bed pressure drop and external power needs, mandate the use of low density fluidization materials in these applications. Fluidizing materials such as sand or a metallic grit yield large bed pressure drops, in excess of the structural capability of a typical building wall cavity. These materials also require significant air pumping power for fluidization. Low density materials (less than 500 Kg/m^3), on the other hand, would greatly reduce these effects and thus provide a potentially more reliable and less expensive alternative to conventional equipment.

However, a review of the literature also reveals that little data exists on the fluidization and heat transfer of low density materials in a

fluidized bed [1,3,4]. This evaluation must be conducted in order to first completely determine the feasibility of the use of fluidized beds of low density materials in a building energy management program and second to provide a further broadening of understanding in fluidized bed technology.

To this end, the primary objective of this work has been to identify and test various low density materials to determine their fluidization and heat transfer characteristics. Fluidization studies are made to determine minimim fluidization velocities, bed pressure drops, flow regimes, and the parameters that effect these. Heat transfer studies are conducted from a heated bed wall surface (to simulate a heated solar collector plate) and an immersed tube (to simulate heating the working fluid). Data analysis is based upon the theories and trends previously developed with denser materials to determine the degree of correlation or discrepancy between experimental results and theoretical predictions for the low density material.

Based upon the experimental results, comparisons are made between the expressed applications of the low density material fluidized bed and the conventional counterparts.

Initially, however, a review of the fundamental theories of fluidized bed technology must be conducted in order to provide the framework upon which this investigation is based.

CHAPTER 2

THEORETICAL BASIS OF INVESTIGATION

This chapter will outline the theory upon which the experimental design and analysis of this investigation is based. A review of the fundamentals of fluidization and fluidized bed heat transfer will be conducted as developed from previous work with dense particles. The brief examination of theory presented here will yield, in general terms, the tools and concepts required for the detailed investigation of low density particles. The specific development of these tools and concepts for this particular experiment will be conducted in Chapter 3.

2.1 The Mechanisms of Fluidization

Simply stated, fluidization is the operation by which an agglomeration of solid particles are transformed into a fluid-like state when brought into contact with a fluid. Although fluidization may be accomplished with either a liquid or gas, the concern of this investigation is fluidization with air at ambient conditions.

As the air flows upward through a bed of solid particles, at low flow rates, it percolates through the void spaces between the particles. This condition is known as a fixed bed. However, as the air flow rate increases the particles begin to move apart and may vibrate slightly [1]. With further increases of flow rate a point is eventually reached where the drag force exerted on the individual particles by the upward moving gas just equals the weight of the particles, the bed height has increased, and the particles have become suspended. This point is called minimum fluidization. The air velocity required to attain minimum fluidization is

called the minimum fluidization velocity, U_{mf} , and the pressure drop within the bed at this point equals approximatedly the cumulative weight of the suspended particles.

Ergun [2] has developed a relationship for the pressure drop of a gas through a fixed bed of uniformly sized solids as

$$\frac{\Delta P}{L} g_c = 150 \frac{(1-\varepsilon)^2}{\varepsilon^3} \frac{\mu U_0}{(\phi_s d_p)^2} + 1.75 \frac{(1-\varepsilon)}{\varepsilon^3} \frac{\rho_g U_0^2}{\phi_s d_p} \quad . \tag{2.1}$$

At minimum fluidization, where the pressure drop equals approximately the weight of the suspended particles the following relation holds

$$\frac{\Delta P}{L_{mf}} = (1 - \varepsilon_{mf})(\rho_s - \rho_g) \frac{g}{g_c} \tag{2.2}$$

By combining Eqs. (2.1) and (2.2) Kunii and Levenspiel [3] have developed an expression for analytically predicting the minimum fluidization velocity of a bed of uniformly sized particles

$$\frac{1.75}{\phi_s \varepsilon_{mf}^3} \left(\frac{d_p U_{mf} \rho_g}{\mu} \right)^2 + \frac{150(1 - \varepsilon_{mf})}{\phi_s^2 \varepsilon_{mf}^3} \left(\frac{d_p U_{mf} \rho_g}{\mu} \right) = \frac{d_p^3 \rho_g (\rho_s - \rho_g) g}{\mu^2} \tag{2.3}$$

At air velocities beyond the minimum fluidization velocity, $U_0 > U_{mf}$, instabilities begin occurring within the bed in the form of bubble creation at the air distributor and enlargement as they rise to the top of the bed. Davidson [4] has attempted to explain this phenomenon through the use of his "Two-Phase Theory of Fluidization". He states that when $U_0 > U_{mf}$ a fluidized bed can be visualized as having two simultaneous phases: an emulsion phase and a bubble phase. As air flow at U_0 enters the bed, the emulsion phase (the fluidized particles) constantly remains at ε_{mf} with a corresponding U_{mf} requirement. The excess volume flow of air, $(U_0 - U_{mf})$ x (bed cross-sectional area), passes through the bed as bubbles. The presence of bubbles determines the total bed expansion and provides for solid circulation within the bed. This bubbling condition is known as an aggregatively fluidized bed.

Despite this increase in air flow beyond minimum fluidization and the resultant bubble formation the bed pressure drop remains relatively unchanged from that at minimum fluidization. This is due to the fact that the dense gas-solid phase is well aerated and can deform easily without appreciable resistance. Thus, the minimum fluidization velocity can be experimentally determined by varying U_0, beyond minimum fluidization, measuring the corresponding bed pressure drop, and checking for its constancy as U_0 is decreased to the point of minimum fluidization. Kunii and Levenspiel recommend using this experimental method of determining U_{mf} for the particular size distribution of particles actually in a bed rather than Eq. (2.3).

Additionally, Geldart [5] has classified materials into four general groups according to their fluidization characteristics (Fig. 2.1):

A. particles of low density (less than 1400 kg/m^3) and of mean diameter between 20 and 100 μm;

B. powders having a mean diameter between 40 and 500 m and a density in the range 1400 to 4000 kg/m^3;

C. small particles having a mean size less than 30 μm for which the effect of interparticle forces is significant;

D. large (>600 μm) and/or dense particles.

Group A particles exhibit considerable bed expansion before the onset of bubbling within the bed and collapse slowly after the air supply is turned off. Materials in Group B exhibit much less stable bed expansion and free bubbling begins at or a little above minimum fluidization. Geldart states that a particle would generally belong to Group B if

$$(\rho_s - \rho_g)^{1.17} d_p \geq 906{,}000 \tag{2.4}$$

with the densities expressed in kg/m^3 and the particle diameter in μm. Group C materials exhibit a strong tendency to agglomerate and are usually difficult to fluidize. Particles in Group D generally fluidize unstably. In air at atmospheric pressure a particle would belong to Group D if

$$(\rho_s - \rho_g) d_p^2 > 10^9 \tag{2.5}$$

2.2 The Mechanisms of Heat Transfer in a Fluidized Bed

In an aggregatively fluidized bed, it is generally believed heat transfer is caused by the rapid mixing of the particles within the bed.

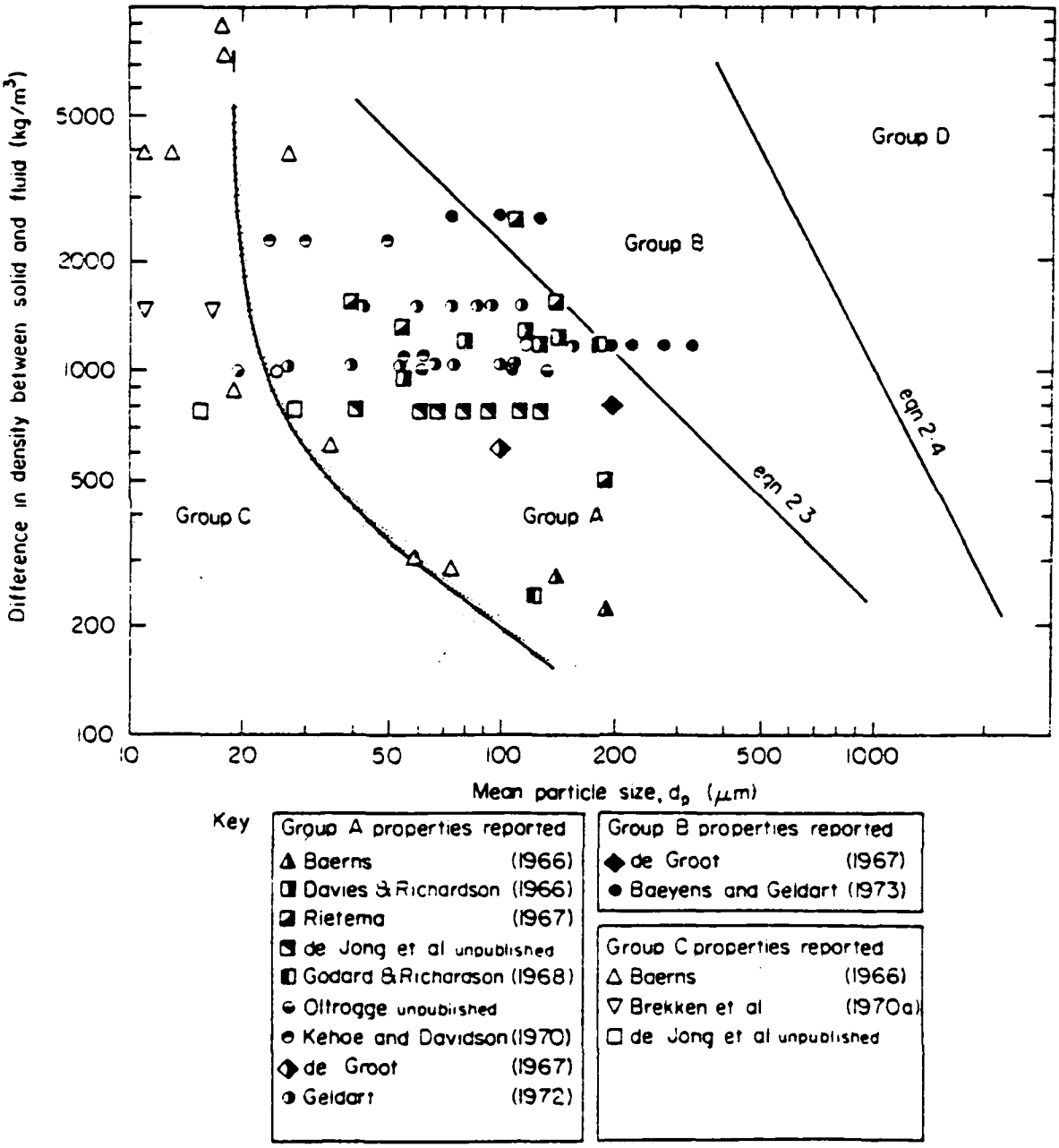

FIGURE 2.1 Geldart's Materials Classification [5]

Bubbles displace particles as they pass and entrain particles into their trailing wake. As a bubble sweeps near or over a surface, particles at the surface are displaced by fresh particles at the mean temperature of the bed. Heat transfer ensues as long as there is a temperature difference between the particles and the surface. It has been suggested that initially the heat transfer is confined to the surface and first layer of particles adjacent to it [6]. As time progresses, the temperature of the adjacent particles approaches that of the surface and heat transfer ensues between the first and second layer of particles. If the particles remain at the wall for a long period of time the heat transfer interaction includes particles far from the wall.

Mickley and Fairbanks [7] were the first to physically model a transient renewal model of heat transfer between an immersed surface and a fluidized bed. In this model the dense phase (the mixture of particles and gas) adjacent to the surface is considered a homogeneous material with an effective thermal conductivity and heat capacity. Mickley and Fairbanks postulated that heat transfer ensues as a packet of this material comes in contact with the immersed surface. A one-dimensional transient heat conduction takes place until the packet is replaced by another one due to bubble motion sweeping the surface or otherwise disrupting the material. The resulting heat transfer coefficient, h_e, predicted by this model averaged over the packet residence time at the surface is

$$h_e = \left(\frac{4\, k_e\, \rho_s (1 - \varepsilon_{mf})\, C_s}{\pi\, t_r} \right)^{1/2} \qquad (2.6)$$

where

k_e = effective packet thermal condutivity

$\rho_s(1-\varepsilon_{mf})C_s$ = effective packet heat capacity

t_r = packet residence time at the surface.

This model of heat transfer predicts that as the residence time continually decreases heat transfer will increase. However, several investigators have experimentally found that the heat transfer coefficient approaches an upper limit as residence times are decreased [8,9]. Baskakov [10] accounted for this result by introducing the concept of a thermal constant resistance in series between the surface and particles.

Additional work has further indicated that, especially for large particles (~1mm), heat transfer between particles and a surface is not only dependent upon the heat capacity of the particle and the direct thermal contact between particle and surface, but also on convective and radiative heat transfer through the gas layer surrounding the contact points [6]. Further it has been demonstrated that the average heat transfer coefficient for large particle beds shows a modest rise with increasing U/U_{mf} approaching a constant value. Small particle beds, on the other hand, have exhibited dramatic changes in heat transfer coefficient as U/U_{mf} increases [6].

In light of these results, Gelperin and Einstein [11] have postulated that the heat transfer averaged over an immersed surface, $\bar{h}$, is determined by the percent of the surface covered by particles, $(1-\delta)$, the average heat transfer coefficient at the surface covered by the emulsion, $h_{surface}$, and the average heat transfer coefficient during bubble or void contact at the surface, h_{void},

$$\bar{h} = (1 - \delta)h_{surface} + \delta h_{void} \tag{2.7}$$

In this model the average heat transfer between the particles and the surface, $h_{surface}$, is due to the previously discussed combined series effect of the surface resistance to heat transfer and the particle renewal model of Mickley

$$\bar{h}_{surface} = \left[\frac{1}{h_w} + \frac{1}{h_e} \right]^{-1} \tag{2.8}$$

where

h_w = the combined effect of conduction, convection and radiation heat transfer at the surface

h_e = the heat transfer coefficient defined by Eq. (2.6).

In non-dimensional terms h_w can be expressed as

$$Nu_w = Nu_{conduction} + Nu_{convection} + Nu_{radiation} \tag{2.9}$$

and using values determined by Glicksman, et al. [6]

$$Nu_w = 6 + 0.05\ Re\ Pr + Nu_{radiation} \tag{2.10a}$$

$$Nu_w = 12 + 0.05\ Re\ Pr + Nu_{radiation} \qquad (2.10b)$$

The value of 6 in Eq. (2.10a) is based on Decker's [1] results in a well fluidized bed. The value of 12 in Eq. (2.10b) is based upon Gloski's [12] results for near a bed wall at close to minimum fluidization conditions.

Although the bubbles in a fluidized bed help promote heat transfer by providing the mechanism for rapid particle replacement against an immersed surface, they also tend to reduce the overall heat transfer by covering a portion of the surface and thus reducing the surface area in contact with particles. This effect is represented by the term h_{void} in Eq. (2.7). The non-dimensional expression for h_{void} may be estimated using the Polhausen solution for heat transfer in a laminar boundary layer on a flate plate

$$Nu_{void} = 0.664\ Re^{0.5}\ Pr^{0.33}\ \left(\frac{d_p}{d_b}\right)^{0.5} \qquad (2.11)$$

where Re = the Reynolds Number expressed as [6]

$$= \left[\frac{(U_b + 3U_{mf})d_p}{\nu}\right]$$

Pr = the gas Prandtl Number

d_b = the average bubble diameter passing over the surface.

The model represented by Eq. (2.7) has been used by several investigators [1,6,12] to predict heat transfer coefficients with good results and will be used in this investigation.

Another area of potentially affecting fluidized bed heat transfer is through the use of finned surfaces. The presence of fins increases the available surface area for heat transfer. This may be especially useful for water cooled immersed tubes when the major resistance to heat transfer occurs on the outside of the tube.

However, there presently appears to be a general lack of extensive data available for finned surface use in a fluidized bed. This lack of data precludes the use of any available model or correlation to predict finned surface heat transfer coefficients with confidence. Glicksman has suggested [6] using data for bare tubes to predict $\bar{h}$ of Eq. (2.7) and then reducing this value by 30-50% to estimate the finned tube heat transfer coefficient. Further, it has been shown by various investigators [13,14,15,16] that in spite of this reduction in heat transfer coeficient and the inclusion of fin efficiency, finned surfaces still can provide increased overall heat transfer. It has also been found, though, that as the fin spacing is reduced to less than ten particle diameters the heat transfer coefficient decreases due to the probable decreased particle mobility between the fins [6].

CHAPTER 3

CONCEPT OF THE INVESTIGATION

Chapter 2 outlined the general theory and relationships that have been developed to study particle fluidization and fluidized bed heat transfer in air. This chapter will, initially, define the specific areas of interest of this investigation. A further development of the concepts presented in Chapter 2 will then follow in order that they may be directly applicable to the requirements of this work.

3.1 Areas of Investigation

Chapter 1 discussed the need for analyzing the fluidization and heat transfer characteristics of low density particles in a fluidized bed. In this investigation several particles with densities of approximately 2 - 30 pcf and diameters of 0.25 - 2 mm will be analyzed by attempting to apply the theory discussed in Chapter 2. Experiments will be conducted in which fluidization and heat transfer data will be collected and analyzed.

Fluidization data of interest in this investigation is the minimum fluidization velocity of the test particles, the pressure drops associated with the low density aggregatively fluidized beds, and the Geldart classification of the test particles based upon their ability to be fluidized. Heat transfer data, in the form of average heat transfer coefficients, will be collected for two geometries: wall-to-bed and immersed tube-to-bed. Relationships between heat transfer coefficients and air velocity, particle density, and particle diameter will be investigated. Comparisons between unobstructed and obstructed air flow on wall heat

transfer and between finned and unfinned immersed tube-to-bed heat transfer are also of interest.

Although the present theory available for this investigation has been developed using significantly denser material it will, nevertheless, be utilized as a basis for comparing results of low density material testing. As such, the fluidization theory outlined in Chapter 2 can be compared directly. The heat transfer theory will require further detailing to be satisfactorily used for this analysis. Section 3.2 presents this detail.

3.2 Model for Heat Transfer Analysis

The model for heat transfer analysis that is used in this investigation is the one expressed by Eq. (2.7). Inherent in this model are several factors that must be evaluated or reasonably assumed based upon the model's particular application.

The first factor entails the determination of the fraction of a surface covered by voids, δ . There is no specifically accurate way of determining δ . However, several methods and relationships exist for estimating it closely. This analysis will be based on Geperin's [11] relationship of

$$\delta = 1 - \left(\frac{1 - \varepsilon}{1 - \varepsilon_{mf}} \right) \tag{3.1}$$

with ε and ε_{mf} having assumed values of 0.6 and 0.5, respectively, for all test particles. These values are based upon representative data from other investigations of comparable particle diameter but greater density fluidization [17]. Substituting these values for ε and ε_{mf} into Eq. (3.1) yields

$$\delta = 0.20 \tag{3.2}$$

The term representing the average heat transfer between the particles and the surface, $h_{surface}$, is defined by Eq. (2.8). Contained within this expression are several parameters represented by Eqs. (2.6) and (2.10). The heat transfer coefficient of the emulsion, h_e, theorized by Mickley is based upon effective thermal properties and particle-to-surface residence times. These parameters are inherently difficult to quantify and are themselves subject of extensive research [17]. In this investigation Gelperin's relation for effective conductivity, k_e, will be used [11]:

$$\frac{K_e}{K_a} = 1 + \frac{(1-\varepsilon)\ (1 - K_a/K_s)}{\frac{K_a}{K_s} + 0.28\ \varepsilon^{0.63(K_s/K_a)^{0.18}}} \tag{3.3}$$

Particle-to-surface residence times will be estimated based upon visual observation and previous experimental representative values [17]. This inherent uncertainty of residence time is a possible critical area of analysis and will be further discussed in Chapter 6.

The heat transfer coefficient represented by h_w can be derived from Eq. (2.10)

$$h_w = [6 + 0.05\ RePr + Nu_{rad}]\ \frac{K_a}{dp} \tag{3.4a}$$

or

$$h_w = [12 + 0.05\ RePr + Nu_{rad}]\ \frac{K_a}{dp} \tag{3.4b}$$

where Re = Reynolds Number defined as [6]

$$Re = \frac{U_{mf}\ (1 + 2\delta)dp}{\nu}$$

The radiation component Nusselt Number, Nu_{rad}, may be expressed by [6]

$$Nu_{rad} = \frac{\sigma(T_w^4 - T_B^4)dp}{(\frac{1}{\varepsilon_B} + \frac{1}{\varepsilon_w} - 1)(T_w - T_B)K_a} \tag{3.5}$$

where

ε_B = emissivity of the fluidized bed

$$= \frac{\varepsilon_{particle} + 1}{2}$$

Combining Eqs. (3.4a) and (3.4b) with Eq. (3.5) and substituting the appropriate air property values the following relations for h_w result

$$h_w = \frac{0.093}{dp} + 3.25\ U_{mf}(1+2\delta) + h_{rad} \tag{3.6a}$$

or

$$h_w = \frac{0.186}{dp} + 3.25\ U_{mf}(1+2\delta) + h_{rad} \tag{3.6b}$$

where

$$h_{rad} = \frac{\sigma(T_w^4 - T_B^4)}{(\frac{1}{\varepsilon_B} + \frac{1}{\varepsilon_w} - 1)(T_w - T_B)}$$

Both expressions for h_w will be used in this investigation for analysis of the low density particle heat transfer due to the unknown nature of their results.

The term representing the heat transfer due to the passage of bubbles or voids over a surface, h_{void}, is defined in nondimsional terms by Eq. (2.11). Further quantification of this expression can be accomplished through substitution of known and approximated parameters. The average bubble rise velocity, U_b, is closely approximated by [6]

$$U_b = 0.71\sqrt{g\ d_b} + (U_0 - U_{mf}) \tag{3.7}$$

For the purpose of this analysis and to be conservative the average bubble length, d_b, will be taken as: one-half the plate width for the wall heater, one-quarter of the tube circumference for the unfinned tube heater, and equal to the average fin spacing for the finned tube heater. Using these approximations and the appropriate air properties h_{void} may be expressed as

$$h_{void} = 0.707\left[\frac{U_0 + 2U_{mf} + 0.71\sqrt{g\ d_b}}{d_b}\right]^{\frac{1}{2}} \tag{3.8}$$

Finally, for finned surface analysis two approaches will be investigated. The first approach will be to simply apply the previously described heat transfer model modified by an overall corresponding surface efficiency. For a finned surface the total rate of heat transfer, q, is

given by

$$q = (\eta_f A_f h_f + A_u h_u)\Delta T \tag{3.9}$$

Taking $h_u = h_f = h$, an overall surface efficiency, ε , may be defined as

$$\varepsilon \equiv \frac{q}{Ah\Delta T} = \eta_f \frac{A_f}{A} + \frac{A_u}{A} \tag{3.10}$$

where $A = A_u + A_f$ [18].

The second approach will be to numerically compare the finned tube heat transfer coefficients to the unfinned values to determine the magnitude of change, if any, between the two geometries.

CHAPTER 4

EXPERIMENTAL APPARATUS DESIGN

Although the proposed fluidization and heat transfer experiments are straightforward in theory, the design and construction of the various components of the experimental apparatus requires care. This chapter will discuss these aspects of the experimental apparatus employed to carry out the necessary data collection. This discussion will include the fluidized beds, heaters, and particles used in these experiments. The details of the data acquisition, however, will be discussed in Chapter 5.

4.1 Fluidized Beds

Two different fluidized beds have been used for data collection. A two-dimensional bed is used primarily to study the fluidization behavior of the test particles and the wall heat transfer characteristics. This type of bed allows experiments to be carried out in a fluidized bed of similar geometry to that of a typical building wall cavity. It consits of a 1 in x 16 in rectangular cross-section and an overall height of 24 inches available for particle fluidization. The air distributor is a plastic perforated sheet covered underneath by three inches of foam rubber. The foam rubber serves to increase the pressure drop across the distributor and thus insure a more uniform air flow. Figure 4.1 details the overall dimensions of the two-dimensional bed.

A three-dimensional bed is used to study the immersed tube heat transfer characteristics. Although this type of bed does not realistically model the rectangular cross section of a typical wall cavity, this particular bed allows for good particle to tube interaction that is not

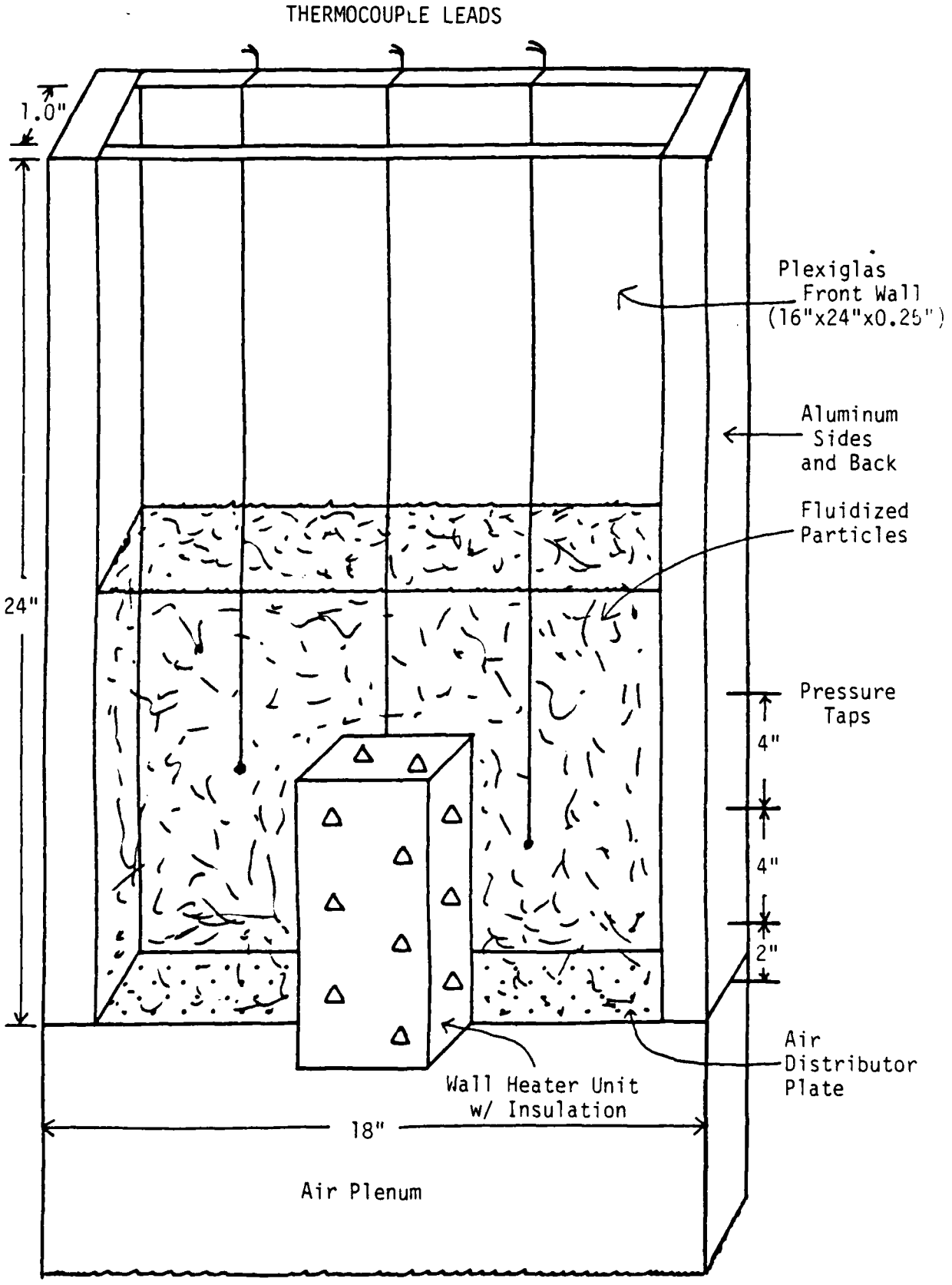

FIGURE 4.1 Two-Dimensional Fluidized Bed

possible in the available two-dimensional bed. The depth of the three-dimensional bed and the radial dimension of the immersed tube heaters approximates that of the depth of a wall cavity, 3-4 inches, and a standard immersed heat transfer tube, 1/2 to 3/4 inch in diameter, within it. In this arrangement there is approximately a 2-1/2 inch clearance between the unfinned tube heater and the bed walls (front and back) and a 1-7/8 inch clearance between the finned tube heater and the walls. This bed consists of a 6 in. x 6 in. square cross-section and an overall height of 36 inches available for particle fluidization. The air distributor consists of a porous plate covered by approximately 16 inches of sand to increase the pressure drop across the distributor plate and insure uniform air flow through the bed. Figure 4.2 details the overall dimensions of the three-dimensional bed.

The flow of air through both beds is metered by a standard ASME square-edged orifice with flange taps [19]. Each bed has a tap near the bottom for particle removal and a plexiglas front wall for ease of particle observation. Additionally, both beds have pressure taps located on the walls available for measuring pressure drops within the bed.

4.2 Flat Plate (Wall) Heater Design

The measurement of average heat transfer coefficients from a wall surface to the fluidized matrial is accomplished by the use of a flat plate wall heater. To insure proper bed material fluidization and heat transfer at the bed walls it is necessary for the wall heater to be designed such that the heat flux generated by the heater is transferred directly into the two-dimensional bed and not lost to other areas, the heater surface remains at a uniform temperature, and the heater is mounted flush with the existing bed wall thus maintaining a smooth profile.

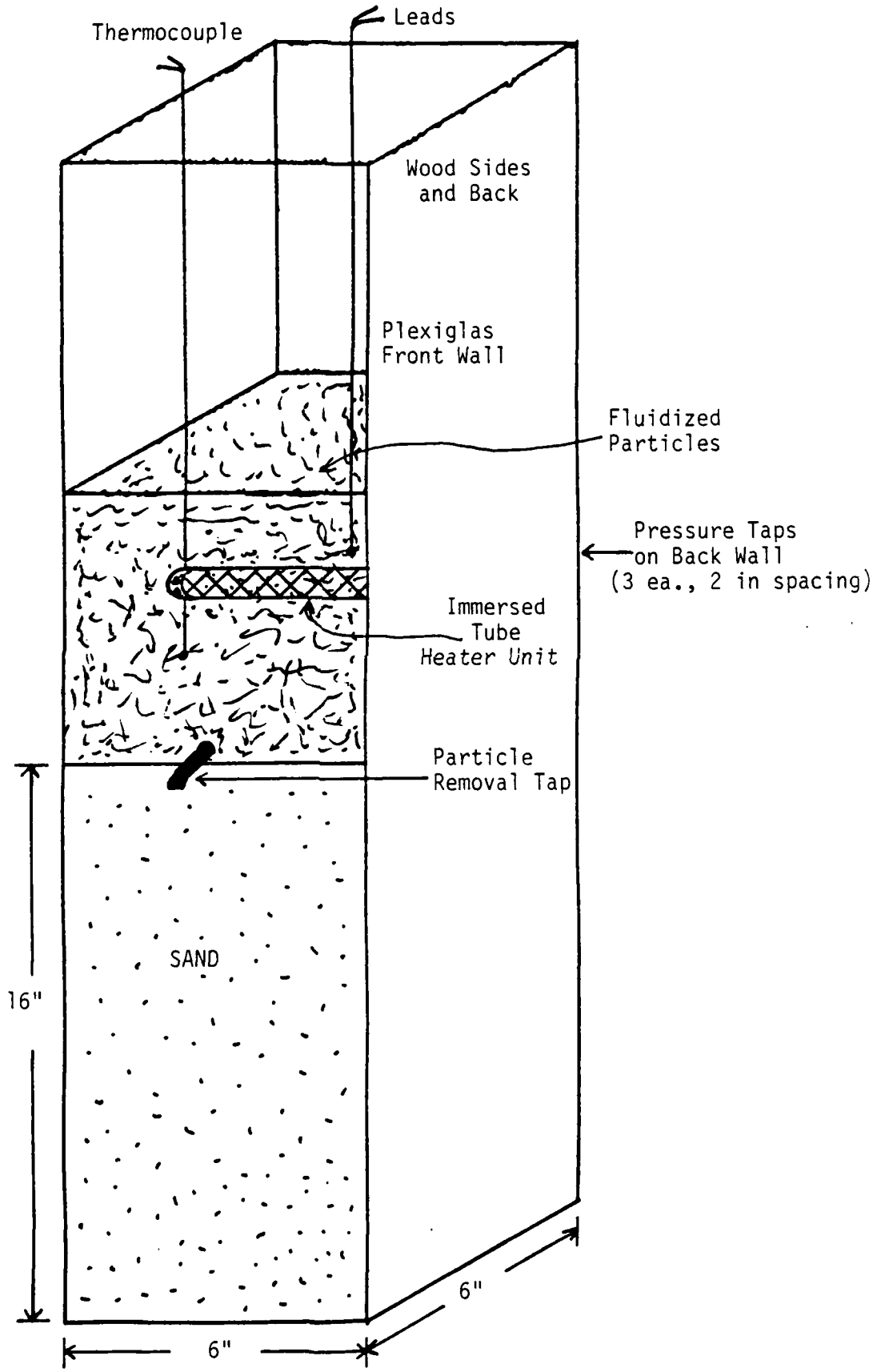

FIGURE 4.2 Three-Dimensional Fluidized Bed

Since the objective of the experiments using the wall heater is to measure the heat transfer coefficient from a heated wall surface to a fluidized bed of low density particles, it is vital that the experimenter know what heat flux is going into the bed. Thus, heat losses from other areas of the heater not in contact with the fluidized particles are to be kept to a minimum. Further, a uniform wall temperature must also be maintained on the heater surface in order to accurately calculate the heat transfer coefficient, and the heater element must be positioned in the bed's existing wall in order to both properly transfer the desired heat flux and not affect the normal fluidizing characteristics of the test material. Unwanted protrusions from the wall into the bed caused by the heater may decrease the bed materials mixing and consequently lower the heat transfer coefficient.

A flat, well insulated heater made of high thermal conductivity material is used in this experiment. As seen in Figure 4.1, the front plexiglas wall of the two-dimensional bed measures 16 in x 24 in. Due to the size of this frontal area a design choice has been made to confine the heater size to 1.5 in x 6 in. This size provides an adequate heat transfer surface (0.063 ft^2) while still allowing visual observation of the material being fluidized within the bed. The heater is oriented in the plexiglas wall with the long dimension being vertical. This allows for the longest heating length to be in the same direction as the bed's air flow and bubble direction of travel.

Secondly, a 0.25 in. thick copper plate was chosen as the heated surface due to copper's high thermal conductivity and to insure good temperature uniformity on the heater surface in contact with the bed material. Styrofoam is used as the primary heater insulation due to its

good insulating properties and availability. A standard 150 watt, 120 volt strip heater is used as the heat source to be attached to the copper plates by two 0.25 in x 1 in threaded brass rods. Holes are drilled in the copper plate approximately 0.0313 in. in from the particle contacting surface for copper/constantan thermocouple placement.

Dimensions for the insulation required to insure small heat losses, on the order of 1% of the total heat flux, were determined through a heat balance around the heater. For these calibrations an assumed value of the heat transfer coefficient from the heated surface to the bed of 20 Btu/hr-ft^2-°F and the ratio of the difference between the wall and fluidized bed temperatures to the difference between the wall and ambient air temperatures of 0.20 is used. As will be seen in Chapter 5 these assumptions are slightly over optimistic but do not compromise the results of the design. Appendix A outlines the procedure used in determining the insulation dimensions via the heat balance analysis and Figure 4.3 depicts the final design of the wall heater.

4.3 Unfinned Immersed Tube Heater Design

The experimental requirements for this heater are similar to those of the wall heater. However its design and construction are somewhat easier due to the drastic reduction of insulation required. The purpose of this heater is to provide a known heat flux into the three-dimensional fluidized bed and maintain a uniform tube wall temperature while being immersed within the bed.

For this design caution should be exercised in order to insure good thermal contact between the heating element and the tube material. Although, with proper insulation heat losses will be minimal, poor thermal contact between the heating element and tube and/or thin tube wall

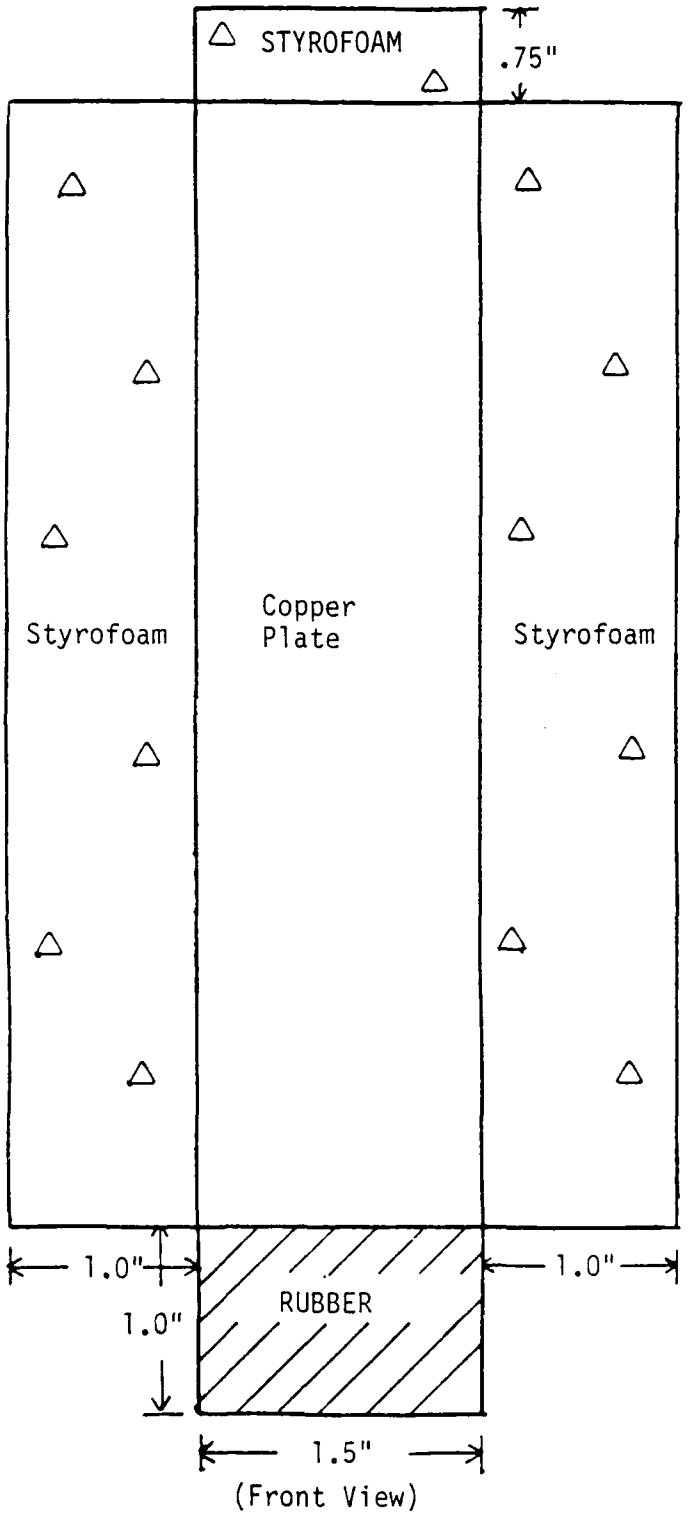

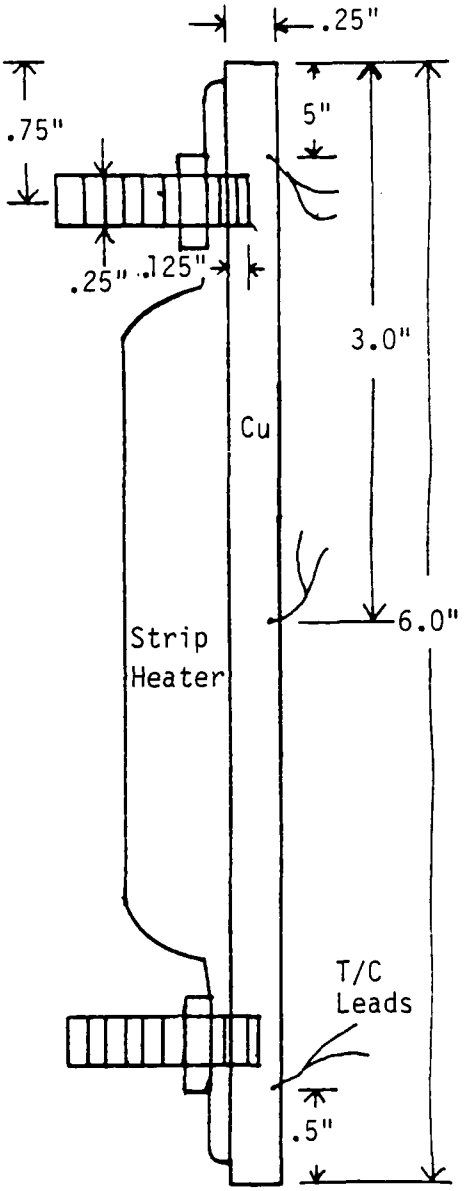

Thermocouple (T/C) Holes:
Dia. = 0.07"
Distance from outer wall = 0.031"
Styrofoam Back Insulation = 6.0"

FIGURE 4.3 Wall Heater Design

thickness could lead to nonuniform tube surface temperatures. This, in turn, will make accurate calculation of heat transfer coefficients difficult. For this reason standard wall tubing is not used in this experiment. Rather, a 1 in (diameter) x 5 in aluminum bar has been fabricated into the required tube heater.

A hole of 0.375 in is drilled and reamed through the center of the aluminum bar. Two additional holes on opposite ends of the bar are drilled approximately 0.0313 in in from the particle contacting surface for copper/constantan thermocouple placement. A 0.375 in x 5 in, 280 watt, 120 volt standard cartridge heater is inserted into the center hole of the aluminum bar. Styrofoam insulation is placed on the ends of the bar to prevent heat loss and provide structural stability for placement in the bed.

This design utilizes a high thermally conductive material and provides for over 0.25 inches of tube wall thickness to insure uniform tube surface temperature. Its overall length allows it to be centered and rigidly placed in the three-dimensional bed thus preventing any possible adverse effects to the bed material fluidization and heat transfer due to heater motion during fluidization. Figure 4.4 depicts the design of the unfinned immersed tube heater.

4.4 Finned Immersed Tube Heater Design

This heater only differs from the unfinned tube heater in concept by the presence of fins. Once again, however, standard finned tubing presents the same thin tube wall and heating-element-to-tube-thermal contact problems that are discussed with the unfinned tube design. Additionally, in many cases standard finned tubing has questionable to poor thermal contact between the fin base and the tube. It may be that in actual

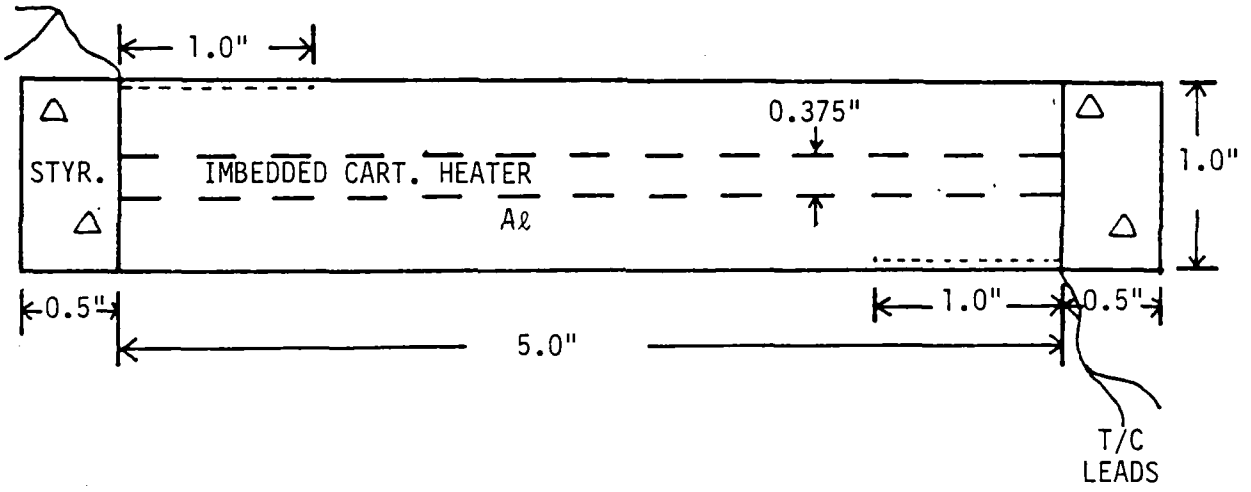

FIGURE 4.4 Unfinned Tube Heater Design

application standard finned tubing will be used (see Chapter 7), but the purpose of this heater is to accurately assist in the determination of a heat transfer coefficient. It is therefore necessary to reduce all possible sources of error and misrepresentation by insuring good thermal contacts.

For these reasons, the choice has been made to fabricate a finned tube heater. The design of this unit consists of a 0.75 in x 4.5 in copper bar with 13 copper circumferential fins of rectangular cross-section attached. A 0.25 in hole is drilled and reamed through the center of the bar. Thermocouple holes are placed similarly to those on the unfinned tube. A 0.25 in x 4.5 in, 110 watt, 120 volt standard cartridge heater is inserted into the center hole of the copper bar. Styrofoam insulation is placed on the ends of the bar to prevent heat loss and provide stability in the bed.

As with the unfinned tube, a high thermally conductive material with approximately 0.25 in tube wall thickness is used. A copper tube with copper fins is used rather than aluminum, as with the unfinned tube, because of the need to provide for good fin to tube thermal contact. Copper on copper can be easily and thermally effectively soldered together, whereas aluminum cannot.

The copper fins are 2.25 inches in diameter, square edged, and 0.02 inches thick. They are spaced approximately 3 fins per inch on the tube and have an efficiency of 90%. The fins are soldered to the copper tube with standrd 50/50 (Pb-Sn) solder. Care must be taken to achieve good thermal contact around the fin base with the tube. Appendix B details the specific analysis of these fins. Figure 4.5 illustrates the finned immersed tube design.

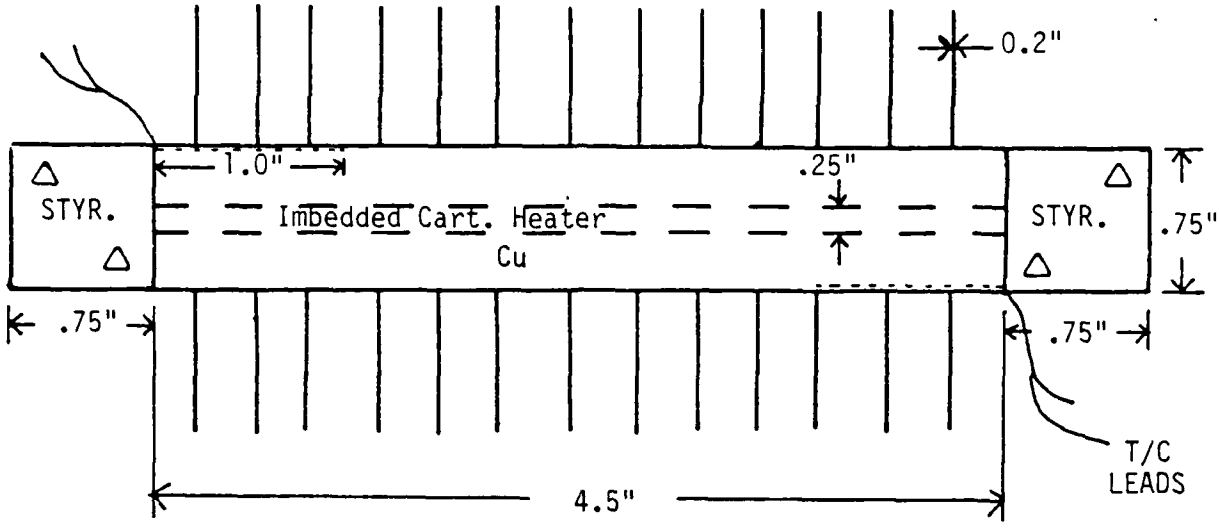

FIN DETAIL:

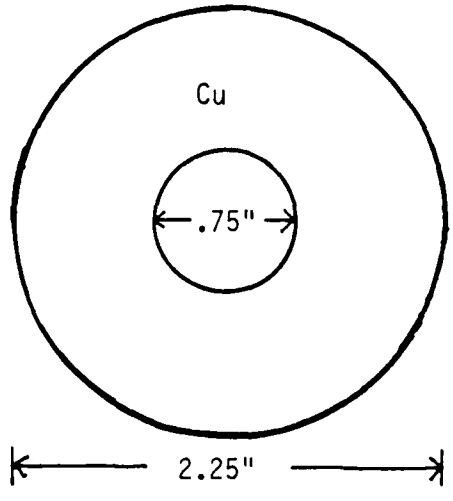

FIGURE 4.5 Finned Tube Heater Design

4.5 Particle Description

The primary distinction and sole purpose of this investigation is to analyze the fluidization and heat transfer of low density particles in a fluidized bed. As was discussed in Chapter 2, previous work has been extensively done on high density material in a fluidized bed and the results of their fluidization and heat transfer have been well documented [12,20,21].

Several different particles have been tested in this experiment with various results. These results are discussed in Chapter 5 and 6. Seven specific particles are thoroughly investigated. They range in average particle diameter of 250 μm to 2 mm and density from approximately 2.5 pcf to 32 pcf.

Test particles used have come from three primary sources: the 3M Company [22], the Norton Company [23], and the Whittermore Perlite Company [24]. The 3M "Macrospheres" are hollow cells with a shell made of a hollow glass bubble/resin combination. Their present applications include fiberglas reinforced plastics construction, filters, flotation devices, marine fabrication, vapor suppression, and electrolytic spacers. In this application the 3M "Macrospheres" M40X, particle diameter of 1 mm, density of 27.2 pcf and the M27X, particle diameter of 2 mm, density of 15.31 pcf are used.

Three particles are used from the Norton Company. These particles are Norton 650, diameter of 650 μm, density of 31.78 pcf, Norton 1, diameter of 1mm, density of 23.2 pcf, and Norton 1.5, diameter of 1.5mm, density of 20.85 pcf. These cellular glass nodules are composed of hundreds of individual hermetically sealed closed cells. Their present applications include use as a lightweight insulating filler in composites and for inducing controlled pores in ceramic bodies.

The third group of test particles are two sizes of Perlite. Perlite is a generic term for a naturally occurring siliceous volcanic rock. When heated to a suitable point in its softening range, it expands four to twenty times its original volume. This expansion is due to the presence of two to six percent combined water in the crude perlite rock. Upon heating, the water vaporizes creating microscopic hollow glassy bubbles. The formation of these bubbles in the perlite causes the expansion and accounts for perlite's characteristic low density. The expansion process can be controlled allowing for the manufacturing of perlite ranging in bulk density from 2-25 pcf and particle diameter of 250 μm to 4mm. Its present applications are strongly in use in the building industry as a thermal insulator, acoustical plastic ingredient, and a concrete aggregate and in the agricultural industry as a soil conditioner and fertilizer extender. In the present application of perlite in this investigation the average particle diameter is 250 μm, with a density of 4.5 pcf, and a diameter of 500 m, and a density of 2.7 pcf.

For all particles in this investigation, the stated particle diameter represents the average diameter determined from a standard seive analysis and may vary by $\pm$ 20%. Densities are expressed as bulk particle density. They have been determined by first measuring the loose-fill density of the particles and then dividing this value by the percent volume occupied by the solid particles. For this calculation all the particles were assumed to be spherical in shape and a loose fill voidage of 0.47 was used. Thus bulk density was thus determined by

$$\text{Bulk Density} = \frac{\text{Loose-fill Density}}{(1 - 0.47)} \qquad (4.1)$$

CHAPTER 5

DATA ACQUISITION AND REDUCTION

In the last chapter the design and construction of the required experimental aparatus and a description of the low density particles used was conducted. This chapter will detail the procedures used in acquiring the fluidization and heat transfer data of the seven test materials, the reduction of this data to usable form for later analysis, the checks made to determine heater performance, and an estimate of the error associated with the acquired data.

5.1 Particle Fluidization Determination

Since no previous work has been conducted on the actual fluidization of low density material, this determination has to be made before heat transfer experiments can be performed. As described in Chapter 4, seven particles have been completely analyzed for this purpose. However, there have been, at least initially, more than these seven particles investigated. In this section the inappropriateness of these other particles and the determination of the fluidization characteristics of the seven test particles is discussed.

To qualify as a test particle, the particle must exhibit good fluidization characteristics. It must be capable of being fluidized as evidenced by the presence of good bubble motion, good particle mixing, and modest air pumping power requirements for fluidization. The seven previously described materials satisfy these requirements, but not all particles investigated did.

Three such additional categories of particles have been identified. The first category is of the group that is characterized by a large average

particle diameter and small density. A material illustrating this is 0.125 in (3 mm) styrofoam beads having a density of approximately 2.35 pcf. When placed in the two-dimensional bed it is visually observed that fluidization is very poor. The beads appear to exhibit an electrostatic attraction to the walls of the bed. There appears to be no noticeable attraction between the beads themselves and some fluidization takes place in the interior of the bed away from the walls. Due to the insulating nature of styrofoam and the static electric attraction to walls, this material is not appropriate for the intended experiment. This is not to say, however, that these particles, nor styrofoam in general, should be totally ignored. As discussed in Appendix C static charging is a function of certain material properties and both styrofoam and plexiglas exhibit a strong electrostatic charging potential. Procedures can be taken to help reduce the effect of this phenomenon, a few of which are discussed in Chapter 8. These procedures are not employed in this experiment.

Another category investigated is that of large diameter and moderate density particles. As described in Chapter 2, a material's minimum fluidization velocity is, among other things, a function of particle diameter and density. As illustrated by the results, shown in Chapter 6, for the moderate to low density material the minimum fluidization velocity tends to be a much stronger function of particle diameter than density at moderate densities. Consequently, larger particles will generally require more air velocity to reach fluidization. This greater amount of air velocity directly relates to an increased external air pumping power requirement based on particle diameter alone. An attempt was made to fluidize Macrosphere and Norton particles of diameter 2.8 and 3 mm and density from 14-18 pcf in the available beds. The air velocity and

consequently the air pumping power required for fluidization of this material is far beyond what is desireable for the intended applications of this work. On the barely acceptable end is the 2 mm macrosphere M27X. Its data will help illustrate the problem with increasing particle diameter.

The third category of particles initially considered were particles with very small diameters and low density. Particles ranging in size from 20 - 200 μm (mean size of 70 μm) and density of 11 pcf have been tested. This silicate-based hollow microsphere material exhibits very poor fluidization and generally resembles the description of Geldart's Group C materials, but are best described in his Group A [5]. This result is further discussed in Chapter 6.

Thus, for the reasons discussed, these three materials are not completely investigated in this work. Their value, however, is in illustrating classes of low density materials that, for one reason or another, are not suitable for the intended applications of this work. That is to say, they fail to adequately demonstrate the criteria established in Chapter 1 of exhibiting good fluidization characteristics, having a low bed pressure drop, and requiring modest external air pumping power. On the other hand, the seven previously described test particles, based on initial screening, appeared to meet the established criteria and thus qualified for further investigation. A description of their investigation is now presented.

To determine the fluidization characteristics of the test particles the following procedures have been used. All air velocities are determined from the use of an ASME square edged orifice with flange taps. Two orifice plates have been used throughout the experiment to allow for ease of measurement and are described in Appendix D. In the two-dimensional bed

the particles under 1 mm in diameter have used orifice plate A and the larger particles have used plate B. In the three-dimensional bed plate B is used for all particles. Due to the particular geometry of the fluidized beds and the varying particle sizes used in this investigation this use of the two different orifice plates resulted in more accurate measurements of the orifice plate pressure drops.

All pressure drops, furthermore, are measured in one of two ways. The pressure drop across an orifice plate is measured by a water filled U-tube manometer graduated in tenths of an inch. Pressure drops in the fluidized beds are measured by an inclined manometer calibrated to read hundredths of an inch of water. Static air pressure upstream of the orifice is read by a standard pressure gage in psi.

Particle minimum fluidization was determined experimentally using the procedure outlined in Chapter 2. Well beyond minimum fluidization the pressure drop associated with the fluidized particles in the bed remains relatively constant and independent of the air velocity passing through the bed. As the air velocity decreases, approaching minimum fluidization velocity the bed pressure drop remains relatively constant. Below minimum fluidization, however, the bed pressure drop decreases linearly with air velocity. The corresponding air velocity associated with the intersection of the constant pressure drop line and the linearly decreasing line is the minimum fluidization velocity. This procedure is used to determine the particle minimum fluidization velocities and bed pressure drops of the test particles. Figure 5.1 illustrates this procedure. Appendix E displays the results graphically of these determinations for the test particles.

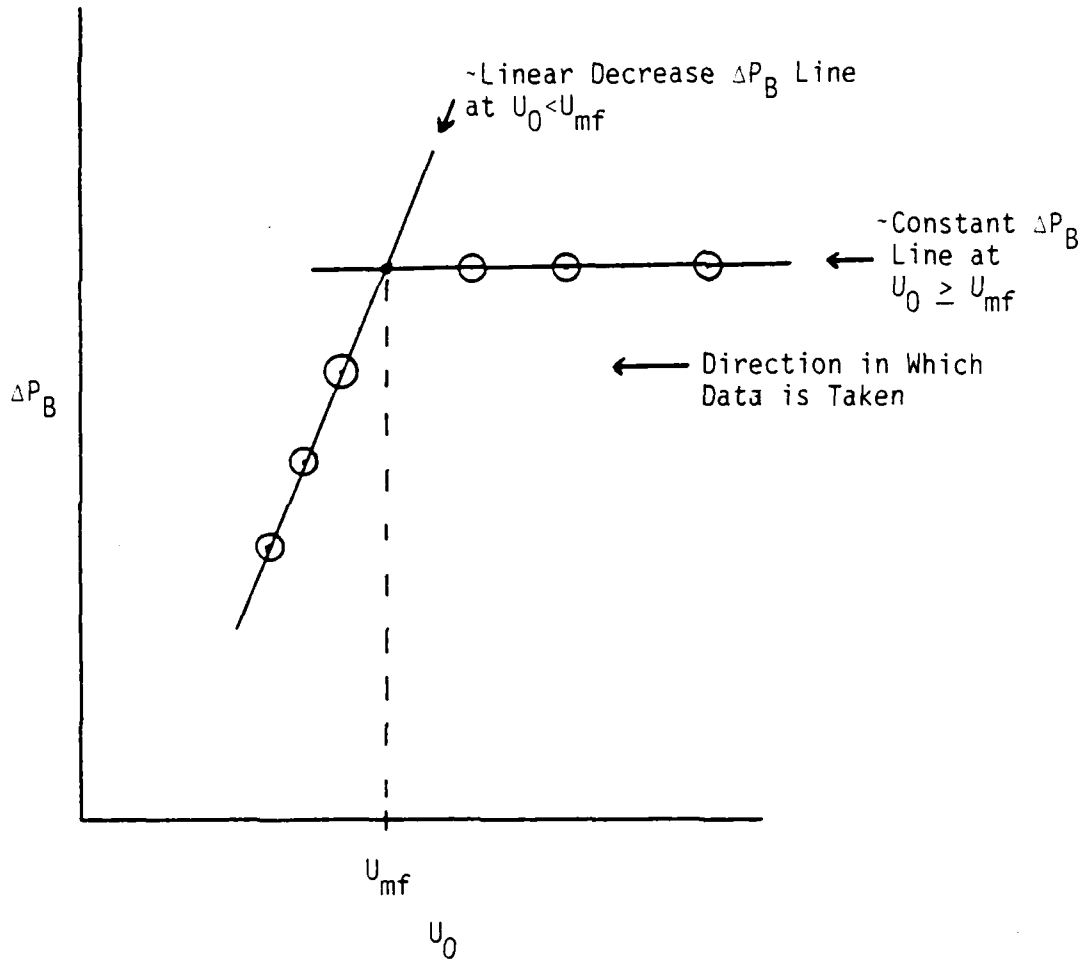

FIGURE 5.1 Particle U_{mf} Determination Procedure

5.2 Determination of Heat Transfer Coefficients

To determine all heat transfer coefficients, h , in this experiment, data has been taken to evaluate or measure the appropriate terms contained in the definition of the heat transfer coefficient:

$$q = h A \Delta T \tag{5-1}$$

Measurement of all heat fluxes into the fluidized beds is accomplished by incorporating the heaters in a simple electric circuit. The voltage and current supplied by a power source to a heater is measured. In this experiment a variable A-C (VARIAC) power supply is utilized to power the heater. Voltage and current is measured independently by two multimeters. Using the relation

Power = Voltage x Current

or

$$q = EI \tag{5-2}$$

the heat flux may be accurately measured Figure 5.2 details the heater electric circuit.

The value of each particular heater heat transfer area is simply the total surface area of the heater in contact with the fluidized particles. As indicated in Figures 4.3 through 4.5 these constant values are 0.063 ft^2 for the wall heater, 0.109 ft^2 for the unfinned tube heater, and 0.644 ft^2 for the finned tube heater.

Temperature measurements have been taken using standard copper/constantan thermocouples and read by a digital copper/constantan thermocouple thermometer to a 1°F accuracy. Thermocouples have been placed in various locations on the heaters and in the fluidized beds to insure accurate temperature measurement and uniformity on the heater surfaces and in the beds (see Figures 4.1-4.5).

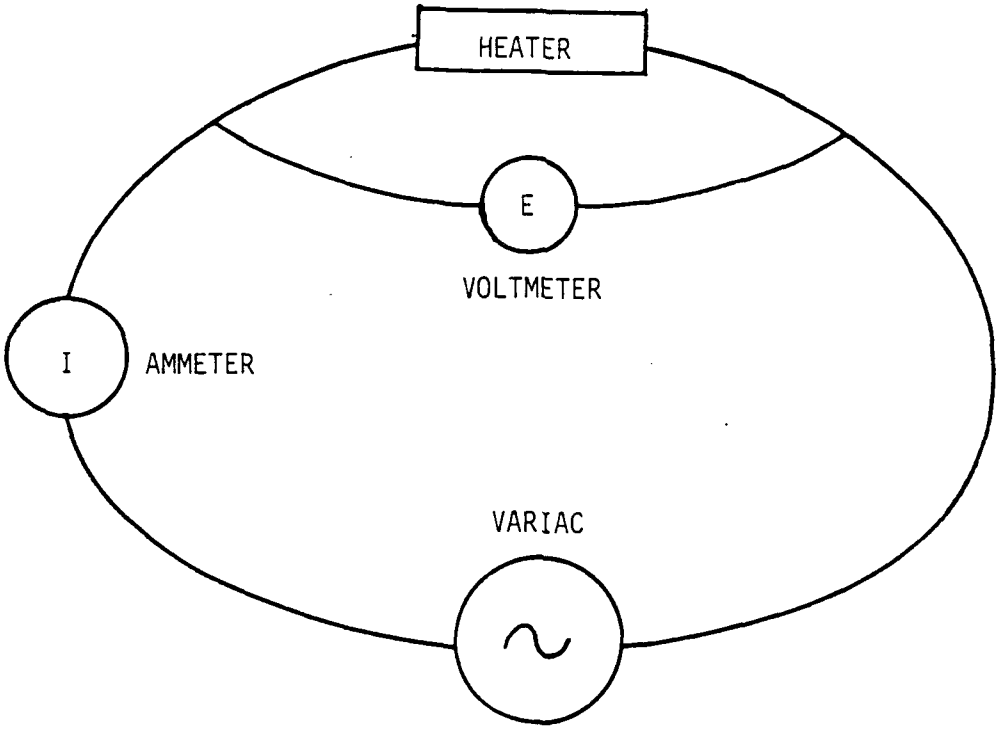

FIGURE 5.2 Heater Electric Circuit

For all experimentation, wall, unfinned and finned tube heating, a minimum of three tests per particle batch has been made. Heat flux for each test is kept approximately constant and the ratio of air velocity to minimum fluidization velocity, U/U_{mf}, is varied test to test. Each test is allowed to reach a steady-state condition, that is, the temperature of the heater surface and bed, is uniform and constant with time for a given heat flux and U/U_{mf} before data is taken and the appropriate heat transfer coefficient is evaluated. To reach this steady condition takes, on the average, two hours. Once a steady-state condition has been reached, the appropriate data is taken and the heat transfer coefficient is determined using Eq. (5.1).

5.3 Heater Performance Checks

In Chapter 4 and Appendix A details of the heaters used in this investigation and the analysis used to minimize heat losses have been discussed. It is further necessary to check the heater's actual performance in order to gain an estimate of any error present in determining heat flux or any required calibration to be done. This section will discuss the test performed on the wall heater and tube heater to check their operation.

The performance of the flat plate wall heater was checked using two methods. The first was by conducting a natural convection test of the heater. The heater unit (the heater and associated insulation) was oriented as depicted in Figure 4.1. A heat flux, q, was generated using the experimental equipment earlier described in this chapter. The steady-state heater wall temperature and the ambient air temperature were measured. From this data an experimental heat transfer coefficient, h_{exp} of 1.20 Btu/hr-ft^2-°F was calculated using Eq. (5.1). This value was

compared to a theoretical value based upon the same test conditions. The theoretical value is expressed as

$$h_{theor.} = h_{NC} + h_{RAD} \qquad (5.3)$$

where

h_{NC} = the theoretical natural convection heat transfer coefficient for a vertical plate in air

= $0.29(\Delta T/L)$ [18]

h_{RAD} = the theoretical radiation heat transfer coefficient

= $4F \sigma T^3_{mean}$ [18] .

Using this expression with the same measured parameters of the test and an assumed emissivity of oxidized copper of 0.25 [18] yields an $h_{theor.}$ of 1.21 Btu/hr-ft^2-°F. This compares very well with the experimentally determined value having an error of approximately 1%. However, caution must be exercised in relying heavily on the results of this particular check due to the uncertainty of the assumed emissivity value of copper.

The second method utilized to check the performance of the wall heater consisted of orienting the heater unit in stationary air as before but covering the copper plate with a material of known thermal conductivity and thickness. A heat flux was generated and the temperature difference across the covering material was measured. This measured value of ΔT is then compared to a theoretically determined value from

$$\Delta T = \frac{q\ell}{kA} \tag{5.4}$$

Extruded polystyrene foam insulation was obtained having a conductivity measured by the supplier using a guarded hot plate traceable to NBS standards of 0.017 Btu/hr-ft^2-°F at 75°F and a thickness of 0.0104 ft. [25]. The insulation was placed over the heater, a heat flux through the heater was generated, and a temperature difference of 40°F across the insulation was measured using copper/constantan thermocouples. Substituting the appropriate known and measured values into Eq. (5.4) a $\Delta T_{theor.}$ of 40.3°F is determined. Again, good agreement exists between the actual and theoretical values to an error of approximately 1%.

A second check of this method was conducted on air flowing at approximately 1.5 fps. This air velocity was selected as an estimated average test velocity in the designed fluidized bed experiments. Under these conditions, and using the same heat flux as before, a ΔT across the insulation of 39°F was measured. This results in an error of approximately 2.8%.

The tube heater performance was similarly checked in stationary and flowing air using the insulation covering method outlined above. In the stationary air case a ΔT of the insulation of 83°F was measured. This value compared to the theoretical ΔT of 84.5°F yields an error of approximately 1.8%. In the flowing air case ($U_0 \tilde{=}$ 1.5 fps) an error of 3% resulted.

As a consequence of these tests it has been concluded that the heaters perform within an acceptable range of experimental accuracy and as designed. Furthermore, it appeared that any heat loss due to

two-dimensional conduction effects is negligible. It is also important to note that the k/ℓ value of the insulation (1.5-2.0 Btu/hr-ft^2-°F) used in these checks is approximately an order of magnitude less than the heat transfer coefficient expected in the fluidized bed experiments. It is to be expected, then, that for the same heat flux generated as in the checks the heat transfer rate will be greater for the bed and, thus, the resulting error would decrease. A discussion of the range of experimental accuracy is presented in the next section.

5.4 Estimation of Experimental Error

Section 5.3 has outlined the procedures and results associated with checking the heating performance of the wall and tube heaters. The results from this are, however, only part the overall estimation of the experimental error. This section will outline the procedure used in estimating this error.

There exists a certain amount of inherent error in any measured data. Since the heat transfer coefficients, h, in this work are determined by Eq. (5.1), the error in the measured values of the heat flux transferred, q, the tube and flat plate area, A, and the wall and bed temperatures, T_W and T_B, affect the error in the calculated heat transfer coefficient. Additionally, since air velocities through the fluidized beds and pressure readings are also required, the error involved in these measurements must be accounted for. The method that is used to determine this experimental error is outlined in reference [26].

The accuracy of the meters used to measure the voltage and amperage used in determining q is 1% and 2% respectively of full scale deflection. Since q = voltage x amperage - leaks, the error, e_q, in the measured q may be calculated by

$$e_q = (e_{VOLT}^2 + e_{AMP}^2 + e_{LEAK}^2)^{1/2} \qquad (5\text{-}5)$$

For both heaters the voltage and current error band is $e_{VOLT} = 2\%$ and $e_{AMP} = 4\%$. As discussed in Section 5.3 the wall heater and tube heater have an $e_{LEAK} = 2.8\%$ and 3% as a worst case, respectively. Consequently, the error, e_q, in the measured q is 5.3% for the wall heater and 5.4% for the tube heater.

Heater dimensions were measured by a micrometer, varied by 0.4%, and thus have a 0.4% error band for the area.

Temperatures were measured by copper/constantan thermocouples to an accuracy of $\pm$ 1°F. This results in an error of 1.4°F for the temperature difference between the wall and the bed material. Assuming an average value of $(T_w - T_B)$ of 60°F for both heaters, this results in a 2.3% error in the measurement of the temperature difference.

Therefore, the net error associated with the determination of h in this work is the square root of the sum of the squares of the errors of the individual contributors to h :

$$\text{Error of } h \text{ (wall)} = [(5.3)^2 + (.4)^2 + (2.3)^2]^{1/2} = 5.8\%$$

$$\text{Error of } h \text{ (tube)} = [(5.4)^2 + (.4)^2 + (2.3)^2]^{1/2} = 5.9\% \quad .$$

The error associated in the measurement of air velocity can be estimated using the same procedure as that used for the heat transfer

coefficient. As shown in Appendix D, air velocity, U_0 , is a function of air properties and orifice plate geometry, static pressure, P_1 , pressure drop, ΔP , and temperature T_1 . Orifice plate geometry was measured by a vernier caliper having an 0.4% error band. Static pressure was measured from a pressure gauge with an accuracy of ± 0.1 psi. Assuming an average static pressure of 18 psi, the resulting error is 1.1%. The pressure drop was measured using a water-filled U-tube manometer accurate to ± 0.1 in. of water. Assuming an average ΔP of 8 in. of water, this results in an error of 2.5%. Temperature was measured using a standard thermometer accurate to 1°C. Assuming an average air temperature of 27°C the corresponding error is 3.7%. Utilizing these individual error values the net error associated with the measurement of air velocity is 4.6%.

Lastly, the fluidized bed pressure drops were measured using an inclined oil-filled manometer accurate to ± .01 in. of water. Assuming an average bed pressure drop of 1 in. of water, there results a 2% error in measurement. Table 5.1 summarizes errors associated with all the measured quantities discussed in this section.

TABLE 5.1

EXPERIMENTAL ERROR SOURCES

ITEM	ACCURACY	
	Wall Heater	Tube Heater
Heat Transfer Rate		
Voltage	± 1%	± 1%
Amperage	±2%	± 2%
Leakage	2.8%	3%
Heater Area	0.4%	0.4%
Temperature		
Thermocouples	± 1°F	± 1°F
Difference	2.3%	2.3%
Velocity		
Orifice Plate	0.4%	0.4%
Static Pressure	1.1%	1.1%
Pressure Drop	2.5%	2.5%
Temperature	3.7%	3.7%
Fluidized Bed		
Pressure Drop	2%	2%

CHAPTER 6

ANALYSIS AND DISCUSSION OF EXPERIMENTAL RESULTS

This chapter will discuss in detail the experimental results presented in Chapter 5. Of concern in this investigation is both the fluidization and heat transfer characteristics of the test particles as compared with the theoretical predictions outlined in Chapter 2. Although closely related, the heat transfer and fluidization subjects will be treated separately in this chapter for the purpose of clarity. All analyses are based upon the detail presented in Chapter 3.

6.1 Fluidization Studies

Fluidization studies have been conducted primarily through visual observation and through measurements taken as described in Chapter 5. Topics of this section present the fluidization results in terms of the Geldart classification, the presence of material static electrification, fluidized bed pressure drops, air pumping power requirements, and the effect of particle diameter and density on minimum fluidization velocities. Table 6.1 lists these results.

6.1.1 Geldart Classification

Chapter 2 presented the general philosophy behind Geldart's materials classification according to their fluidization characteristics. This classification, however, was based on materials significantly more dense and generally of smaller diameter than the material studied in this work (see Figure 2.1). It is, therefore, of interest to see whether the general trends predicted by Geldart's classification can be applied to

TABLE 6.1 TEST MATERIAL FLUIDIZATION CHARACTERISTICS

PARTICLE	ρ [pcf]	(1) $\bar{d}_p$ [in]	(2) $\bar{U}_{mf}$ [fps]	(3) $\overline{\Delta P}_B$ [psf]	(4) P/A [HP/ft^2]
Norton 650	31.8	0.026	0.24	12.71	0.029
Macro M40X	27.2	0.039	1.04	13.73	0.136
Norton 1	23.2	0.039	0.57	10.61	0.057
Norton 1.5	20.9	0.059	0.75	9.44	0.067
Macro M27X	15.3	0.078	1.59	8.42	0.127
Perlite 250	4.5	0.010	0.011	1.60	3.2×10^{-5}
Perlite 500	2.7	0.020	0.016	1.01	2.97×10^{-5}

NOTES: (1) $\bar{d}_p$ = mean particle diameter

(2) $\bar{U}_{mf} = \frac{1}{2}(U_{mf}$ (2-D Bed) $+ U_{mf}$ (3-D Bed)$)$

(3) $\overline{\Delta P}_B = \frac{1}{2}(\Delta P_B$ (2-D Bed) $+ \Delta P_B$ (3-D Bed)$)$/ft. of bed height

(4) P/A $\equiv$ Air pumping power per unit bed cross-section area at U_{mf}

$= U_{mf}(\Delta P_B)$

All quantities are experimentally measured.

larger, less dense materials in order to be a further aid in fluidization engineering or fluidized bed design. In this section each test particle's fluidization characteristics will be discussed and compared to Geldart's classification. Additionally, the non-test particles described in Chapter 5 will be evaluated. Table 6.2 is a summary of these results.

The Norton 650 particles exhibit very good fluidization characteristics. As shown in Fig. E.1, they have an average experimentally determined minimum fluidization velocity, U_{mf}, of 0.24 fps and bed pressure drop per foot of height, ΔP_B of 12.75 psf. Bubbling commences in this material slightly above the minimum fluidization velocity. Based upon experimental observations and testing, Norton 650 is best described by Geldart's Group B fluidization classification. It also obeys Eq. (2.4) which Geldart uses to describe a Group B particle. In general, Geldart's classification criteria satisfactorily describes this material.

The Macro M40X particles also exhibit good fluidization characteristics. Figure E.2 shows that this material has an average U_{mf} of 1.04 fps and a ΔP_B of 13.77 psf. Again, bubbling appears to commence slightly above minimum fluidization. As with the Norton 650 material, the Macro M40X particles are best described experimentally by and satisfy the analytical expression for Geldart's Group B classification. Thus, it can be concluded that Geldart's classification also satisfactorily describes this material.

The Norton 1 material fluidizes well. Bubbles commence slightly above minimum fluidization. It has an average U_{mf} and ΔP_B of 0.57 fps and

TABLE 6.2 GELDART MATERIAL CLASSIFICATION COMPARISON

PARTICLE	$\Delta\rho$ [kg/m^3]	d_p [μm]	DESCRIPTION	
			GELDART	EXPERIMENT
Norton 650	507.8	650	B	B
Macro M40X	434.4	1000	B	B
Norton 1	370.4	1000	B	B
Norton 1.5	332.7	1500	B	B
Macro M27X	244.0	2000	B/D	B
Q-Cell	175.0	~ 70	A/C	C
Perlite 250	70.9	250	A	A
Perlite 500	42.0	500	A	A
Styrofoam Beads	36.4	3000	B/D	C

10.64 pcf, respectively, as illustrated in Fig. E.3. As with the preceding materials, Geldart's Group B classification satisfactorily describes the fluidization characteristics of Norton 1.

The next group of test particles, Norton 1.5, also demonstrates good fluidization characteristics showing bubble commencement slightly above minimum fluidization. This material has an average U_{mf} of 0.75 fps and a ΔP_B of 9.48 pcf (Fig. E.4). Its fluidization characteristics are well described by the Group B description and it satisfies Eq. (2.4). Again, the Geldart classification provides a satisfactory description of this material.

The Macro M27X material fluidizes fairly well, although not as well as the preceding test materials. This material, primarily due to its particle diameter, requires the greatest amount of air velocity for fluidization (1.59 fps). As a consequence of this, bubble diameters appear to be larger and the bed fluidization is more violent. However, due to its lower particle density, this material has a lower ΔP_B than the preceding test materials (8.45 pcf) as shown in Fig. E.5. This material is not very well described by Geldart's materials classification. It appears to be somewhere between the Group B and D categories.

On the other hand, both the Perlite 250 and Perlit 500 materials fluidize well. They exhibit some bed expansion before the onset of bubbling. The Perlite 250 has an average U_{mf} of 0.011 fps and a ΔP_B of approximately 1.60 pcf (Fig. E.6). The Perlite 500 has an average U_{mf} of 0.016 fps and a ΔP_B of 1.02 psf (Fig. E.7). Their fluidization is hampered, though, by their tendency to attain and hold a triboelectric charge. This is most apparent when the particles are in contact with the

plexiglas front walls of the fluidized beds. As discussed in Appendix C, both perlite and plexiglas are dielectrics and thus have relatively small susceptabilities available for this triboelectric charging to take place. Perlite in contact with the metal and wooden walls does not present this problem. The attraction between the perlite and the plexiglas is not enough to seriously hamper the perlite's fluidization characteristics, but it may pose a heat transfer problem. Perlite 250, moreover, tends to exhibit a greater attraction to the plexiglas than the Perlite 500.

Despite this triboelectrification problem, though, both perlites are best categorized by Geldart's Group A description (but graphically appear in Group C). Thus, it appears that his materials classification narrative descriptions can also apply to this category of material.

In summary, then, Geldart's material classification according to fluidization characteristics seems to hold adequately for the lower density and particle diameter materials used in this investigation. His initial criteria based on ranges of particle diameters and densities for the four fluidization groups, however, needs to be modified to include the appropriate diameters and densities of these test materials.

Before concluding this topic, though, a discussion of two materials initially investigated in this work whose fluidization characteristics are not well described by Geldart's material classification is in order. These two materials are the styrofoam beads and the Q-cell [27] (small diameter, moderate density) material described in Chapter 5.

Considering the material density and particle diameter of the styrofoam beads and Eqs. (2.4) and (2.5) one would predict, based upon Geldart's classification, that this material would be in the Group B/D range, being very close to Group D. In experimental investigation,

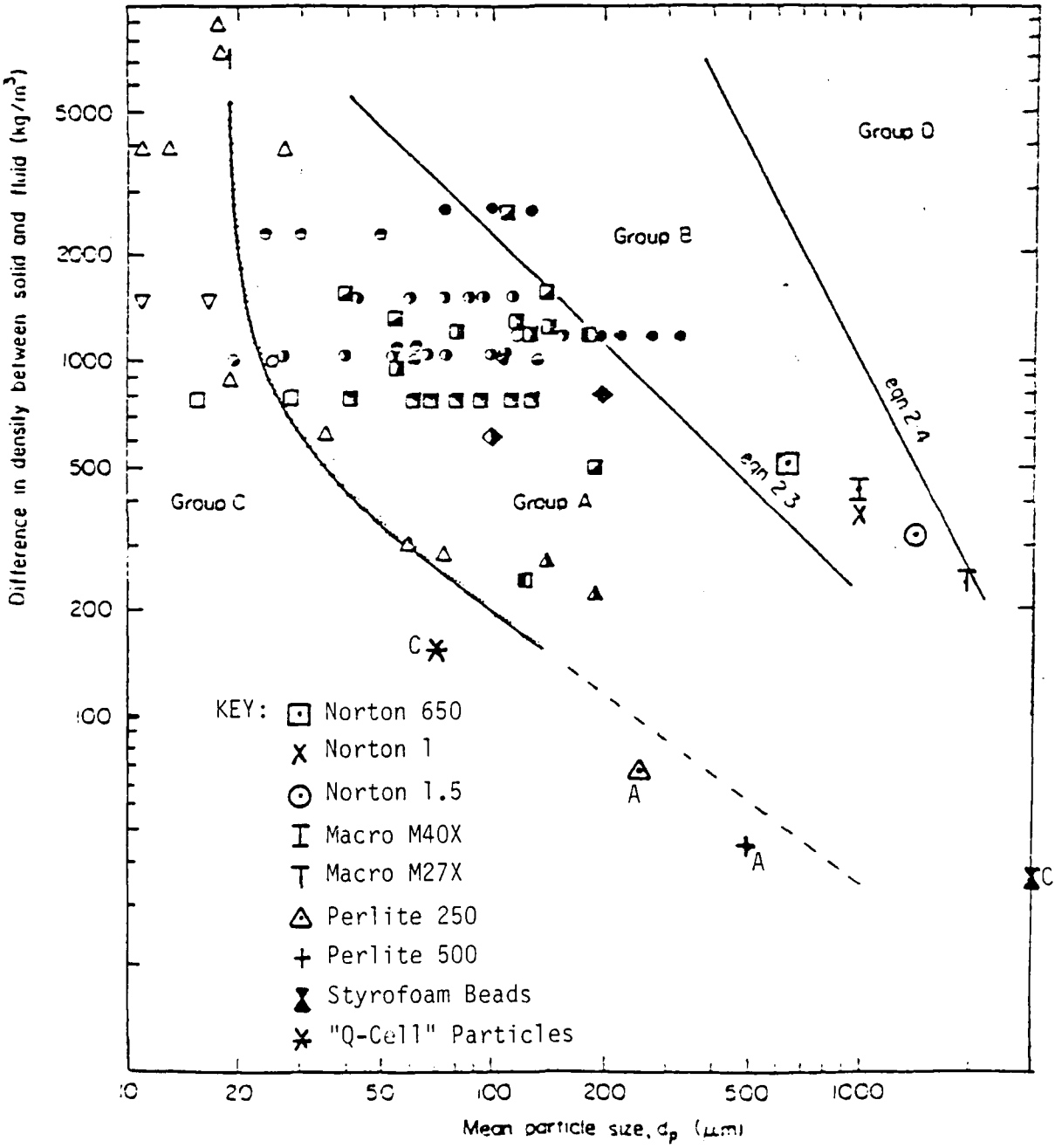

FIGURE 6.1 Test Material Geldart Classification

however, this material exhibited some bed expansion, displayed excessive triboelectric charging and in general fluidized poorly. This fluidization characteristic is best described as a Geldart Group C material and not the predicted Group D.

The second unpredicted material is the "Q-Cell" material of mean particle diameter of 70 μm and density of 11 pcf. Given this data, one would predict the material to fall generally into the Group A region due to the mean particle diameter criteria. In reality, however, this material fluidizes very poorly and seems to be better represented by Group C. It is interesting to note that if the classification of this material was based on Figure 2.1 alone, the Group C classification would be accurately predicted. If, however, the classification was based on particle density and diameter, without reference to Figure 2.1, a Group A classification would be predicted. Figure 6.1 shows these test results along with those previously reported by Geldart.

Thus, it appears that care must be exercised in using the Geldart materials classification on the very extremes of the low density region, that is, at the very large particle diameter (2500 μm) and the very small diameter (50 μm) areas and when fluidizing materials where conditions exist for the creation of significant triboelectric charging.

6.1.2 Air Pumping Power Requirements

This section is of interest due to the intended applications of this work in solar collector and heat exchanger technology. The analysis presented here will be further utilized in Section 6.2 and in Chapter 7. The external air pumping power required to operate a fluidized bed is, in itself, not a fluidization characteristic of a material but rather a result of certain characteristics.

In general, air pumping power, $\underline{P}$, is a function of air mass flow rate, $\dot{m}$, pressure drop, ΔP, and density, ρ

$$\underline{P} = \frac{\dot{m}\ \Delta P}{\rho} \tag{6.1}$$

Defining $\dot{m} = U_0 A$ and substituting into and rearranging terms in Eq. (6.1) yields

$$\underline{P}/A = U_0 \Delta P_B \tag{6.2}$$

which expresses air pumping power per unit cross-sectional area. Substituting Eq. (2.2) into Eq. (6.2) results in an expression for $\underline{P}/A$ in terms of fluidized bed characteristics at $U_0 \geq U_{mf}$

$$\underline{P}/A = U_0 L(1 - \varepsilon)(\rho_s - \rho_g) \frac{g}{g_c} \tag{6.3}$$

Consequently, either Eqs. (6.2) or (6.3) may be used to express the air pumping power requirement per unit bed cross-sectional area.

As expressed by Eq. (6.2), $(\underline{P}/A)$ is linearly proportional to the product of the air velocity through the bed and the bed pressure drop. Thus, in order to minimize $(\underline{P}/A)$ for solar collector and heat exchanger applications, this product must be minimized. Air velocity may be minimized to slightly above minimum fluidization velocity. Therefore, materials with a small U_{mf} will result in a lower $(\underline{P}/A)$. The material parameters affecting U_{mf} are discussed in Section 6.1.3.

Bed pressure drop, as shown in Eq. (2.2), is strongly affected by the material density. Generally speaking, lower density material will yield a

smaller ΔP_B . Thus, low density material will also aid in yielding low $(\underline{P}/A)$ values. Table 6.1 shows this trend for $(\underline{P}/A)$ values evaluated at $U_0 = U_{mf}$.

Consequently, desirable materials for low $(\underline{P}/A)$ values should have both low U_{mf} and density characteristics. As shown in Table 6.1, the Norton 650 and the Perlites in this work require the lowest $(\underline{P}/A)$ value.

6.1.3 The Effect of Particle Diameter and Density on U_{mf}

In Chapter 2 it was shown that Kunii and Levenspiel, using the correlation of Eq. (2.3), have analytically expressed U_{mf} in terms of, primarily, particle diameter and density. They stress that this relation is only approximate and valid for uniformly sized material. The test particles in this work are not of constant particle diameter and this equation cannot be applied directly. However, this expression is useful in interpreting data.

Specifically, Eq. (2.3) shows that U_{mf} is a function of $(d_p)^2$ and ρ_s . Thus, solely based on this relation, one would expect particle diameter to have a stronger effect on U_{mf} than particle density. As shown in Table 6.1, this is generally the case with the test materials of this investigation. The Macro M27X material (d_p = 0.078 in, ρ = 15.3 pcf) has a U_{mf} of 1.59 fps versus the Macro M40X (d_p = 0.039 in, ρ= 27.2 pcf) with a U_{mf} of 1.04 fps demonstrates this effect. However, again care must be taken, for this trend is not an absolute as illustrated by comparing the Macro M40X and the Norton 1.5. It appears that at relatively close particle diameters density becomes significant in determining U_{mf} .

Using this conclusion, lower U_{mf} values should correspond to smaller particle diameters. Since, as discussed in Section 6.1.2, the $(\underline{P}/A)$

values required to fluidize a bed of particles is of concern in this work, a minimization of this value will also result in using smaller diameter materials. Consequently, the best possible combination of properties that a material could have in order to minimize air pumping power is a low density and small particle diameter. In actuality, though, this criteria presents a problem. In the manufacturing of low density materials, particle diameter is usually varied by expanding the material with air or another gas. As a result, for a specific group of materials lower density corresponds to larger particle diameter. This is identically the case for all the test particles in this work for small $(\underline{P}/A)$. This fact also makes simple material selection based on low diameter and density difficult. It is necessary to test various combinations of diameter and density to determine the minimum value. In this work, for example, Perlite 500 has the lowest $(\underline{P}/A)$ value (at $U_0 = U_{mf}$) even though it does not have the smallest particle diameter. Table 6.3 compares the theoretical to experimental values of the test materials U_{mf} and ΔP_B.

6.2 Heat Transfer Studies

Heat Transfer studies of the test material have been conducted for the wall flat plate, immersed tube, and finned immersed tube cases in accordance with the procedures outlined in Chapter 5. The data collected is presented in Figs. 6.2 through 6.4 and is correlated and analyzed in this section based upon the theory developed in Chapters 2 and 3. Additionally, this section will discuss the experimental results of particle diameter, density, air velocity and bed obstructions on heat transfer coefficients, and conclude with a discussion on how heat transfer compares with air pumping power for the low density materials used in this investigation.

TABLE 6.3 A COMPARISON OF THEORETICALLY PREDICTED AND EXPERIMENTALLY DETERMINED MINIMUM FLUIDIZATION VELOCITIES AND BED PRESSURE DROPS

MATERIAL	$(U_{mf})_{th}^{(1)}$	$(U_{mf})_{exp}$	$(\Delta P_B)_{th}^{(2)}$	$(\Delta P_B)_{exp}$
Norton 650	0.20	0.24	12.68	12.71
Norton 1	0.35	0.57	11.56	10.61
Norton 1.5	0.71	0.75	10.39	9.44
Macro M40X	0.72	1.04	13.56	13.73
Macro M27X	0.90	1.59	7.62	8.42
Perlite 250	0.005	0.011	1.77	1.60
Perlite 500	0.01	0.016	1.05	1.01

NOTES: (1) Units of fps

(2) Units of psf per ft height of bed.

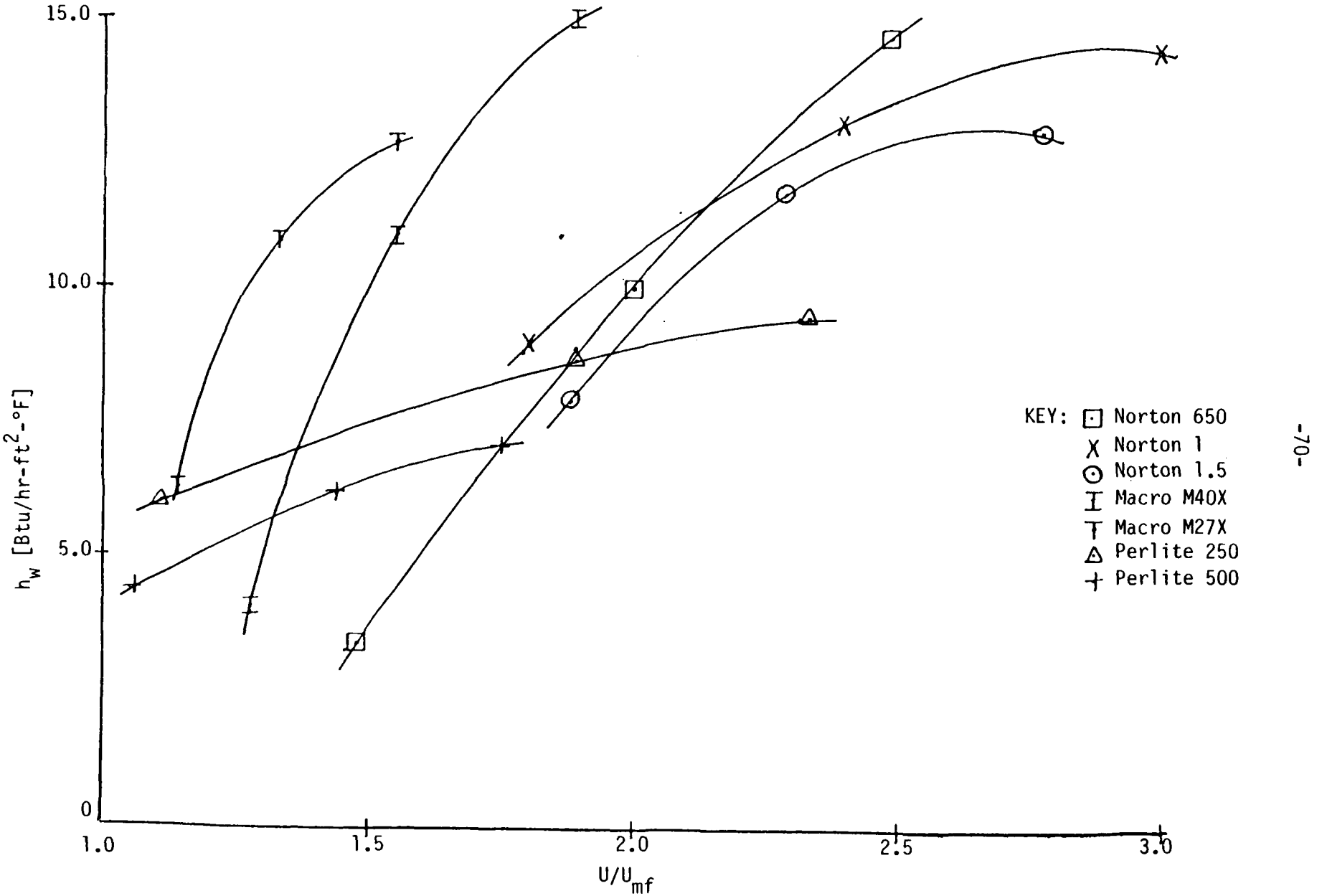

FIGURE 6.2 Test Material Wall Heat Transfer Coefficients

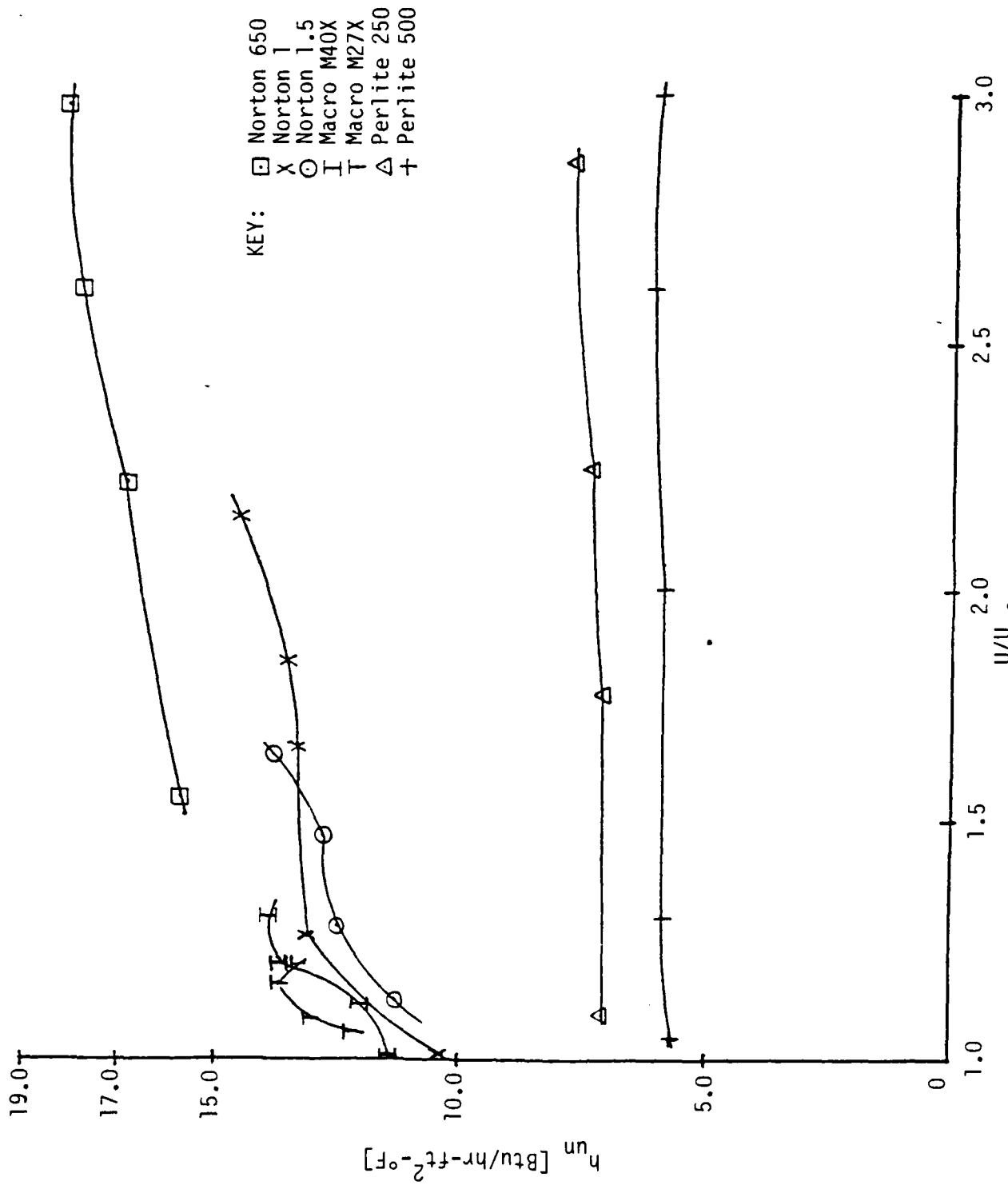

FIGURE 6.3 Test Material Unfinned Tube Heat Transfer Coefficients

FIGURE 6.4 Test Material Finned Tube Heat Transfer Coefficients

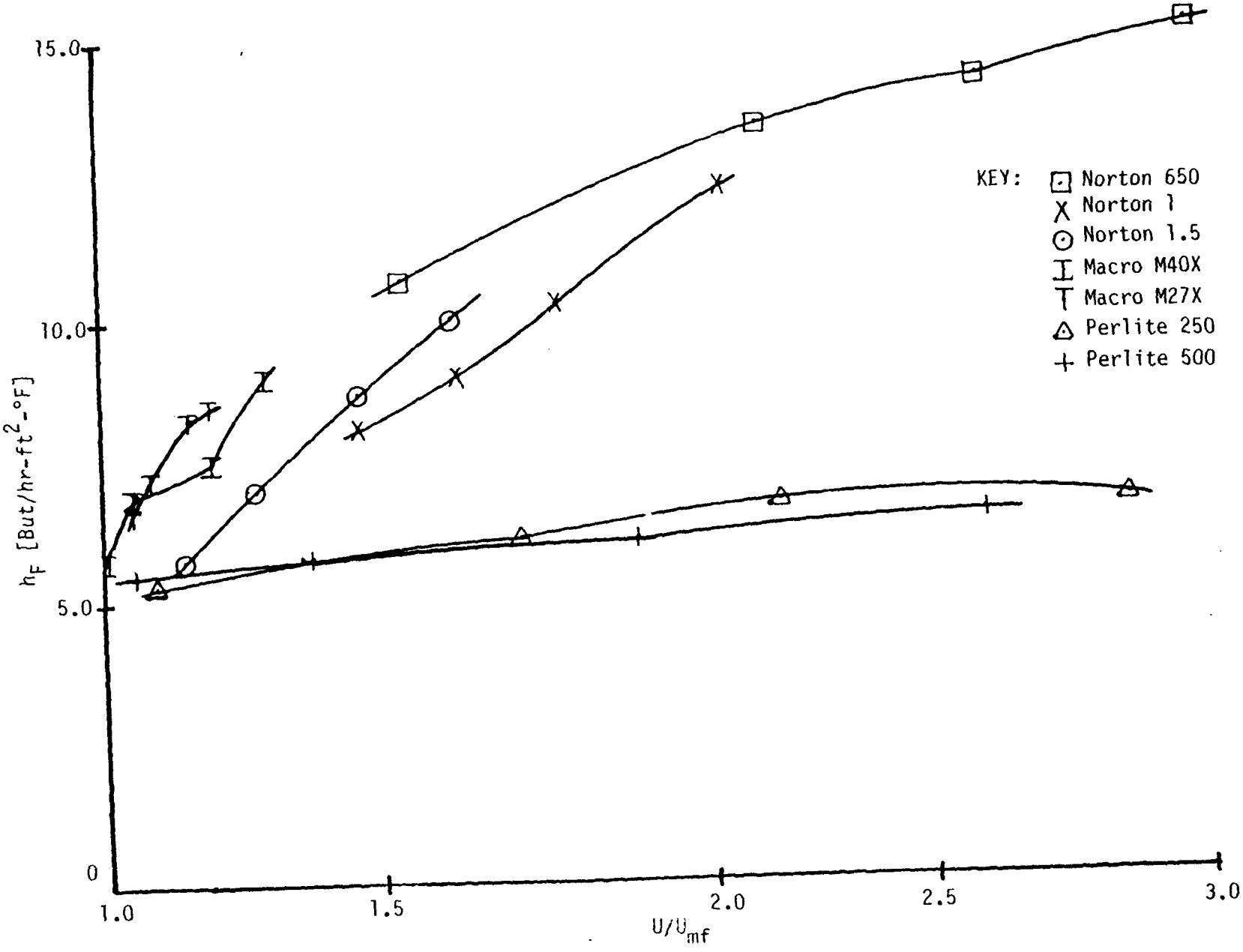

6.2.1 Theoretical Comparison

The analysis presented in this section considers the actual experimental heat transfer accomplished for each low density test material and compares those results to theoretical predictions. From this comparison general trends and conclusions are developed. Each heating geometry is discussed separately.

Wall Heat Transfer

In Chapter 3 the specific theoretical relationships applicable to this work have been outlined. However, no reference to the particle-to-surface residence time, t_r of Eq. (2.6) is made. Quantifying this value has traditionally been difficult. In this work no detailed procedure has been used to determine the residence times. Its value for use in Eq. (2.6) for this analysis is assumed, based on visual observation and typical values determined by other investigators [17]. With this in mind, for the wall heat transfer case, the following particle-to-surface residence times have been used:

Particle Group	U/U_{mf}	t_r (sec)
Macro and Norton	1.0 - 1.5	0.8
	1.51 - 2.0	0.7
	2.01 - 2.5	0.6
	2.51 +	0.5
Perlite	1.0 - 1.5	0.5
	1.51 - 2.0	0.4
	2.01 +	0.3

The difference in times between the two groups is based primarily on experimental observation. It was visually detected that the Perlite

materials exhibited more rapid mixing during fluidization than did the Macro and Norton materials. As a result, there appeared to be a significant decrease (on the order of one half) in wall residence time with the Perlite as compared with the other test material. Although the actual reason for this is not exactly known, it is probably a result of the different fluidization characteristics of Perlite (Geldart Group A) versus the other materials (Geldart Group B). Although this one observation cannot be considered conclusive, further and more detailed investigations into the role of material fluidization classification on particle-to-wall surface residence time may be appropriate.

Having assigned these residence times to the appropriate ranges of U/U_{mf}, a theoretical wall heat transfer coefficient has been numerically determined for each test material. These results are listed in Table 6.4 and graphically depicted in Fig. 6.5. Also listed in the table are the corresponding experimentally determined wall heat transfer coefficients from the data presented in Figs. 6.2 through 6.4. These experimental wall heat transfer coefficients are with obstructions placed in the bed (see Section 6.2.4).

As illustrated in Table 6.4 and Fig. 6.5, there exists a fairly good correlation between the theoretically predicted wall heat transfer coefficients, h_{theor}, to those that have been measured experimentally, h_{exp}. However, some departures do exist.

These departures from theory are all in the lower U/U_{mf} areas of the Group B materials. An actual comparison of only U/U_{mf} values for these departures reveals no specific limit or trend for which all particles exhibit this poor correlation. However, there does seem to exist a general trend when comparing the value of the air velocity through the bubbles

TABLE 6.4 WALL HEAT TRANSFER DATA

PARTICLE	U/U_{mf}	$(U-U_{mf})$	h_{void}	h_e	h_{rad}	h_w (6 12)	h_{surf}	h_{theor}	h_{exp}	h_{exp}/h_{theor}	t_{req}
Norton 650	1.58	0.13	3.93	26.47	0.38	88.84	20.39	17.92	3.40	0.23	44
						45.18	16.64	14.73			
	2.00	0.27	4.07	28.30	0.35	88.81	21.46	18.85	10.02	0.65	2.6
						45.15	17.40	15.40			
	2.48	0.40	4.20	30.57	0.33	88.79	22.74	19.96	14.63	0.91	
						45.13	18.22	16.12			
Macro M40X	1.28	0.31	6.05	27.38	0.38	62.09	19.00	16.41	4.09	0.31	42
						33.74	15.11	13.30			
	1.55	0.61	6.25	29.27	0.34	62.05	19.89	17.16	11.01	0.80	
						33.70	15.66	13.78			
	1.89	0.98	6.48	29.27	0.32	62.03	19.89	17.21	15.04	1.09	
						33.68	15.66	13.83			
Norton 1	1.80	0.47	5.08	27.04	0.36	59.75	18.61	15.91	9.06	0.72	2.3
						31.40	14.53	12.64			
	2.39	0.82	5.34	29.20	0.33	59.72	19.61	16.76	13.10	0.99	
						31.37	15.12	13.17			
	2.90	1.12	5.56	31.99	0.32	59.71	20.83	17.77	14.43	1.05	
						31.36	15.84	13.78			

TABLE 6.4 (Cont'd.)

PARTICLE	U/U_{mf}	$(U-U_{mf})$	h_{void}	h_e	h_{rad}	$h_w \left(\frac{12}{6}\right)$	h_{surf}	h_{theor}	h_{exp}	h_{exp}/h_{theor}	t_{req}
Norton 1.5	1.88	0.66	5.58	25.63	0.37	41.59	15.86	13.81	7.92	0.74	2.5
						22.68	12.03	10.75			
	2.28	0.96	5.79	27.68	0.33	41.55	16.61	14.45	11.82	1.06	
						22.64	12.45	11.12			
	2.77	1.33	6.03	30.32	0.33	41.55	17.53	15.23	12.96	1.12	
						22.64	12.96	11.58			
Macro M27X	1.14	0.26	7.39	20.54	0.36	37.22	13.24	12.07	6.31	0.62	5
						23.05	10.86	10.17			
	1.33	0.62	7.58	20.54	0.32	37.18	13.23	12.10	10.88	1.07	
						23.01	10.85	10.20			
	1.55	1.03	7.79	21.96	0.32	37.18	13.81	12.60	12.69	1.20	
						23.01	11.24	10.55			

TABLE 6.4 (Cont'd.)

PARTICLE	U/U_{mf}	$(U-U_{mf})$	h_{void}	h_e	h_{rad}	$h_w\left(\begin{smallmatrix}12\\6\end{smallmatrix}\right)$	h_{surf}	h_{theor}	h_{exp}	h_{exp}/h_{theor}	t_{req}
Perlite 250	1.11	.001	3.20	8.07	0.38	227.59	7.79	7.10	6.08	0.88	
						114.17	7.54	6.89			
	1.89	.01	3.29	9.01	0.34	227.55	7.37	7.86	8.72	1.15	
						114.13	8.35	7.59			
	2.33	.015	3.33	10.41	0.33	227.54	9.95	8.96	9.50	1.10	
						114.12	9.54	8.61			
Perlite 500	1.06	.001	3.45	6.24	0.40	114.49	5.92	5.55	4.43	0.83	
						57.78	5.63	5.31			
	1.44	.01	3.52	6.24	0.36	114.45	5.92	5.56	6.19	1.16	
						57.74	5.63	5.32			
	1.75	.012	3.57	6.98	0.35	114.44	6.58	6.13	7.13	1.22	
						57.73	5.23	5.84			

NOTES: 1) $(U-U_{mf})$ units are fps.

2) h units are Btu/hr-ft^2-°F

3) h_{exp}/h_{theor} based on $Nu_{COND} = 6$.

4) t_{req} units are sec.

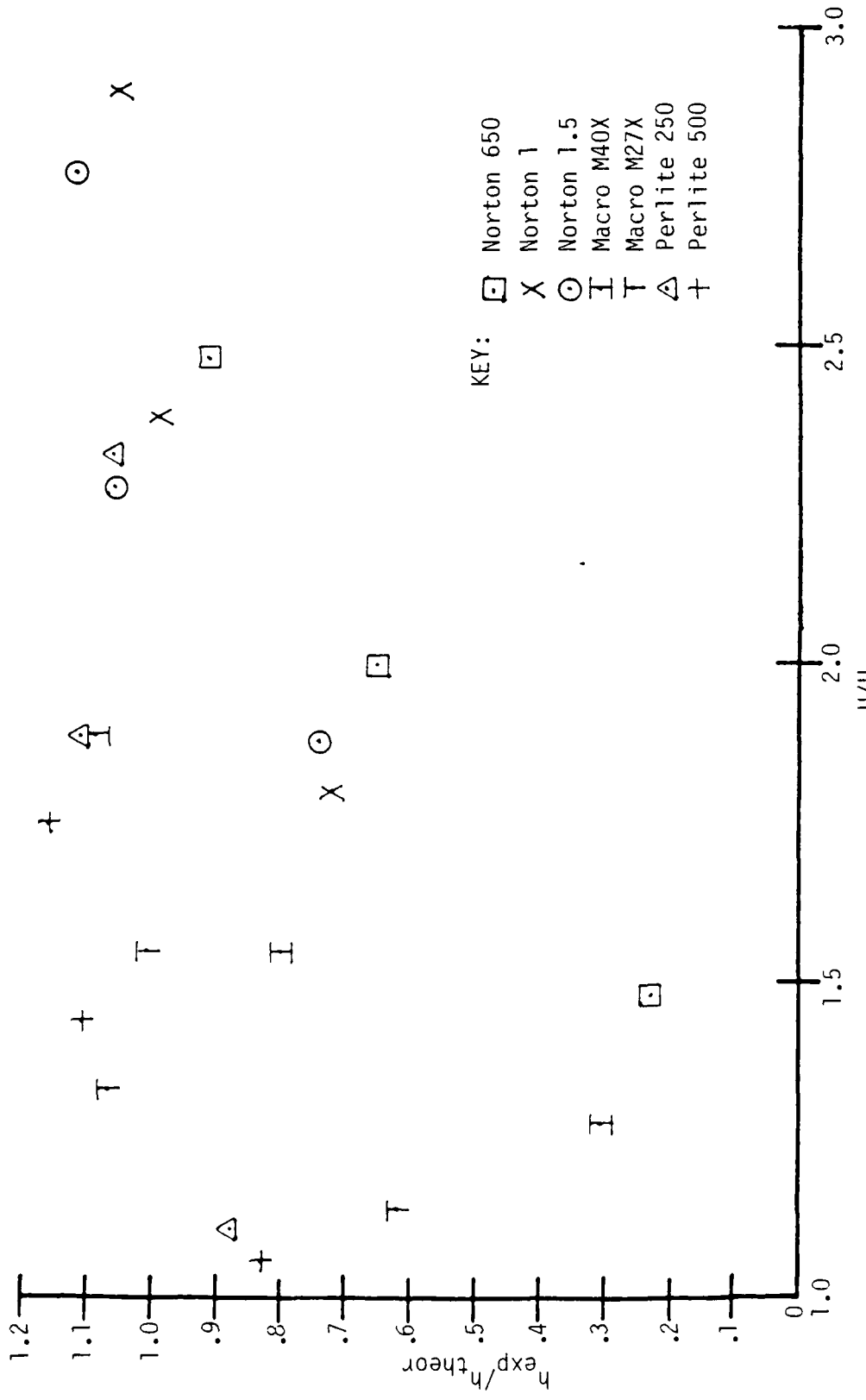

FIGURE 6.5 Test Material Wall Heat Transfer Coefficients - Experimental vs. Theoretical

formed in each material, $(U_0 - U_{mf})$. This data indicates that when the $(U_0 - U_{mf})$ values are less than 0.4 fps all of the Group B materials exhibit poor heat transfer correlations with theory. Conversely,when the value is above 0.7 fps all Group B materials exhibit good correlation with theory. Between these two values of $(U_0 - U_{mf})$ theoretical correlation is apparently dependent upon particle diameter and density. Density is important when particle diameters are approximately equal, in which case the greater density material requires the greater value of $(U_0 - U_{mf})$ for theoretical correlation.

Poor theoretical correlation with the actual results at the low $(U_0 - U_{mf})$ values of these low density, large diameter Group B materials suggests that the heat transfer model as expressed by Eq. (2.7) may not be accurate for this region. Air velocity affects the bed heat transfer, according to the model, most significantly in the emulsion and wall heat transfer. The emulsion heat transfer coefficient, h_e, sees this effect via the particle residence time. As discussed earlier, for a given fluidized material greater air velocity will yield greater particle mixing, and, thus, lower particle-to-surface residence times. If the model is assumed to be correct, then the assumed residence time values used to determine h_e must be inaccurate. However, the residence times required for good correlation at the low velocity values are generally longer than what was observed during experimentation. These required residence times, t_{req}, are listed in Table 6.4.

Air velocity is also a factor in the convective component of h_w. However, this is of secondary importance as compared to its effect on h_e due to the characteristically low air velocities involved with fluidizing this material. Also at these air velocities the convective component of

h_w is much smaller than the conduction component which, in turn, is not dependent upon air velocity at all.

Consequently, it must be concluded that at low air velocities some other physical mechanism may be taking place, other than the packet renewal theory used in this model, in order to account for the unpredicted low actual wall heat transfer coefficients. One possibility of this is that at these low air velocities particle packets may have moved along the heated surface for a finite length of time rather than simply, and rapidly, making contact and moving away. Experimental observations were made to this effect, but these extended residence times were on the order of 1-2 seconds for the effected particles at these velocities. This could account for some of the experimental heat transfer coefficent departures from theory but does not explain the results of the lowest velocity Norton 650 and Macro M40X data.

As mentioned earlier, the theory generally does well in predicting the wall heat transfer coefficients except for the departures discussed above. The data indicates that the use of the conduction Nusselt Number of 6 in h fits the data better than the value of 12 . Furthermore, it shows that the controlling resistance to heat transfer is primarily the emulsion component of the surface resistance. Again the importance of air velocity and particle-to-surface residence time becomes evident. Being the controlling parameter, h_e must be maximized in order to maximize the overall heat transfer from the wall to the fluidized material. To do this, air velocity can be increased or, in order to not simultaneously increase air pumping power requirements, obstructions can be placed on the wall or in the bed to enhance particle mixing and reduce particle residence time. This concept is discussed later in the chapter.

Of particular interest to the applications of this work due to its low density, moreover, is the Perlite material. Unlike the Group B material, the Perlite's (Group A) wall heat transfer coefficients through all ranges of (U/U_{mf}) are well predicted by the theory. Again the controlling heat transfer parameter is h_e but it plays an even more dominant role in the Perlite material than in the Group B materials. This suggests the increased importance in decreasing particle residence time to enhance heat transfer for the Perlite. Additionally, heat transfer enhancement may also be accomplished by taking measures to reduce the triboelectric affect exhibited by the Perlite and the plexiglas front wall. In effect, reducing the static attraction should enhance the fluidization next to the wall, and, thus, reduce the particle-to-surface residence time. It should be re-emphasized that the triboelectric phenomenon present in this situation was present with the Perlite against the plexiglas *only*, *not with* any other surface, to include the copper wall heater surface.

In summary, then, the data available for the the low density, large particles used in this investigation indicates that the heat transfer model represented by Eq. (2.7) generally does well in accurately predicting wall heat transfer coefficients. The controlling heat transfer coefficient tends to h_e . Problems do exist, however, with the Group B material at very low air velocities. This, in turn, suggests some other physical mechanism may be at work effecting their heat transfer.

Unfinned Tube Heat Transfer

As with the analysis of the wall heat transfer, the unfinned tube heat transfer analysis is based upon the relationships outlined in Chapter 3. The particle-to-tube residence times are assumed, based on typical values determined by other investigators [17], as follows:

Particle Group	U/U_{mf}	t_r(sec)
All	1.05	0.6
	1.05 - 1.10	0.5
	1.11 - 1.99	0.4
	2.00	0.3

Notice that in the immersed tube case the residence times versus U/U_{mf} apply to all particle groups. Contrary to the wall case, there was no experimental visual observation due to the immersed nature of the tube surface to suggest any changes in residence times between the different material fluidization groups was required.

Using these assumed residence time values, theoretical immersed tube heat transfer coefficients have been numerically determined for each test material. The results are listed in Table 6.5 along with the corresponding experimentally determined immersed tube heat transfer coefficients. The ratios of the individual experimental to theoretical heat transfer coefficients versus U/U_{mf} are graphically illustrated in Fig. 6.6.

As shown in Table 6.5 and Fig. 6.6 there is a very good correlation between the theoretical heat transfer coefficient predictions and the actual results for all materials. Except for the largest diameter particles (Macro M27X and Norton 1.5) the best data fit of the theory is with using the conduction Nusselt Number of 6. For the Macro M27X and the highest air velocity Norton 1.5 the conduction Nusselt Number of 12 provides a better estimate. This is not to say, however, that these materials exhibit greater heat conduction. The effect present here is

TABLE 6.5 IMMERSED TUBE HEAT TRANSFER DATA

PARTICLE	U/U_{mf}	h_{void}	h_e	h_{rad}	h_w ($^{12}_{6}$)	h_{surf}	h_{theor}	h_{exp}	h_{exp}/h_{theor}
Norton 650	1.55	3.65	37.43	0.14	88.31	26.29	22.89	15.70	
					44.65	20.36	17.86		0.88
	2.20	3.78	43.23	0.14	88.31	29.03	25.24	16.78	
					44.65	21.96	19.24		0.87
	2.60	3.86	43.23	0.14	88.31	29.02	25.25	17.69	
					44.65	21.96	19.25		0.92
	2.98	3.93	43.23	0.14	88.31	29.02	25.26	18.37	
					44.65	21.96	19.26		0.95
Macro M40X	1.30	5.68	38.72	0.14	61.26	23.72	20.12	13.90	
					32.90	17.79	15.37		0.90
	1.20	5.62	38.72	0.14	61.26	23.72	20.10	13.64	
					32.90	17.79	15.35		0.89
	1.07	5.53	34.63	0.14	61.26	22.12	18.81	12.08	
					32.90	16.87	14.61		0.83
	1.01	5.49	31.61	0.14	61.26	20.85	17.78	11.31	
					32.90	16.12	14.00		0.81
Norton 1	1.02	4.51	29.20	0.14	59.31	19.57	16.55	10.40	
					30.95	15.02	12.92		0.80
	1.26	4.62	35.76	0.14	59.31	22.31	18.77	13.12	
					30.95	16.59	14.19		0.92
	1.47	4.71	35.76	0.14	59.31	22.31	18.79	12.90	
					30.95	16.59	14.21		0.91
	1.65	4.79	35.76	0.14	59.31	22.31	18.81	13.28	
					30.95	16.59	14.23		0.93

TABLE 6.5 (Cont'd.)

PARTICLE	U/U_{mf}	h_{void}	h_e	h_{rad}	h_w ($^{12}_{6}$)	h_{surf}	h_{theor}	h_{exp}	h_{exp}/h_{theor}
Norton 1 (Cont'd.)	1.83	4.86	35.76	0.14	59.31 30.95	22.31 16.59	18.82 14.24	13.55	0.95
	2.33	4.99	41.29	0.13	59.30 30.94	24.37 17.75	20.50 15.20	14.47	0.95
Norton 1.5	1.15	5.09	33.90	0.14	41.36 22.45	18.68 13.51	15.96 11.83	11.22	0.95
	1.28	5.16	33.90	0.14	41.36 22.45	18.68 13.51	15.97 11.84	12.50	1.06
	1.47	5.27	33.90	0.14	41.36 22.45	18.63 13.51	15.95 11.85	12.75	1.08
	1.64	5.36	33.90	0.14	41.36 22.45	18.63 13.51	15.97 11.87	13.86	1.17
Macro M27X	1.06	6.20	25.98	0.14	34.45 20.28	14.81 11.39	13.09 10.35	12.20	0.93
	1.09	6.23	25.98	0.14	34.45 20.28	14.18 11.39	13.10 10.36	13.03	0.99
	1.16	6.28	29.05	0.14	34.45 20.28	15.76 11.94	13.87 10.81	13.73	0.99
	1.20	6.31	29.05	0.14	34.45 20.28	15.76 11.94	13.87 10.81	13.37	0.96

TABLE 6.5 (Cont'd.)

PARTICLE	U/U_{mf}	h_{void}	h_e	h_{rad}	h_w ($^{12}_{6}$)	h_{surf}	h_{theor}	h_{exp}	h_{exp}/h_{theor}
Perlite 250	1.11	3.29	9.01	0.15	227.51	8.67	7.86	7.09	
					114.09	8.35	7.59		0.93
	1.76	3.38	9.01	0.15	227.51	8.67	7.88	7.09	
					114.09	8.35	7.61		0.93
	2.23	3.45	10.40	0.15	227.51	9.95	8.98	7.28	
					114.09	9.53	8.62		0.84
	2.86	3.54	10.40	0.14	227.50	9.95	8.99	7.69	
					114.08	9.53	8.63		0.89
Perlite 500	1.06	3.41	6.24	0.15	114.24	5.92	5.54	5.67	
					57.53	5.63	5.29		1.07
	1.38	3.46	6.98	0.15	114.24	6.58	6.11	5.86	
					57.53	6.23	5.81		1.01
	1.97	3.57	6.98	0.14	114.23	6.58	6.12	6.92	
					57.52	6.23	5.83		1.02
	2.62	3.68	8.06	0.15	114.24	7.53	6.95	6.12	
					57.53	7.07	6.56		0.93
	3.06	3.75	8.06	0.14	114.23	7.53	6.96	6.05	
					57.52	7.07	6.57		0.92

NOTES: 1) h units are Btu/hr-ft^2-°F

2) h_{exp}/h_{theor} based on $Nu_{COND} = 6$

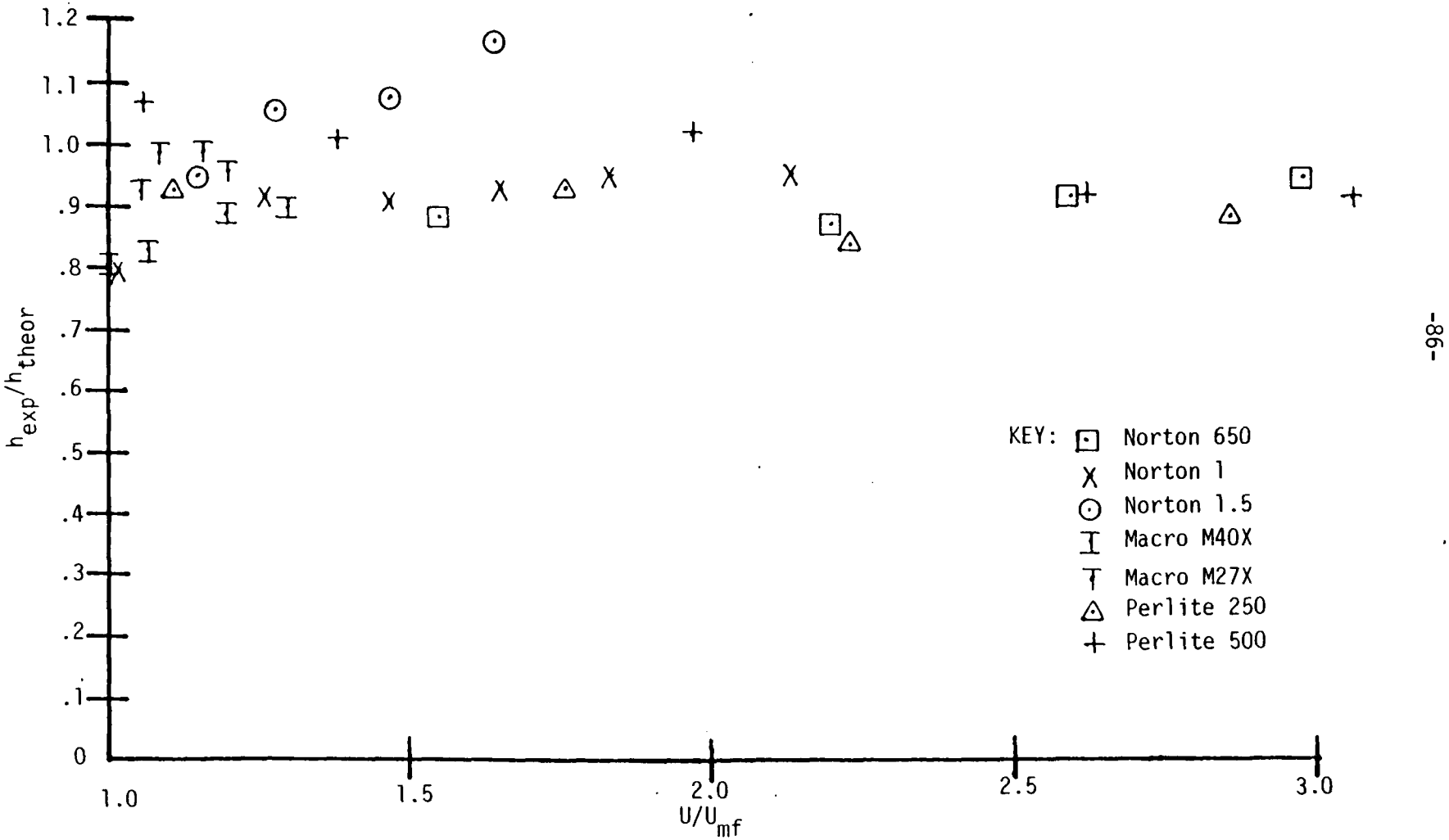

FIGURE 6.6 Test Material Unfinned Tube Heat Transfer Coefficients - Experimental vs. Theoretical

probably due to the increased role of convective heat transfer as a result of the increased air velocity through these particles relative to the other particles tested brought on by their larger size.

The data also indicates that for the Macro and Norton materials there is no definitively controlling resistance to heat transfer in the immersed tube case. Both h_e and h are generally of the same order. This suggests that enhanced heat transfer is best accomplished by increased air velocity and the use of smaller diameter particles, not necessarily through the use of flow abstructions.

On the other hand, the Perlite material data indicates that h_e is again the controlling parameter in determining the overall heat transfer coefficient. Thus, the same options discussed for enhancing wall heat transfer should apply to the immersed tube case for Perlite.

In summary, then, the data available for the low density, large particles used in this investigation indicates that the heat transfer model represented by Eq. (2.7) does well in predicting unfinned immersed tube heat transfer coefficients. For the Norton and Macro materials there appears to be no dominate resistance to heat transfer. The Perlite materials, however, have their heat transfer strongly controlled by h_e. The assumed particle residence times also appear to be valid.

Finned Tube Heat Transfer

The analysis of the immersed finned tube heat transfer proceeds similarly to that of the unfinned tube case. Of concern in these tests is the effect that the placement of fins on an immersed tube will have on its heat transfer compared to the unfinned case. Test air velocities and assumed particle-to-tube residence times for the finned tube experiments have been kept identical to the corresponding unfinned experiments.

Theoretical immersed finned tube heat transfer coefficients have been calculated for each test material using the surface efficiency modification procedure discussed in Chapter 3. Table 6.6 presents these results in conjunction with the corresponding experimentally determined finned tube heat transfer coefficients and the ratios of h_{exp} to h_{theor}.

The results of these experiments are not surprising. Using the same assumed particle-to-tube residence times as the unfinned case yields, in general, very poor theoretical correlation to experimental data. Acceptable correlation begins to exist (shown with a "*" in Table 6.6) at the smaller diameter particle level and at the higher air velocity regions of the intermediate diameter particles. The poor correlation is due to the decreased particle mobility between the fins in the larger particle cases. The decrased particle mobility translates directly to an increased particle-to-tube residence time than assumed and, thus, a lower value of h_e than would be predicted. The Perlites show good theoretical correlation because their average diameter, d_p, is so small compared to the fin spacing X, that the presence of the fins in this case is unnoticeable. For Perlite 500 this ratio is 0.06 whereas for Norton 1.5, it is 0.18. Consequently, the residence times between the finned and unfinned tubes remain similar. Figure 6.7 illustrates the effect of increased particle diameter on the average heat transfer coefficients at the given fin spacing of this investigation.

Although the model of heat transfer represented by Eq. (2.7) is difficult to apply to the finned tube case due to the uncertainty surrounding the particle residence times, another aspect of the theory discussed in Chapter 2 does hold well in this investigation.

TABLE 6.6 FINNED TUBE HEAT TRANSFER DATA

PARTICLE	U/U_{mf}	h_{void}	h_e	h_{rad}	h_w ($^{12}_{6}$)	h_{surf}	h_{theor}	h_{exp}	h_{exp}/h_{theor}
Norton 650	1.55	4.52	34.06	0.34	80.57	23.94	21.03	11.27	
					40.84	18.57	16.47		0.68
	2.20	4.72	39.34	0.30	80.53	26.43	23.17	13.49	
					40.80	20.03	17.73		0.76
*	2.60	4.85	39.34	0.30	80.53	26.43	23.19	14.18	
					40.80	20.03	17.75		0.80
*	2.98	4.96	39.34	0.30	80.53	26.43	23.20	15.13	
					40.80	20.03	17.76		0.85
Macro M40X	1.01	7.28	28.77	0.30	61.42	19.59	17.13	5.76	
					33.06	15.38	13.77		0.42
	1.07	7.35	31.51	0.30	61.42	20.83	18.13	6.83	
					33.06	16.13	14.38		0.47
	1.20	7.47	35.24	0.31	61.43	22.39	19.40	7.43	
					33.07	17.06	15.15		0.49
	1.30	7.56	35.24	0.30	61.42	22.39	19.42	9.00	
					33.06	17.06	15.17		0.59
Norton 1	1.47	6.13	32.54	0.29	54.13	20.32	17.49	8.11	
					28.33	15.14	13.35		0.61
	1.65	6.25	35.24	0.29	54.13	20.32	17.51	8.96	
					28.33	15.14	13.37		0.67
	1.83	6.36	32.54	0.29	54.13	20.32	17.53	10.46	
					28.33	15.14	13.39		0.78

TABLE 6.6 (Cont'd.)

PARTICLE	U/U_{mf}	h_{void}	h_e	h_{rad}	h_w ($^{12}_{6}$)	h_{surf}	h_{theor}	h_{exp}	h_{exp}/h_{theor}
Norton 1 (Cont'd.) *	2.13	6.55	37.57	0.29	54.13 28.33	22.18 16.15	19.05 14.23	12.30	0.86
Norton 1.5	1.15	6.69	30.85	0.30	37.81 20.60	16.99 12.35	14.93 11.22	5.76	0.51
	1.28	6.80	30.85	0.29	37.80 20.59	16.99 12.35	14.95 11.24	6.98	0.62
	1.47	6.95	30.85	0.29	37.80 20.59	16.99 12.35	14.98 11.27	8.75	0.78
*	1.64	7.09	30.85	0.29	37.80 20.59	16.99 12.35	15.01 11.30	10.05	0.89
Macro M27X	1.06	8.31	23.64	0.30	54.14 28.34	16.45 12.89	14.82 11.97	6.51	0.54
	1.09	8.35	23.64	0.30	54.14 28.34	16.45 12.89	14.83 11.98	7.17	0.60
	1.16	8.43	26.44	0.29	54.13 28.33	17.76 13.68	15.90 12.63	8.34	0.66
	1.20	8.48	26.44	0.29	54.13 28.33	17.76 13.68	15.91 12.64	8.49	0.67

TABLE 6.6 (Cont'd.)

PARTICLE	U/U_{mf}	h_{void}	h_e	h_{rad}	h_w (6^{12})	h_{surf}	h_{theor}	h_{exp}	h_{exp}/h_{theor}
Perlite 250	1.11	3.96	8.20	0.34	207.21	7.89	7.29	5.21	
					114.28	7.65	7.09		0.73
*	1.76	4.10	8.20	0.31	207.18	7.89	7.32	6.15	
					114.25	7.65	7.12		0.86
*	2.23	4.21	9.46	0.30	207.17	9.05	8.32	6.61	
					114.24	8.74	8.06		0.82
*	2.86	4.36	9.46	0.29	207.16	9.05	8.34	6.65	
					114.23	8.74	8.08		0.82
Perlite 500*	1.06	4.14	5.68	0.33	104.15	5.39	5.20	5.53	1.06
					52.55	5.13	4.98		
*	1.38	4.23	6.35	0.31	104.13	5.98	5.72	5.88	1.03
					52.53	5.67	5.45		
*	1.97	4.38	6.35	0.30	104.12	5.98	5.75	6.12	1.06
					52.52	5.67	5.48		
*	2.62	4.57	7.33	0.30	104.12	6.85	6.51	6.43	0.99
					52.52	6.43	6.16		

NOTES: 1) h units are Btu/hr-ft^2-°F

2) h_{exp}/h_{theor} based on $Nu_{COND} = 6$

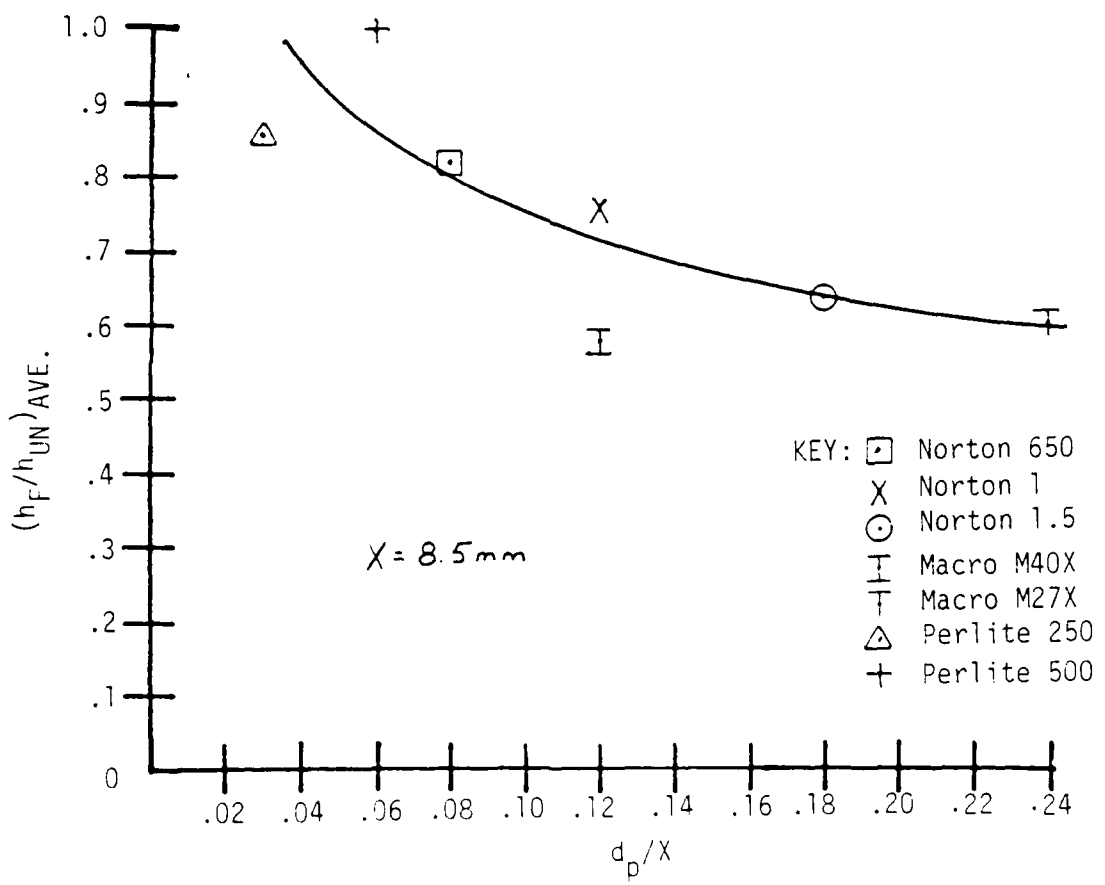

FIGURE 6.7 The Experimental Effect on Heat Transfer Coefficient Due to the Pressure of Fins

AD-A155 259 AN INVESTIGATION INTO THE FLUIDIZATION AND HEAT TRANSFER OF LOW DENSITY P.. (U) ARMY MILITARY PERSONNEL CENTER ALEXANDRIA VA J M MODLIN 10 MAY 85 2/2

UNCLASSIFIED F/G 10/1 NL

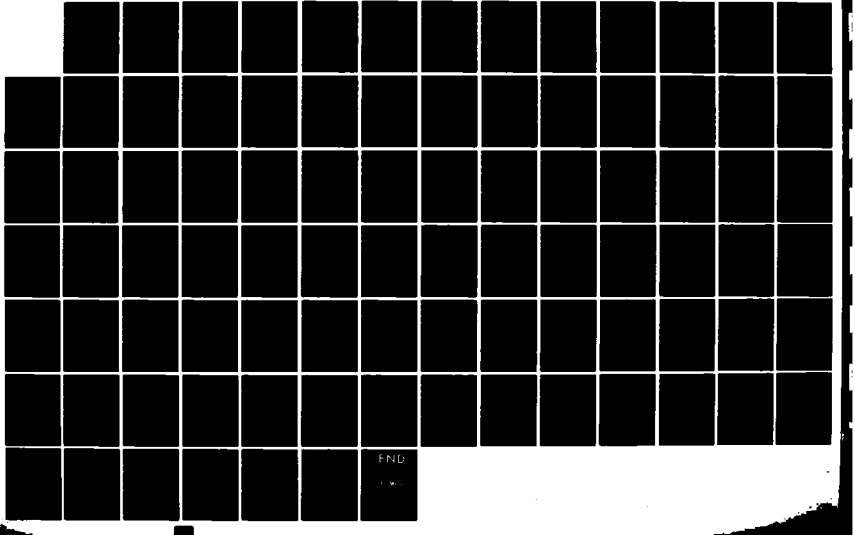

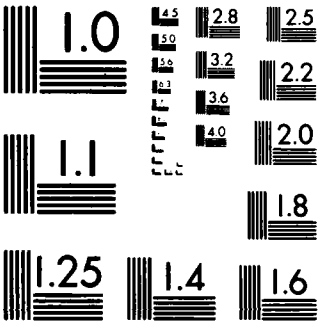

MICROCOPY RESOLUTION TEST CHART
NATIONAL BUREAU OF STANDARDS-1963-A

This concept, suggested by Glicksman, suggests reducing the unfinned tube heat transfer coefficient by 30-50% to estimate the finned tube coefficient. This "rule of thumb" works well for these test particles. Violations of this rule appear to occur only where the effect of the fins on fluidization is small. In general, the experimental data for these materials indicate that where theoretical correlation is not good this rule of thumb holds.

As would be expected, then, as particle diameter lengths approach that of the fin spacing of a finned surface, heat transfer coefficient values decrease in a fluidized bed. However, the intended purpose of using a finned surface over an unfinned one is to enhance the overall rate of heat transferred to a medium. For the particular materials and finned tube heater used in this investigation, this enhancement was significant. The degree of enhancement can best be illustrated by comparing the unfinned tube heat transfer coefficients to a psuedo-finned tube heat transfer coefficient defined as:

$$h' = \frac{Q_f}{A\ \Delta T_f} \tag{6.4}$$

where

Q_f = rate of heat transfer for the finned tube experiment [Btu/hr]

A = the tube surface area of the finned tube heater without fins [0.074 ft^2]

ΔT_f = the temperature difference between the bare surface of the finned tube heater and the fluidized material.

By comparing h_{UN} to h' gives an indication of the heat transfer enhancement due to the presence of fins is available. Table 6.7 shows this comparison. As is indicated in this table, heat transfer has been enhanced by a factor of 4 to 9 while the actual unfinned tube heat transfer coefficient has only been reduced by 1/3 - 1/2 for the larger particles and no more than by 1/5 for the smaller particles. These results suggest that an optimum particle diameter to fin spacing ratio and fin efficiency may exist in which the reduction of h_{UN} to h_{FIN} is minimized while maximizing the heat transfer enhancement.

In summary, then, the data available for the low density, large particles used in this investigation indicates that the heat transfer model represented by Eq. (2.7) does well in predicting finned immersed tube heat transfer coefficients only in situations where the ratio of particle diameter to fin spacing is very small. As this ratio exceeds about 0.08 particle fluidization between the fins is adversely affected, residence times increase, and heat transfer coefficients decrease. How the particle residence time is increased is difficult to quantify. Until it can be better evaluated the model cannot be accurately used. However, it has been noticed that in the cases where the model cannot be applied, the reduction of h_{UN} to h_{FIN} generally follows the "30/50 Rule of Thumb". Lastly, for all test particles the actual rate of heat transferred was significantly greater using fins than the reduction of the heat transfer coefficient.

6.2.2 The Effect of Particle Diameter and Density on Heat Transfer

The nature and variety of the test material used in this investigation makes it difficult to set forth specific conclusions on the effect changes in a particle's diameter and/or density would have on heat

TABLE 6.7 FIN ENHANCEMENT OF HEAT TRANSFER

PARTICLE	h_{un}	h'	h'/h_{un}
Norton 650	15.70	98.07	6.2
	16.78	117.42	7.0
	17.69	123.40	7.0
	18.37	131.67	7.2
Macro M40X	11.31	50.17	4.4
	12.08	59.46	4.9
	13.64	64.66	4.7
	13.90	78.31	5.6
Norton 1	12.90	70.54	5.5
	13.28	77.99	5.9
	13.55	91.00	6.7
	14.47	107.02	7.4
Norton 1.5	11.22	50.10	4.5
	12.50	60.75	4.9
	12.75	76.18	6.0
	13.86	87.50	6.3
Macro M27X	12.20	56.63	4.6
	13.03	62.38	4.8
	13.73	72.56	5.3
	13.37	73.92	5.5
Perlite 250	7.09	45.32	6.4
	7.09	53.55	7.6
	7.28	57.50	7.9
	7.69	57.85	7.5
Perlite 500	5.67	48.09	8.5
	5.86	51.16	8.7
	5.92	53.28	9.0
	6.12	56.00	9.2

NOTE: Units of h are Btu/hr-ft^2-°F

transfer coefficients. To do this would require the ability to vary a specific material's particle diameter while holding its density constant and vice versa. As was explained earlier, this is not possible with the materials on hand. Consequently, only a general view can be extracted from the results of this investigation. Figures 6.8 and 6.9 show the average trends exhibited by the test materials in a well fluidized bed on heat transfer with varying particle diameter and density. In general it can be seen that increased particle density, represented in h_e, appears to have a more significant effect on increased heat transfer than increased particle diameter, represented in h_w. That is, h_{exp} appears to change strongly with h_e, but only changes significantly with h_w when the ratio of $h_w/h_{exp} \simeq 1\text{-}2$.

This conclusion should not be surprising. As discussed in Chapter 2 and illustrated earlier in this chapter, particle diameter has its strongest effect on fluidization velocities. Heat transfer, on the other hand, is directly affected by the square-root of the particle density, as shown in Eq. (2.6). Thus, changes in density should have a greater impact on heat transfer than changes in particle diameter.

6.2.3 The Effect of Air Velocity on Heat Transfer

As illustrated in the data previously presented, the amount of air velocity through a fluidized bed is an important factor for heat transfer. In general, it would be expected that as the air velocity is increased, that is as U/U_{mf} increases, the heat transfer coefficient would also increase. However, for the materials used in this investigation there are various agreements and disagreements with this expectation. To evaluate this, a measure of the air velocity effect on changes in heat transfer coefficients is accomplished by determining the ratio of the

FIGURE 6.8 Nu_{exp} vs. $\frac{h_e}{h_{exp}}$ and $\frac{h_w}{h_{exp}}$ for Wall

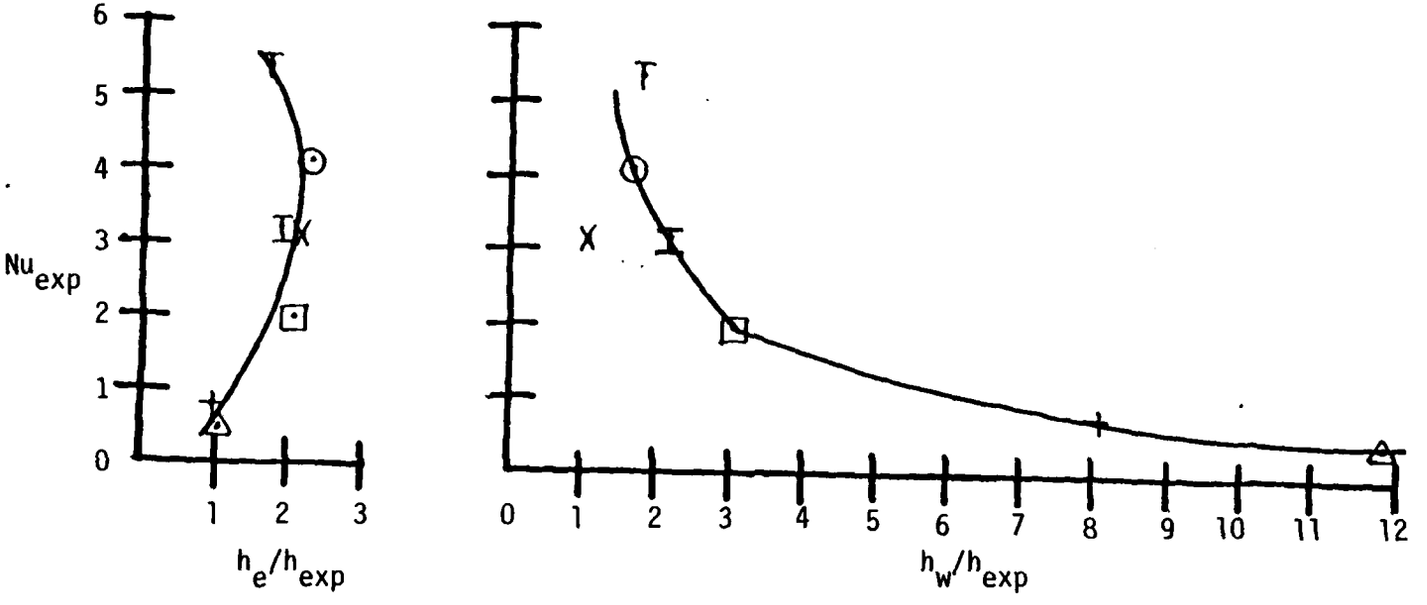

KEY:
- ⊡ Norton 650
- X Norton 1
- ⊙ Norton 1.5
- I Macro M40X
- T Macro M27X
- △ Perlite 250
- \+ Perlite 500

FIGURE 6.9 Nu_{exp} vs. $\frac{h_e}{h_{exp}}$ and $\frac{h_w}{h_{exp}}$ for Unfinned Tube

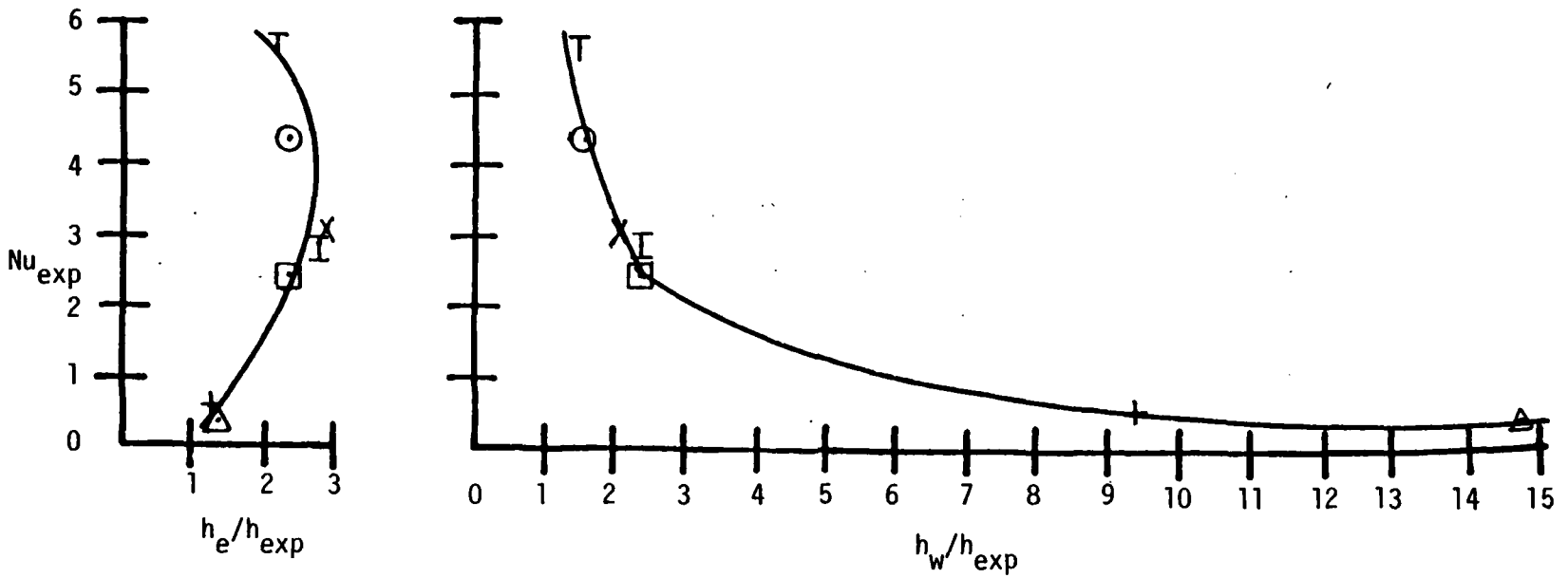

KEY:

- Norton 650
- Norton 1
- Norton 1.5
- Macro M40X
- Macro M27X
- Perlite 250
- Perlite 500

material's average heat transfer coefficient, h_{AVE}, to its maximum value, h_{MAX}, and comparing it to the material's average U/U_{mf} value. This nondimensional comparison gives the relative magnitude of the effect that changes in U/U_{mf} have on changes in the heat transfer coefficient. The results of this comparison for each test material and heating geometry is shown in Fig. 6.10.

Evaluating the data in this light yields several conclusions. First, without exception, all test materials exhibit a more significant change in wall heat transfer as U/U_{mf} changes than for the unfinned tube heat transfer. In the range of average U/U_{mf} values used in this work the average wall heat transfer coefficient varied from approximately 0.65 to 0.85 of the maximum value. In the unfinned tube case, however, the average heat transfer coefficient only varied from approximately 0.9 to 0.95 of h_{max}. These results indicate the increased sensitivity the wall heat transfer coefficient has with air velocity over the unfinned tube one. Thus it would appear that by increasing U/U_{mf} the wall heat transfer coefficient will, in general, increase more than the corresponding unfinned tube coefficient.

Secondly, finned tube heat transfer coefficients appear to exhibit behavior between that of the wall coefficients and the unfinned tube ones as U/U_{mf} changes. Additionally, in the two immersed tube cases, increases in U/U_{mf} appear to have a more dramatic effect on changes in h for materials of 1 mm and greater diameter than in the smaller materials.

Finally, the Perlite materials demonstrate, on average, less sensitivity of h to increases in U/U_{mf} for all heating geometries than do the other materials. This is especially evident in the immersed tube cases. Thus, to improve the heat transfer coefficients for Perlite requires significant increases in U/U_{mf}.

FIGURE 6.10 The Effect of Air Velocity on Heat Transfer Coefficient

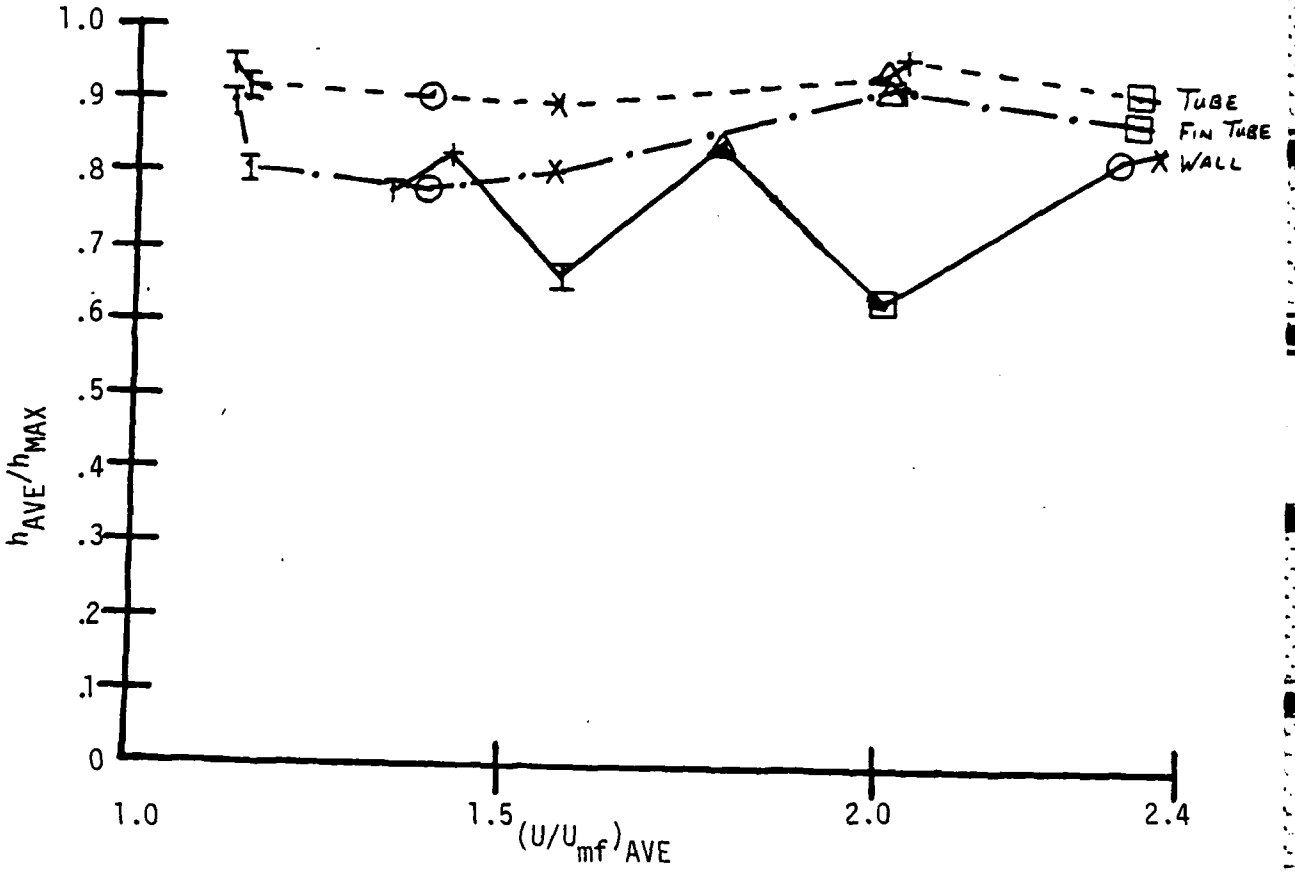

KEY:
- ⊡ Norton 650
- X Norton 1
- ⊙ Norton 1.5
- ⊥ Macro M40X
- ⊤ Macro M27X
- △ Perlite 250
- \+ Perlite 500

Increasing air velocity through a fluidized bed of these test materials to increase their heat transfer is not always appropriate, however, as indicated by the data. All of these materials, in both the unfinned and finned tube experiments, have shown a tendency of either approaching an asymptotic value for the heat transfer coefficient or reaching a peak value and then beginning to decline as U/U_{mf} was further increased (see Figs. 6.2 - 6.4).

Thus, the data for this investigation suggests several things. Increases in U/U_{mf} generally yield greater increases in wall heat transfer coefficients than immersed tube coefficients. Tube heat transfer coefficients of the larger diameter materials are more responsive to increases in U/U_{mf} than the smaller materials. The Perlite material is generally less affected by increased U/U_{mf} than the other materials, and all materials have demonstrated a peaking characteristic in the value of their immersed tube heat transfer coefficients.

6.2.4 The Effect of Bed Obstructions on Wall Heat Transfer

The previous topic discussed the effect increases in air velocity have on the heat transfer coefficients of the materials tested in this investigation. In general, it has been shown that increasing air velocity aids in increasing heat transfer. However, there is an apparent limit to this aid. Excessive air velocity will lead to increased bed voidage and/or particle elutriation, which adversely effects overall heat transfer, and will lead to significant air pumping power requirements. One method briefly investigated in this work of enhancing fluidized bed heat transfer without increasing air velocity is through the use of bed obstructions.

Obstructions should break up large bubble formations in a fluidized bed, thus increasing particle mixing and subsequently reducing

particle-to-surface residence times. To evaluate this effect, one 0.5 inch diameter x 15 inch wooden dowel was suspended horizontally in the center of the fluidized material in the two-dimensional bed used in this investigation. Comparison tests of with and without this obstruction was made using the Perlite 250 and Norton 1 materials. The criteria used for determining the effect of the presence of the obstruction was based solely on resultant wall heat transfer coefficient values. Sample results of this comparative testing are shown in Table 6.8. At low values of U/U_{mf} the presence of the obstruction had little or no effect on changing wall heat transfer coefficients. However, at higher values the heat transfer coefficents were improved by approximately 25-30%.

Having identified the value of using flow obstructions, it was necessary to determine a possible optimum number and positioning of the obstructions to yield the greatest increase in wall heat transfer. This was done using the Perlite 500 and Norton 650 materials. Various geometries of obstruction placement were tested. These geometries and the test results are listed in Table 6.9. As a result of these test it was concluded that obstructions placed centrally to the heated surface and in the middle of the bed performed better than those placed either below or above the heated surface or closer to either wall. For the 6 inch high wall heater used in this work it was further found that two parallel dowels, one up two inches from the heater bottom and the other down two inches from the top, resulted in higher heat transfer coefficients than any other dowel combination.

The tentative conclusions that can be drawn from this are that obstructions of air flow through a fluidized bed appear to improve wall heat transfer at moderate to high values of U/U_{mf} . Obstructions need to

TABLE 6.8 OBSTRUCTION TESTING RESULTS

MATERIAL	U/U_{mf}	$h_{w/o}$	h_{with}	%Δ
Perlite 250	1.06	6.35	6.08	-4.25
	1.94	6.69	8.72	30.34
Norton 1	1.81	7.13	9.06	27.07

NOTE: Units of h are Btu/hr-ft^2-°F

TABLE 6.9 OBSTRUCTION GEOMETRY TEST RESULTS

MATERIAL	GEOMETRY	U/U_{mf}	h(Btu/hr-ft^2-°F)
Perlite 500	1 each dowel, on plexiglas bed wall, 1 inch up from air distributor	2.0	8.2
	1 each dowel, on plexiglas bed wall, bottom of heater unit	2.0	7.9
	1 each dowel, center of bed, center of heater unit	2.0	8.3
Norton 650	1 each dowel, center of bed, center of heater unit	2.1	10.0
	2 each dowels, center of bed, center of heater unit 4 inches apart	2.1	10.2
	3 each dowels, center of bed, center of heater unit 1 inch apart	2.1	9.5
	4 each dowels, center of bed, center of heater unit 1 inch apart	2.1	9.5

be symmetrically located near the heated surface. The number and perhaps geometry of the obstructions need to be optimized. Too few obstructions does not yield the desired result while too many apparently interfer with the fluidization process. For these reasons all the data ultimately taken in this investigation and reported in this chapter for the wall heat transfer was taken using the two 0.5 inch dowels described above.

6.2.5 Heat Transfer and Air Pumping Power Requirements

A detailed discussion of air pumping power requirements for the fluidization of the materials at the conditions of this work was conducted earlier in the chapter. This section will compare these required pumping power values to the available heat transfer in the same manner as is done for other forms of heat exchanging surfaces.

In order to effectively make this comparison, air pumping power requirements must be expressed in terms of power per unit wall surface area to overcome friction and not in terms of power per unit bed cross-sectional area. For the two-dimensional bed used in this investigation, the ratio of the cross-sectional area to the surface area is 0.13. Figures 6.11 and 6.12 graphically depict the relationships between each material's friction power requirement per unit wall surface area, $(\underline{P}/A)$, and the corresponding wall heat transfer coefficient, h_w based upon the overall bed pressure drop with the 2 bed obstructions described above . This result, modified appropriately, will be utilized in Chapter 7 for making comparisons with other heat transfer surfaces.

6.3 Summary of Experimental Results

As a result of this experimental investigation, several results and conclusions have been developed. All of the low density test materials used in the investigation have demonstrated the capability of being

FIGURE 6.11 A Comparison of the Heat Transfer and Friction Power Characteristics of the Norton and Macro Materials

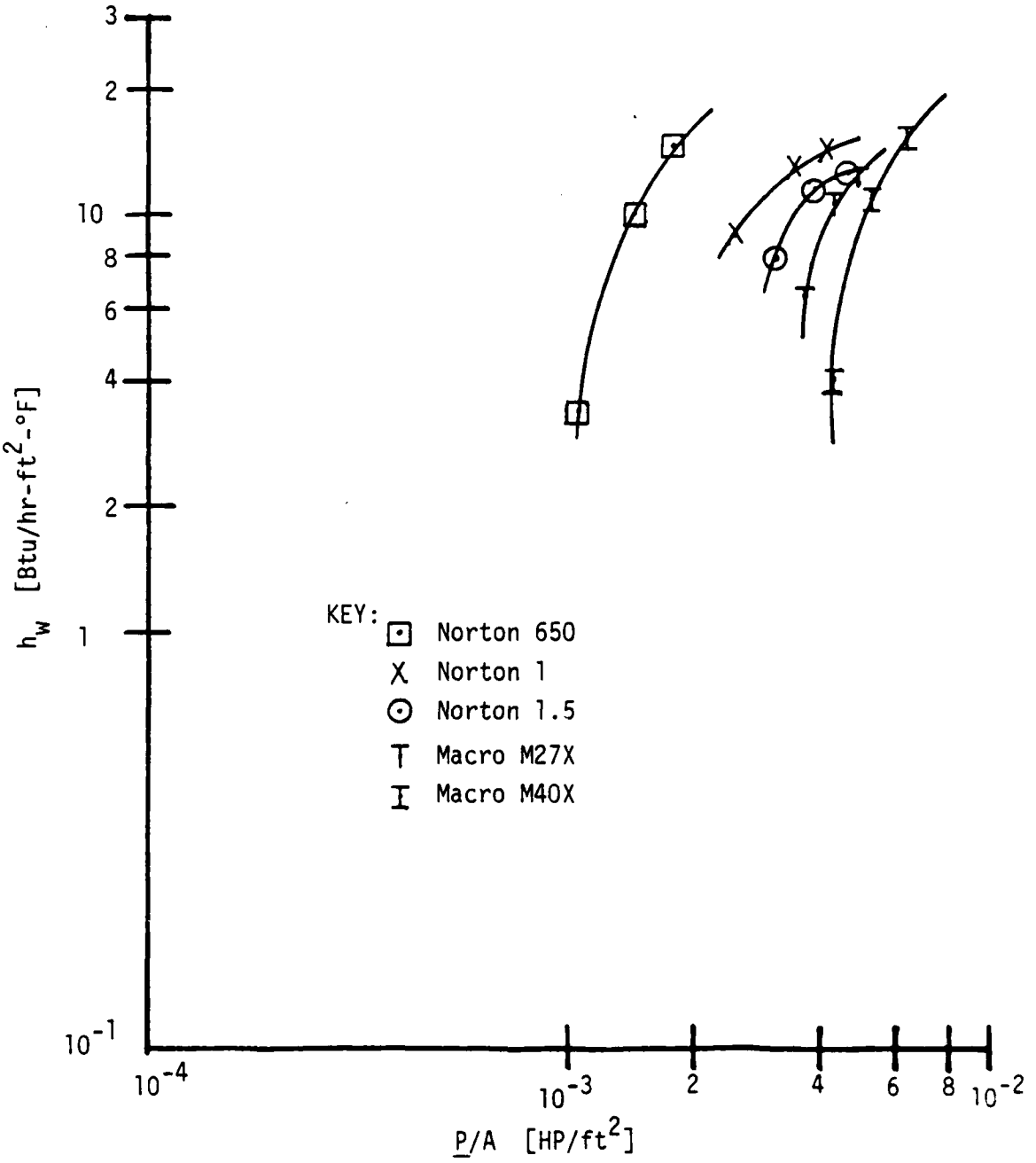

Figure 6.12 A Comparison of the Heat Transfer and Friction Power Characteristics of the Perlite Materials

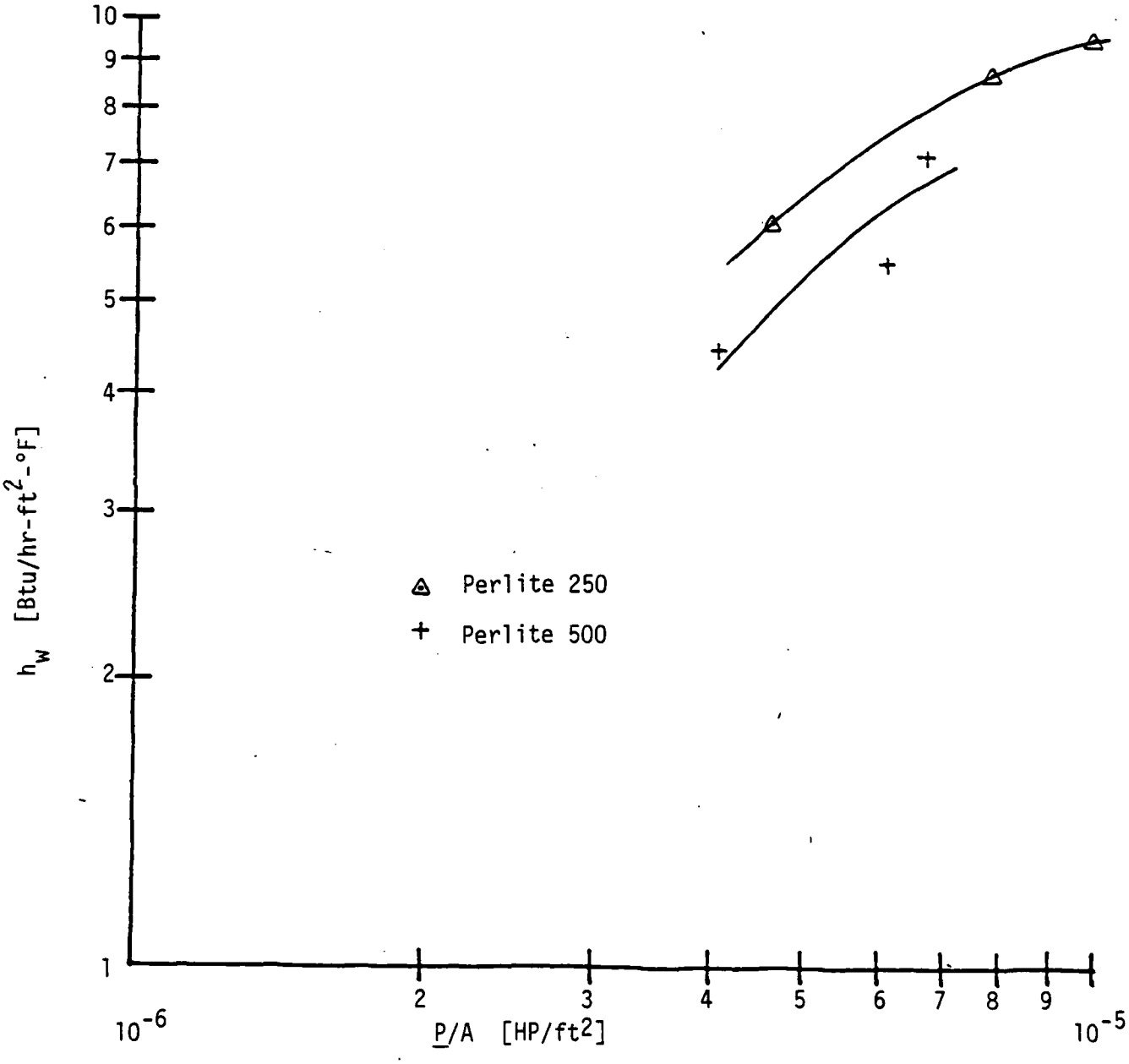

fluidized successfully. The Geldart materials classification based on fluidization characteristics generally does well in predicting the test materials fluidization behavior, except for the lowest density materials where electrostatic effects are important. The data indicates that particle diameter is the controlling factor in a materials minimum fluidization velocity and, ultimately, external air pumping power requirements. Density, on the other hand, controls the fluidized bed pressure drop.

Furthermore, the model of heat transfer depicted by Eq. (2.7) does reasonably well in predicting the overall heat transfer coefficient from a heated surface to the fluidized particles. At low values of $(U_0 - U_{mf})$, however, the data indicates that other mechanisms may be taking place than those represented by the model. Also, the model cannot be confidently applied to a finned surface due to the uncertainty of the effect the presence of the fins has on the material's fluidization. In this case, reducing the unfinned heat transfer coefficient by 30-50% for these materials works reasonably well in predicting their finned heat transfer coefficients assuming the fin spacing is not too small.

Data on the various heating geometries indicates that, in general, at a given fluidization velocity the immersed tube heat transfer coefficient is larger than the corresponding one from the fluidized bed wall. However, increasing air velocity and using flow obstructions tends to increase the wall heat transfer coefficients at a greater rate than the immersed tube ones. The controlling component of these overall heat transfer coefficients is the emulsion component, h_e. Particle density is shown to have a significantly larger effect on heat transfer than particle diameter. Increased air velocity through the bed increases heat transfer, but

indications are that there is an upper limit to this before increased voidage and particle elutriation effects cause a decrease in heat transfer.

Finally, and of special importance to the intended applications of this work, the low density test materials showed fairly good ratios of energy delivered to external operating energy required. Chapter 7 will discuss this and other aspects of utilizing these experimental results and conclusions for specific engineering applications.

CHAPTER 7

SELECTED ENGINEERING APPLICATIONS

This chapter will apply the results and identified trends of low density particle fluidization, as discussed in Chapter 6, to two specific engineering concepts: the use of a two-dimensional fluidized bed as an active flat plate solar collector and the use of a fluidized bed as a heat exchanger. Of primary concern in these applications, and which will serve as the basis of this discussion, is the thermal performance and associated costs in energy usage of the fluidized bed as compared with conventional equipment. The primary application of this work, a solar collector, will be presented first.

7.1 The Fluidized Bed Solar Collector

The concept of a fluidized bed of lightweight particles used within the cavity of a building's south facing wall as a vertical flat plate solar collector, as discussed in Chapter 1, could not be evaluated until data on the fluidization and heat transfer characteristics of the lightweight particles was obtained. As a result of the experimental work of this investigation an initial evaluation of this concept can now be conducted. From the results of this evaluation further and more definative conclusions can be drawn on the relative merit of the fluidized bed solar collector concept. In this section, data drawn from the experimental work on the fluidization and heat transfer of the low density test materials will be utilized to compare the predicted performance and feasibility of a "typical" Fluidized Bed Solar Collector to that of conventional liquid and air-cooled solar collectors. To accomplish this a brief description of the

general characteristics and design of conventional flat plate solar collectors is first given. Secondly, an analysis of a fluidized bed as a solar collector is performed. With this information, comparisons are then made between a representative fluidized bed solar collector, using the test materials of this work, and comparable conventional collectors.

7.1.1 General Characteristics and Design of Conventional Flat-Plate Solar Collectors

Flat-plate solar collectors in present use require either a liquid or air as the heat transfer medium. A typical commercial liquid-cooled collector panel has an area of 18 to 32 ft^2, a copper absorber plate with copper tubes manifolded into headers, a black chrome selective absorber surface, fiberglass or foam insulation, and tempered glass covers. Air-cooled collectors differ from the liquid-cooled ones mainly in the design of the fluid passage mechanism. A continuous black sheet of steel or aluminum replaces the plate and tubes. A lower metal sheet forms the bottom of the air passage. Inlet and outlet ports are provided at the sides or bottom of the unit, and metal screens are optionally used as absorbers [28].

The thermal performance of any type of solar collector can be evaluated by an energy balance which determines the amount of incoming solar energy, I_c, transferred to the working fluid in the form of useful energy, q_u. For a flat-plate collector of area A_c this energy balance is

$$I_c A_c \overline{\tau_s \alpha_s} = q_u + q_{loss} + \frac{de_c}{dt} \qquad (7.1)$$

where de_c/dt represents the rate of internal energy storage in the collector plate and is negligible for thin, metallic plates.

For convenience in terms of physical parameters and to allow direct comparison between the thermal performance of collectors of varying designs Eq. (7.1) may be represented in the alternate form

$$q_u = A_c F' \{\overline{\alpha\tau}\, I_c - U_c(T_f - T_a)\} \tag{7.2}$$

where F' denotes the collector efficiency factor and physically represents the ratio of two overall heat transfer coefficients [29]. The numerator is the thermal resistance between the collector surface and the ambient air. The denominator is the thermal resistance between the working fluid and its environment. It has a strong dependence on the overall collector heat loss conductance, U_c, and the average heat transfer coefficient of the working fluid. It is only slightly dependent on temperature. The collector efficiency factor also increases with increasing plate thickness and plate thermal conductivity. Other new terms in Eq. (7.2) represent the temperature of the working fluid and ambient air, T_f and T_a. Additionally, the overall heat loss conductance, U_c, is primarily a function of the number and type of covers used, the radiant emissivity of the collector surface, the effectiveness of the back insulation, and the environmental wind speed. Equation (7.2) is limited, however, for it only yields the rate of heat transfer to the working fluid at a given point along the collector plate.

In an actual collector the fluid temperature increases in the direction of flow as heat is transferred to it. Thus, to compare the performance of a real collector to the thermodynamic optimum, it has been

convenient to define a heat-removal factor, F_R , as the ratio of the actual rate of heat transfer to the working fluid to the rate of heat transfer at the minimum temperature difference between the collector plate and the environment [30]. This thermodynamic optimum corresponds to the condition of the working fluid remaining at the inlet temperature throughout the collector, a condition which can be approached at high working fluid Reynold's numbers. As a result, F_R approaches F' , as an upper limit, with increasing fluid flow rate. Thus, the rate of useful heat transfer, q_u , can then be expressed as

$$q_u = A_c F_R \{ \overline{\alpha\tau}\, I_c - U_c(T_f - T_a)\} \tag{7.3}$$

where T_f is now the working fluid inlet temperature. This form of the energy balance is frequently used for design because the fluid inlet temperature to the collector is usually known or can be specified.

Lastly, the collector efficiency η , is defined as the ratio of the useful energy delivered to the total incoming solar energy, or, upon using Eq. (7.3), as

$$\eta \equiv \frac{q_u}{A_c I_c} = F_R\{ \overline{\alpha\tau} - U_c \frac{(T_f - T_a)}{I_c} \} \tag{7.4}$$

For a given design of a flat-plate solar collector F_R , $\overline{\alpha\tau}$, and U_c are relatively constant. Values of these parameters may be determined experimentally and have been estimated in the literature [29,30]. Consequently, as indicated by Eq. (7.4) a straight line relationship exists between η and the variable (due to environmental conditions) $\frac{(T_f - T_a)}{I_c}$.

7.1.2 The Fluidized Bed Solar Collector

A fluidized bed solar collector could be designed similar to that of an air-cooled flat-plate collector. The difference being that the air would be used to fluidize particles in a south facing wall cavity of a building, two to four inches wide, between an external solar absorber surface and an interior insulated wall. The wall cavity would be filled with lightweight particles on the order of those used in this investigation. The air would flow from a distributor at the base of the cavity, around the particles and embedded heat transfer tube(s), and be collected in a header at the top of the cavity. Solar insolation is transmitted through the front cover and absorbed by the collector surface. The fluidized particles, in turn, transfer the absorbed energy from the back of the collector surface to the embedded heat transfer tube(s). A view of a fluidized bed solar collector is shown in Figure 7.1.

As with the more conventional liquid-cooled flat plate solar collectors, useful energy can be removed from the fluidized bed solar collector through a water stream in the immersed heat transfer tube(s). Additional energy could be collected using the fluidizing air as a solar energy collector medium similar to an air-cooled collector scheme in a building space heating design. This is limited, however, due to the low air velocities required for fluidizing the small, lightweight particles. If not used for space heating purposes, the heated air could be recirculated back through the base of the cavity and provide additional energy to the immersed tubes.

In order to analyze the thermal performance of a fluidized bed solar collector Eq. (7.3) must be further examined. The terms A_c , $\overline{\alpha\tau}\, I_c$,

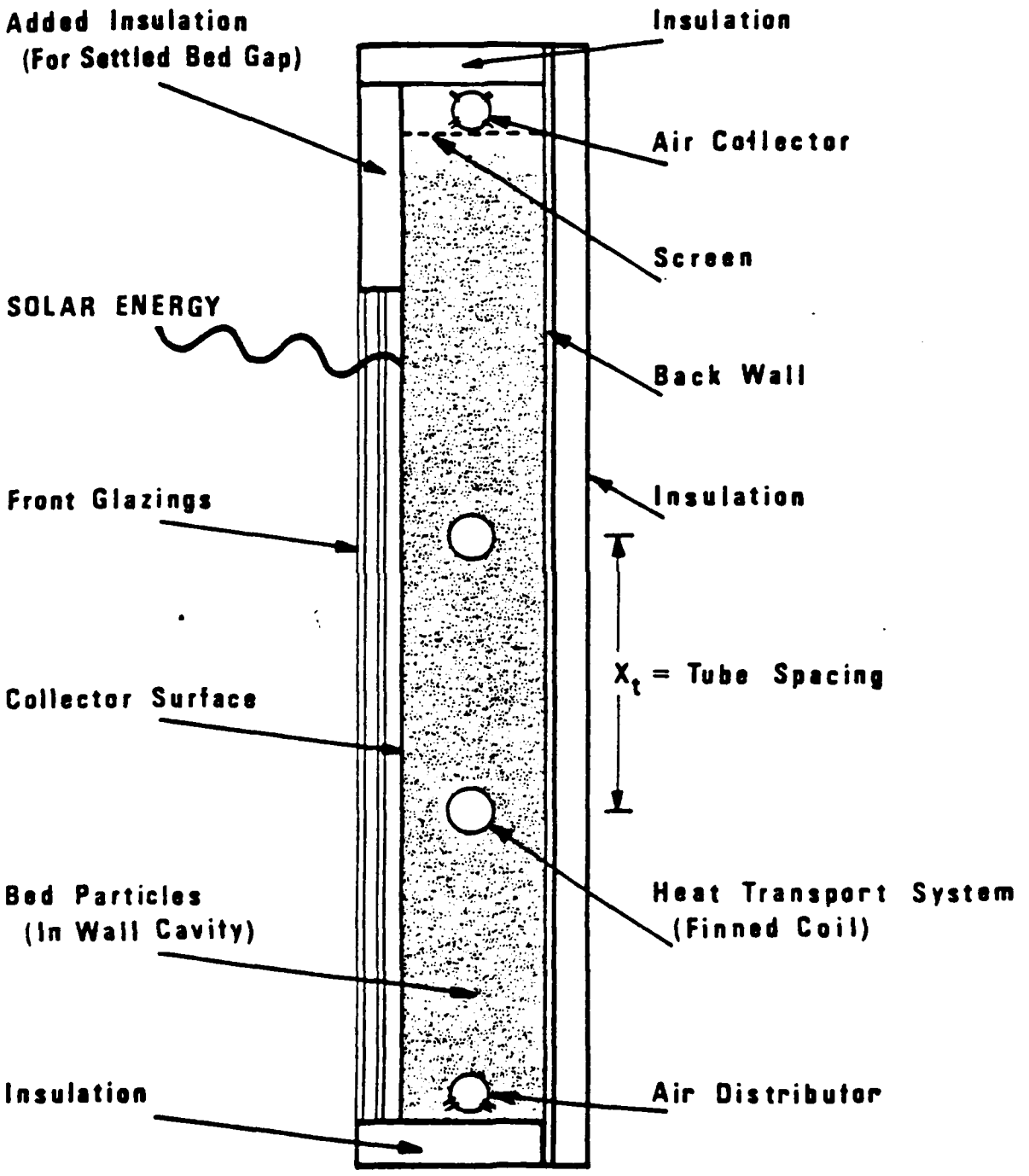

FIGURE 7.1 Fluidized Bed Solar Collector

and $U_c(T_f - T_a)$ are design parameters or are determined from design parameters and environmental operating conditions in the same procedure as used with a conventional flat-plate collector. The evaluation of the collector efficiency factor, F_R, distinguishes the performance of a fluidized bed solar collector from that of a conventional collector. As before, F_R represents the ratio of the actual rate of heat transfer to the working fluid to the rate of heat transfer at the minimum temperature difference between the collector plate and its environment. For a fluidized bed, expressed in terms of the appropriate resistances to heat transfer, this is given by

$$F_R = \frac{\frac{1}{U_c}}{\frac{1}{U_c} + \sum R_{bed}} = \frac{1}{1 + U_c(R_w + R_B + R_T)} \qquad (7.5)$$

where R_w = the thermal resistance between the collector surface and the fluidized particles

R_B = the thermal resistance within the fluidized bed

R_T = the thermal resistance between the bed particles and the working fluid in the immersed tubes.

For absorbing surfaces made of thin metal sheets,

$$R_w = \frac{1}{h_w} \qquad (7.6)$$

where h_w is the heat transfer coefficient between the back surface of the

collector surface and the bed particles. In this work it is equal to h_{wall}. The effective thermal resistance within a fluidized bed is

$$R_B = \frac{\ell A_c}{k_{eff} A_x} \tag{7.7}$$

where ℓ is the average path length for heat flow from the collector surface to the immersed heat transfer tube(s) and k_{eff} is the effective thermal conductivity of the bed. The average path length, ℓ, is a function of the bed design and can be approximated by

$$\ell = \frac{x_t}{4} \tag{7.8}$$

The effective thermal conductivity, k_{eff}, is a quantity whose value can only be estimated at this time. Work is presently being conducted to accurately determine k_{eff} for a bed of small, lightweight particles [17]. Previous work on beds of greater density material has indicated that k_{eff} is a function of the amount of material displaced within the bed due to bubble motion, the effective density and heat capacity of the particles, and the height in which particles are displaced within the bed [31]

$$k_{eff} = \alpha(1 - \varepsilon_{mf})(\rho c)_s (U_0 - U_{mf})x_t \tag{7.9}$$

For heat transfer tubes made of thin metal, the resistance to heat flow is

$$R_T = \frac{A_c}{h_u A_u} + \frac{A_c}{h_i A_i} \tag{7.10a}$$

$$R_T = \frac{A_c}{\varepsilon h A_{tot}} + \frac{A_c}{h_i A_i} \qquad (7.10b)$$

where Eq. (7.10a) is the resistance associated with an unfinned tube and Eq. (7.10b) is the corresponding resistance of a finned tube. The term ε in Eq. (7.10b) represents the overall surface efficiency as defined in Chapter 4.

Thus, as with conventional flat-plate solar collectors, a fluidized bed collector efficiency can be represented by Eq. (7.4). A straight line relation would again exist between η and $(T_f - T_a)/I_c$ for the fluidized bed collector.

7.1.3 Solar Collector Comparisons

Using the relationships developed in the previous two sections, the efficiency of a fluidized bed solar collector can be compared to that of a typical liquid and air-cooled flat plate solar collector operating under the same environmental and geometric conditions. In this section, a standard liquid and air-cooled flat-plate solar collector will be compared with fluidized bed solar collectors comprised of this work's low density test material. All collectors will bed designed to the following specifications:

1. Collector Surface Area, A_c = 8 ft x 4 ft = 32 ft^2
2. Air-cooled and fluidized bed collector cross-sectional area, A_x = 4 ft x 4 in = 1.33 ft^2
3. Black painted, copper collector plate, ε = 0.95
4. Environmental Wind Speed of 8 mph

5. Ambient air temperature of 50°F
6. No back heat losses
7. Vertically oriented.

All collectors will be evaluated using one and two glass covers. From these specifications the following additional data may be obtained [29]:

One Glass Cover		Two Glass Covers	
U_c	= 1.2 Btu/hr-ft^2- F	U_c	= 0.70 Btu/hr-ft^2- F
τ_s	= 0.91	τ_s	= 0.83
$\alpha = \varepsilon =$	0.95		
$\overline{\alpha\tau}$	= 0.862	$\overline{\alpha\tau}$	= 0.786

Given these design parameters common to all three collector types, the individual collectors may now be designed and evaluated. Table 7.1 lists the additional details of the liquid-cooled flat-plate collector used for the comparison.

An air-cooled solar collector can also be designed and evaluated using standard techniques and the specifications listed above. Malik and Buelow [32] have surveyed the fluid mechanics and heat transfer phenomena in air collectors and have concluded that the heat transfer in a smooth air-cooled collector can be expressed as

$$St = \frac{0.0192\ Re^{-1/4}}{1 + 1.22\ Re^{-1/8}\ (Pr-2)} \qquad (7.11)$$

where $St \equiv Re\ Pr\ Nu$, the convective heat transfer coefficient in the Nusselt Number is based on the unit collector area, and the Reynolds and

TABLE 7.1 LIQUID-COOLED FLAT PLATE SOLAR COLLECTOR DATA

Components	:	Copper tubes of 0.4 in ID, connected by a .02 in thick plate at a center-to-center distance of 6 in., 7 tubes total
	:	Working fluid - Water
	:	Working fluid flow rate - 1.54 lb/sec
One Glass Cover	:	$F_R = 0.93$
	:	$\eta_{LC1} = 0.93\{.862 - 1.2(T_f - T_a)/I_c\}$
Two Glass Covers	:	$F_R = 0.98$
	:	$\eta_{LC2} = 0.98\{.786 - 0.7(T_f - T_a)/I_c\}$

Nusselt Numbers are based on the unit hydraulic diameter. Using Eq. (7.11) to determine the convective heat transfer coefficient of the air-cooled collector and the relations developed in Section 7.1.1, the design and performance of the collector can be completed and evaluated. Table 7.2 lists the additional details for the air-cooled flat-plate collector used in the comparison.

The fluidized bed solar collector used in the comparison will, in addition to meeting the general design specifications, consist of two 4 ft. long, 0.75 in. ID, finned immersed heat exchange tubes symmetrically spaced 2.67 ft apart within the bed. The finned tubes used in this collector are of the same geometry as that used in the experimental section of this work. Bed resistances are determined for each test material based upon the experimental results discussed in Chapter 6 and on Eqs. (7.6), (7.7) and (7.10b). Table 7.3 lists the data of each test material, and an "optimum" material to be discussed separately, for use in the fluidized bed solar collector comparison.

As can be seen from this data, for this particular design of a fluidized bed solar collector, the tube resistance is the controlling heat transfer resistance when compared to the wall resistance. This could be changed, however, by possibly changing the geometry of the immersed finned tubes or by adding more tubes. Using the model for the bed resistance R_B expressed by Eq. (7.7) results in this resistance being small compared with the other heat transfer resistances for the Norton and Macro materials, but very large for the Perlites. This is due to the Perlites low density and fluidization velocity.

TABLE 7.2 AIR-COOLED FLAT PLATE SOLAR COLLECTOR DATA

Components	:	Air Flow Rate = 0.8 lbm/sec
	:	Re_H = 29760
	:	h = 1.35 Btu/hr-ft^2 - F
	:	Galvanized Steel Air Ducting, 12" x 12": Entrance - 3 ft. straight section, 90 rectangular section elbow, 1 ft straight section emptying into a 2" x 48" plenum at the base of the air collector. Exit - Symmetric with the entrace.
One Glass Cover	:	F_R = 0.52
	:	$\eta_{AC1} = 0.52\{.862 - 1.2(T_f - T_a)/I_c\}$
Two Glass Covers	:	F_R = 0.65
	:	$\eta_{AC2} = 0.65\{.786 - 0.7(T_f - T_a)/I_c\}$

TABLE 7.3 FLUIDIZED BED SOLAR COLLECTOR DATA

MATERIAL	U_0 [fps]	R_W	R_B	R_T	$F_{R\ 1\ cover}$	$F_{R\ 2\ covers}$
Norton 650	0.6	.067	.010	.151	0.78	0.86
Norton 1	1.2	.083	.008	.177	0.76	0.84
Norton 1.5	1.5	.100	.007	.193	0.74	0.83
Macro M40X	1.6	.091	.007	.212	0.73	0.82
Macro M27X	2.0	.091	.018	.236	0.71	0.81
Perlite 250	.025	.105	1.75	.321	0.28	0.40
Perlite 500	.030	.139	2.91	.353	0.20	0.30
"Optimum"	0.14	.091	.157	.265	0.53	0.74

NOTE: Units for all resistances are [hr-ft^2- F/Btu].

An indication of the comparable performances of the three types of flat-plate solar collectors can be accomplished by graphically depicting collector efficiency, η, as a function of $(T_f - T_a)/I_c$. Using the data contained in Tables 7.1 through 7.3 and by applying Eq. (7.4), this graphical comparison is shown in Figures 7.2 and 7.3. As illustrated in these figures, the thermal performance of a fluidized bed solar collector can be expected to fall between that of a comparable conventional liquid and air-cooled collector. The exception to this is in the case of very low density fluidized material, such as the test Perlites. Their performance is poor due to their large bed resistance to heat transfer. This result indicates a need to take steps to reduce this resistance or, due to its inherent uncertainty, determine a more accurate measure of its value to allow for the viable use of these particular low density materials in this application.

A third option is to use another low density material, unavailable for this investigation, that is of slightly greater density but of approximately the same size as the Perlite material. As described in Chapter 4, Perlite's density and particle diameter can be independently controlled and, thus, may be a possible candidate for this use.

The criteria that can be used to determine the characteristics of this "optimum" material is a direct result of the analysis of Chapter 6. As stated there, heat transfer showed a general trend of increasing as density and velocity increased. Fluidization velocity increased with particle diameter. With these two trends, the "optimum" material should be denser than the present Perlite material and at least as large as the Perlite 500 to yield greater heat transfer. The air pumping power required for

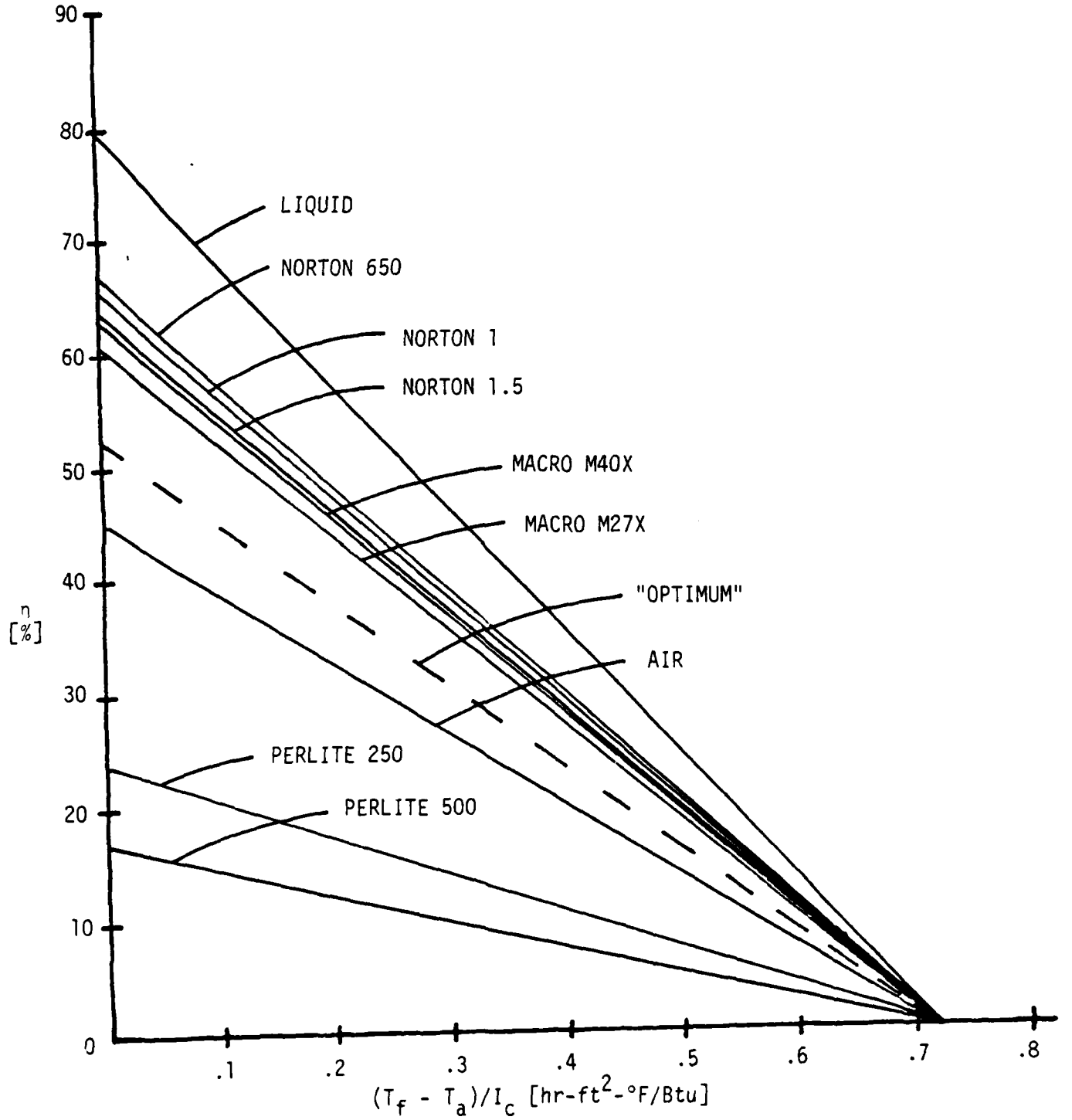

FIGURE 7.2 Solar Collector Comparisons (One Cover Glass)

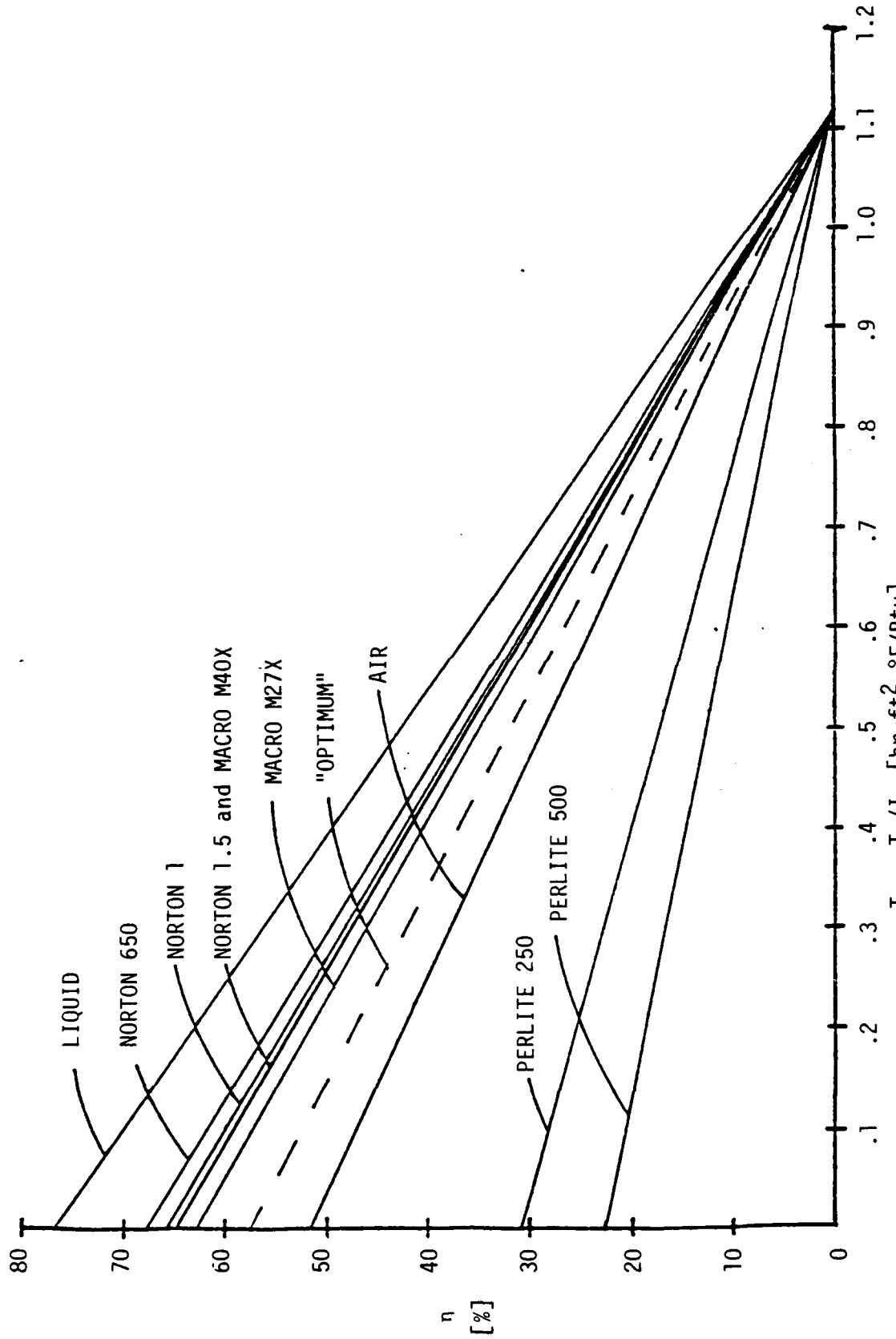

FIGURE 7.3 Solar Collector Comparisons (Two Cover Glasses)

fluidization was also strongly effected by material density and the required fluidization velocity. Thus, the "optimum" material should also be less dense and have a smaller particle diameter than the Norton and Macro materials. The resulting suggested characteristics of this "optimum" material is a material having a density of approximately 10 pcf and a particle diameter approximately equal to that of the Perlite 500 of 0.02 in.

This material, perhaps Perlite-like but slightly denser, should have the following fluidization and heat transfer characteristics based upon the results of this work and Eqs. (2.2), (2.3), and (2.7), which have been shown to predict these characteristics well:

$$U_{mf} \cong 4\ U_{mf} \text{ of Perlite 500 (due to density increase)} \cong 0.07 \text{ fps}$$

$$\Delta P_B \cong 4\,\Delta P_B \text{ of Perlite 500 (due to density)} \cong 4 \text{ psf/ft of bed height}$$

$$h_w \cong 11 \text{ Btu/hr-ft}^2\text{-°F at } U_0 = 0.14 \text{ fps } (U/U_{mf} = 2)$$

$$h_F \cong 8 \text{ Btu/hr-ft}^2\text{-°F at } U_0 = 0.14 \text{ fps .}$$

Using this data in the same manner as with the test material, the fluidized bed solar collector data (Table 7.3) and predicted efficiency data (Figures 7.2 and 7.3) is obtained.

As indicated in Table 7.3 the increased density and fluidization velocity of the ideal material has significantly lowered the bed resistance, R_B, as compared with the Perlite 500 (the material with equal particle diameter). R_w and R_T have remained on the same order as with the test materials. Consequently, the significant decrease of R_B is

solely responsible for the "optimum" materials drastics improvement in performance ove. ıe test Perlite's. The additional importance of the identification of this "optimum" material will be presented later in this section.

To this point in the discussion only thermal performance comparisons of the fluidized bed collector to a liquid and air-cooled collector have been considered. This is of primary importance in order to tentatively determine the feasibility of the fluidized bed solar collector concept. Having now indicated that thermally the fluidized bed solar collector has the potential of falling in the same operational range as conventional flat-plate liquid and air-cooled collectors, other operational comparisons need to be conducted.

One of these, the external power requirements, is listed in Table 7.4 for each solar collector based upon the collector surface area. It is informative to note that the fluidized bed solar collector requires less water pumping power than the liquid-cooled collector for the same water heat transfer coefficient inside the tubes (~1000 Btu/hr-ft^2-°F). Also, the power required to pump the water through a fluidized bed collector is significantly less than that required to fluidize the bed,except for Perlite. All materials require less air pumping power than the corresponding air-cooled collector in this design. Additionally, the air-cooled collector in this design, a 8 ft x 4 ft x 4 in collector with a 1 ft^2 air exit duct three feet long, is only well suited for a building space heating scheme in which the heated air is just circulated to an open space directly adjacent to the collector. The other two collector types deliver their usable heat in a more versatile form, through a heated water

TABLE 7.4 SOLAR COLLECTOR EXTERNAL POWER REQUIREMENTS [HP/ft^2]

COLLECTOR TYPE	AIR	WATER
Liquid-cooled		2.0×10^{-3}
Air-cooled	10×10^{-3}	
Fluidized bed:		
Norton 650	4.6×10^{-3}	1.4×10^{-3}
Norton 1	7.4×10^{-3}	"
Norton 1.5	8.2×10^{-3}	"
Macro M40X	13.0×10^{-3}	"
Macro M27X	9.8×10^{-3}	"
Perlite 250	2.3×10^{-5}	"
Perlite 500	1.8×10^{-5}	"
"Optimum"	3.3×10^{-4}	"

stream. If the air-cooled collector were designed to deliver heat to the building interior, its air pressure losses would be even larger due to the more extensive ducting required.

A second operational consideration involving the fluidized bed solar collector is its actual use in a building wall cavity. Generally, vertical walls are designed to resist a laterial wind pressure load, acting either inward or outward, of about 20 psf for a wall less than 50 feet high, plus any additional loading the designer may expect the wall to encounter [33]. If a building wall cavity is to serve as a fluidized bed the additional lateral load placed on the wall due to the bed pressure drop must be considered in the wall design. Chapter 6 presented the results of the bed pressure drops associated with the test materials. Table 7.5 lists these results based upon an 8 foot high wall/fluidized bed solar collector. As shown in this table the additional wall loading associated with the operation of a fluidized bed is significant for the Norton and Macro materials. Use of these materials would, therefore, require a careful wall design. The Perlite materials, on the other hand, yield little, if any, additional wall loading over what is generally designed to accommodate wind effects. Thus, the additional wall loading due to the bed pressure drops may, in itself, be either an economic or construction limitation on the ultimate choice of material to use in a fluidized bed solar collector. For this reason the importance of identifying the previously discussed "optimum" type material becomes evident. In a realistic context, the very large pressure drops associated with the Norton and Macro materials, despite their good thermal efficiencies, could eliminate them for use in this application. Additionally, the test Perlite materials are poor

TABLE 7.5 FLUIDIZED BED SOLAR COLLECTOR WALL PRESSURE DROPS

MATERIAL	PRESSURE DROP [psf]
Norton 650	101.7
Norton 1	84.9
Norton 1.5	75.5
Macro M40X	109.8
Macro M27X	67.4
Perlite 250	12.8
Perlite 500	8.1
"Optimum"	32.0

NOTE: The maximum pressure occurs at the base of the wall and decreases linearly to zero at the top of the wall.

thermal performers. The "optimum" material provides a compromise, good thermal and wall load results.

Several other considerations are also involved in the comparison of a fluidized bed solar collector to conventional ones. The fluidized bed solar collector cannot be tilted at large angles for the vertical as can liquid-cooled collectors in order to increase the amount of solar irradiation received unless multiple air distributors are used. Furthermore, the wall cavity containing the bed must be carefully sealed to prevent moisture or other foreign matter from entering the bed and to prevent the loss of bed particles.

Conventional flat-plate collectors, on the other hand, despite their proven performance and versatility have had significant historical problems. Liquid collectors have suffered from corrosion, freeze damage, outgassing of volatile materials, condensation beneath and between glass covers, rain water leakage, separation of parts, thermal distortion, charring and burning [28]. Air collectors have suffered from some of these same problems and are inherently at a disadvantage due to the low heat transfer coefficient of air and the higher air pumping power requirements.

Conventional collectors also offer little or no insulating value during periods of non-operation. The fluidized bed collector would serve as a good insulator when defluidized. As described in Chapter 4, the materials used in this investigation are all typically used in lightweight or insulation applications. In the defluidized state, the effective bed thermal conductivity is primarily a function of the entrapped gas within the bed. As such, a defluidized bed of the Norton or Macro materials would have a R value of approximately 6 hr-ft^2-°F/Btu while Perlite would have

a slightly larger value. These values compare very well with typical commercial wall insulation R values of 3-5 hr-ft^2-°F/Btu. Additionally, the good insulating property of the defluidized bed would aid in preventing freeze-ups during power failures.

In summary, then, the experimental results of this work indicate that the use of a fluidized bed as a flat-plate solar collector appears to be a viable concept. Its thermal performance generally falls in between that of typical liquid and air-cooled conventional collectors. Air pumping power requirements are expected to be less than that required for an air collector, and water pumping power requirements less than what is required for a liquid collector. The pressure drops associated with the greater density Norton and Macro test materials, though, present a probable structural problem for the wall containing the fluidized bed. During off-hours the defluidized bed would serve a dual role as the wall cavity insulation.

It must be re-emphasized, however, that the comparison between a fluidized bed solar collector and a conventional liquid-cooled and air-cooled flat-plate collector conducted in this section represents a comparison of only one of several possible vertical, active flat-plate solar collector designs. The particular design used in this section was chosen as a representative one that also made the best use of the available data on the fluidization and heat transfer of low density materials. Other possible designs, such as reducing the air gap from 4 inches to a smaller value and using a roughened collector surface for the air-cooled collector, could be considered. However, for an accurate comparison the fluidized bed solar collector design should similarly be changed to reflect the reduce

gap and roughened collector surface design changes. To date, data on the effect of varying gap width and roughened wall surfaces on the fluidization and heat transfer of low density materials is not available. In the next section, though, the heat transfer associated with air flow over a smooth and roughened heat exchange surface is compared with the results of the wall heat transfer of the experimental fluidized bed work. This comparison could give some initial insight into the effect of roughening an air-cooled collector surface and how it compares with the fluidized bed.

7.2 Heat Exchanger Applications

Another area of potential interest in the applications of low density material fluidization and heat transfer is in a heat exchanger configuration. This concept again involves the use of a building wall cavity as a fluidized bed. In this application, however, the bed would serve as an energy diffuser rather than an energy concentrator, as in the fluidized bed solar collector application. The wall containing the fluidized bed could serve a dual function for use in either a building space heating or cooling scheme. In both cases, the fluidized bed characteristic of being isothermal during fluidization would be utilized.

The space heating scheme would consist of using the fluidized bed to transfer heat from either an outside solar collector plate (in the case of an exterior wall), from hot water/steam passing through immersed heat transfer tubes, or from electric resistance heaters. In this configuration, the fluidized bed would, due to its isothermallity, yield a relatively constant temperature wall surface. The wall temperature could be maintained at a comfortable level by controlling the incoming heat flux to the bed and/or the bed operation, and, due to its surface area, still

provide a significant heat flux to the space to be heated. The concentrated incoming heat flux would have to be controlled in such a manner to overcome the appropriate thermal resistances at the heat source and through the bed. Thus, in this application the critical resistance to heat flow which effects the maintenance of a constant desired wall temperature is at the wall itself, R_w .

Table 7.6 lists the wall heat transfer coefficients ($h_w = 1/R_w$) of this investigation's test materials obtained from the experimental data. In this table a comparison is made between the test materials in a fluidized bed and air flowing over a smooth flat plate, in the form of the air pumping power requirement per unit surface area, for the same heat transfer coefficient. As can be seen by these results, the fluidized bed generally requires less power for the same heat transfer than air alone; the Perlite and optimum materials require significantly less. If, for example, Perlite 250 was fluidized in a wall cavity, the wall surface temperature maintained at 80°F, and the fluidization velocity adjusted to yield a wall heat transfer coefficient of 9.5 Btu/hr-ft^2-°F, a heat flux of 760 Btu/hr-ft^2 would be transferred from the wall into the space to be heated. Also, as with the solar collector application, the materials within the wall when defluidized would serve as effective heat insulation.

A building space-cooling scheme would operate similar to that of the space-heating one. In this case, however, when cooling is desired, such as at night, heat transfer would take place from the heated interior wall panel, through the bed, and to either an immersed heat transfer tube or to the cooler exterior panel. Again, to insulate from the heat transfer the bed would be defluidized. Contrary to the solar collector application,

TABLE 7.6 A COMPARISON OF POWER REQUIRED FOR A FLUIDIZED BED AND AIR FLOW OVER A SMOOTH FLAT PLATE FOR EQUAL HEAT TRANSFER

MATERIAL	h_{wall} [Btu/hr-ft^2-°F]	$(P/A)_{air}$ [HP/ft^2]	$(P/A)_{FB}$ [HP/ft^2]
Norton 650	10.0	2.2×10^{-3}	1.4×10^{-3}
	14.6	8.1×10^{-3}	1.8×10^{-3}
Norton 1	13.1	5.5×10^{-3}	3.4×10^{-3}
	14.4	7.8×10^{-3}	4.2×10^{-3}
Norton 1.5	11.8	3.9×10^{-3}	3.8×10^{-3}
	13.0	5.3×10^{-3}	4.6×10^{-3}
Macro M40X	11.0	3.0×10^{-3}	5.3×10^{-3}
	15.0	9.0×10^{-3}	6.4×10^{-3}
Macro M27X	10.9	2.9×10^{-3}	4.2×10^{-3}
	12.7	5.0×10^{-3}	4.9×10^{-3}
Perlite 250	8.7	1.3×10^{-3}	7.8×10^{-6}
	9.5	1.8×10^{-3}	9.9×10^{-6}
Perlite 500	6.2	4.0×10^{-4}	5.5×10^{-6}
	7.1	6.6×10^{-4}	6.7×10^{-6}
"Optimum"	11.0	3.0×10^{-3}	3.3×10^{-4}

these applications best suit the use of Perlite-like materials due to their low fluidization power requirements, bed pressure drops, and still increased surface heat transfer coefficients than air flowing over a flat plate.

Another area of interest related to the heat exchanger applications, and mentioned in the last section, concerns the comparison of the thermal performance of the fluidized bed to that of air over a roughened surface. Han, et al. [34] have conducted extensive work on the heat transfer and friction power requirements of air through rib-roughened parallel plates of constant heat flux. Table 7.7 compares the results of the fluidized bed wall heat transfer to that of Han's results for air flowing at 0.8 lbs/sec through a roughened duct of the same geometry as the air-cooled solar collector described in Section 7.1. As indicated in these results, roughening the surface over which air flows increases its heat transfer and also the associated friction power requirement. Under these conditions, the air heat transfer coefficient begins to approach that of the Perlite's but the power requirement is approximately two orders of magnitude greater. Thus, it would again appear that use of a Perlite type material in a fluidized bed, in which only the wall resistance to heat flow was of concern, would generally perform better than just using air.

TABLE 7.7 A COMPARISON OF HEAT TRANSFER COEFFICIENT AND POWER REQUIREMENT FOR A FLUIDIZED BED AND AIR FLOW THROUGH RIB-ROUGHENED PARALLEL PLATES

MATERIAL	h_{wall} (1)	(P/A) (2)	U_0 (3)
Air (roughened surface)	5.2	3.8×10^{-4}	8.0
Norton 650	14.6	1.8×10^{-3}	0.67
Norton 1	14.4	4.2×10^{-3}	1.7
Norton 1.5	13.0	4.6×10^{-3}	2.1
Macro M40X	15.0	6.4×10^{-3}	2.1
Macro M27X	12.7	4.9×10^{-3}	2.9
Perlite 250	9.5	9.9×10^{-6}	.02
Perlite 500	7.1	6.7×10^{-6}	.03

NOTE: Units are: (1) [Btu/hr-ft^2-°F]

(2) [HP/ft^2]

(3) [fps]

CHAPTER 8

CONCLUSIONS AND RECOMMENDATIONS

In this work the fluidization and heat transfer characteristics of low density particles in a fluidized bed have been investigated. Seven groups of particles ranging in diameter from approximately 250 μm to 2mm and density of 2.5 to 32 pcf have been used for all studies. It has been shown that these materials can be successfully fluidized and that their fluidization behavior can be fairly accurately predicted using the Geldart materials classification. Exceptions to this exist, however, for materials that exhibit significant triboelectric effects. Additionally, theoretical expressions for determining minimum fluidization velocities (Eq. 2.3) and bed pressure drops (Eq. 2.2) do well in predicting the actual values for these low density materials. It has also been shown, though, that not all low density particles can be fluidized for a variety of reasons (inter-particle forces, static-electric attraction).

The model of heat transfer that has been developed using significantly denser materials than those of this work (Eq. 2.7) has also been shown to do well in predicting the overall heat transfer coefficient from a heated surface to a bed of low density fluidized particles. However, it cannot be applied with confidence to a finned surface without knowing the effect the presence of the fins have on the material's fluidization. Despite this uncertainty, though, the use of fins does significantly increase the rate of heat transfer to the fluidized bed and a good estimate of the overall heat transfer coefficient can be made using Glicksman's "30/50 Rule".

The results of the heat transfer studies have also indicated that particle density is a larger controlling factor in heat transfer than

particle diameter. Density has a significant input in the emulsion component, h_e , of the overall heat transfer coefficient, which, in turn, has been shown to be the controlling component. Particle diameter, on the other hand, plays a dominant role in fluidization velocities, but due to the inherently low velocities required for the fluidization of these materials enters into the heat transfer as a secondary contributor.

The potential for additional heat transfer enhancement has also been studied through the use of air flow obstructions placed in the bed. It is hoped that the placement of obstructions would break up large bubble formations and thereby reduce particle-to-surface residence times. Initial results show that heat transfer coefficients may be increased up to 30% at moderate to high U/U_{mf} levels through the use of obstructions.

Using the results of the low density material fluidization and heat transfer studies, this work has additionally investigated the feasibility of using a fluidized bed of low density particles as part of a building's efficient energy management program. Two applications have been discussed: integrating a fluidized bed into a building wall cavity to serve as a "flat-plate" solar collector and to serve as a heat exchange medium.

In the solar collector application the thermal efficiency of a fluidized bed solar collector can be expected to fall in between that of comparable conventional liquid and air cooled flat plate solar collectors. Exceptions to this exist when very low density material (Perlite of this investigation) is used in the fluidized bed. This material has a large resistance to heat transfer through the fluidized bed due to its low density and fluidization velocities (see Eqs. (7.7) and (7.9)).

Additionally, the fluidized bed solar collector, using all the test materials, requires less water pumping power than the liquid-cooled

collector for the same heat transfer to the water and significantly less complex plumbing requirements. Similarly, the fluidized bed solar collector, using all test materials, requires less air pumping power than an air-cooled collector operating at normal conditions (air velocity of 8 fps) and provides the added benefit of having a more versatile and easily transportable energy stream (heated water in a tube versus heated air in a duct). The fluidized bed solar collector during non-operation also acts as effective wall insulation in contrast to conventional collectors.

However, the Norton and Macro materials used in this work pose potential wall structural problems. Due to their density they create significant pressure drops that may be impractical for use in a building wall cavity. Thus, because of the Perlite's poor thermal performance and the Norton and Macro's excessive wall pressures an "optimum" material having a density of approximately 10 pcf and a diameter of 0.5 mm (yet to be identified) has been described and analyzed for use in this application. This material, in theory, shows both good thermal and wall pressure results.

In the heat exchanger application the wall containing the fluidized bed could serve a dual function for use in either a building space heating or cooling program. In this application the use of a Perlite-like material would be most appropriate due to its low density (thus low wall pressures), low fluidization velocities (thus low air pumping power requirements), and because the critical resistance to heat transfer in this application is at the wall surface, h_w .

Finally, Chapter 1 noted that little work has previously been done on the use of low density particles in a fluidized bed and the potential applications of such use. This investigation has attempted to answer some

of the questions surrounding this topic. Although it appears that low density particle fluidization generally follows the same theoretical fluidization and heat transfer processes as greater density particles do and that feasible applications of this technology do exist, many questions still remain unanswered.

This work has only identified nine groups of low density particles for testing in which seven were extensively used. It is necessary that future work be conducted on other low density materials to develop further experimental data. Initially, it is recommended that the earlier described "optimum" material be identified and tested. At this introductory stage the "optimum" material possesses the greatest potential for successful applications.

Additional fluidization and heat transfer studies also need to be conducted using varying bed and heating geometries. The results of this investigation are based upon tests conducted only using the fluidized beds and heaters described in Chapter 4. These results have then been assumed to remain constant in order to be applied to the solar collector and heat exchanger applications. This assumption, although reasonable, must be verified through experimental means in order to determine its validity and to further determine optimum conditions for low density particle fluidization and heat transfer. It is recommended, for example, that tests be conducted using varying finned tube geometries. These tests would assist in understanding the effect the presence of fins have on fluidization and would produce further data available for selecting an optimum finned tube geometry for a particular application. Similarly, additional testing on the effect of air flow obstructions, roughened fluidized bed wall surfaces, and varying bed depths should be conducted to

aid in the understanding and optimization process of low density particle fluidization.

An additional area requiring more research, which is of particular importance to the applications discussed in this work, is the fluidized bed thermal resistance determination. The theoretical model used in Chapter 7 (Eq. 7.7) is based upon an effective heat conduction path length that is a function of immersed heat transfer tube spacing (Eq. 7.8) and an effective thermal conductivity (Eq. 7.9). Recently, though, it has been suggested that a more realistic model expressing this resistance should be based upon a path length that is a function of the average bubble diameter rising through the bed [41]. If this is so, it can be expected that the average bubble length may be less than the length represented by Eq. (7.8) and result in an increased bed resistance than that which was originally predicted. The magnitude of this increase will determine what procedures should be taken to decrease this resistance or totally re-evaluate the feasibility of the applications considered in this work.

Consequently, the initial successes observed in this investigation must be tempered by the knowledge that many more questions exist. Not until these topics, and any further ones they in turn may generate, are resolved will a full understanding of low density particle fluidization and heat transfer with successful applications be realized.

REFERENCES

[1] DECKER, N., "Heat Transfer to Horizontal Tubes in Large Particle Gas Fluidized Beds", unpublished Ph.D. Thesis, Dept. of Mechanical Engineering, M.I.T., 1983.

[2] ERGUN, S., Chem. Eng. Progr., 48, p. 89, 1952.

[3] KUNII, D. and LEVENSPIEL, O., Fluidization Engineering, Krieger Publishing Co., Huntington, N.Y., 1977.

[4] DAVIDSON, J. and HARRISON, D., eds., Fluidization, Academic Press, New York, 1971.

[5] GELDART, D., Fluid-Bed Heat Transfer, J. Botterill, Academic Press, New York, pp. 12-15, 1975.

[6] GLICKSMAN, L., "Heat Transfer in Fluidized Bed Combustors", unpublished, M.I.T., 1983.

[7] MICKLEY, H. and FAIRBANKS, D., "Mechanisms of Heat Transfer to Fluidized Beds", AIChE J., 1, p. 374, 1955.

[8] BOTTERILL, J., BUTT, M., CAIN, G., and REDISH, K., "The Effect of Gas and Solid Thermal Properties on the Rate of Heat Transfer to Gas Fluidized Beds", Int. Symp. on Fluidization, A. Drinkenburg, ed., Netherlands University Press, Amsterdam, pp. 442-57, 1967.

[9] DUNSKY, V., ZABRODSKY, S., and TANIARIN, A., "On the Mechanism of Heat Transfer Between a Surface and a Bed of Moving Particles", Proc. 3rd Int. Heat Transfer Conf., Vol. 4, AIChE, pp. 193-297, 1966.

[10] BASKAKOV, A., "The Mechanism of Heat Transfer Between a Fluidized Bed and a Surface", Int. Chem. Eng., 4, pp. 320-24, 1964.

[11] GELPERIN, N. and EINSTEIN, V., "Heat Transfer in Fluidized Beds", in [4].

[12] GLOSKI, D., "An Experimental Study of the Transient Particle-Wall Thermal Contact Resistance in Fluidized and Packed Beds", unpublished S.M. Thesis, Dept. of Mechanical Engineering, M.I.T. 1982.

[13] CHEN, J. and WITHERS, J., "An Experimental Study of Heat Transfer from Plain and Finned Tubes in Fluidized Beds", 15th National Heat Transfer Conference, AIChE Paper No. 34, 1975.

[14] BARTEL, W. and GENETTI, W., "Heat Transfer from a Horizontal Bundle of Bare and Finned Tubes in an Air Fluidized Bed", AIChE Symposium Series 69, No. 128, pp. 85-93, 1973.

[15] PETRIE, J., FREEBY, W., and BUCKHAM, J., "In-Bed Heat Exchangers", Chemical Engineering Progress 64, pp. 45-51, 1968.

[16] GENETTI, W. and KNUDSEN, J., Chemical Engineering Progress Symposium Series 30, No. 147, 1968.

[17] GLICKSMAN, L., Personal Communication, 1984.

[18] ROHSENOW, W. and CHOI, H., Heat, Mass, and Momentum Transfer, Prentice-Hall, Englewood Cliffs, N.J., 1961.

[19] LEARY, W. and TSAI, D., "Metering of Gases by Means of the ASME Square-Edged Orifice with Flange Taps", Unpublished, M.I.T., 1951.

[20] ANDEEN, B., "Heat Rejection from Horizontal Tubes to Shallow Fluidized Beds", Unpublished Ph.D. Thesis, Dept. of Mechanical Engineering, M.I.T., 1974.

[21] DECKER, N., "Heat Transfer to Horizontal Tubes in a Fluidized Bed", Unpublished S.M. Thesis, Dept. of Mechanical Engineering, M.I.T., 1978.

[22] 3M Company, St. Paul, Minnesota, P.O.C.: Ronald L. Adalbert, Marketing Supervisor, Business Development Life Sciences Sector, Ph. (612) 733-1154.

[23] Norton Company, Worcester, MA, P.O.C.: David Rostoker, Assistant Director R&D, Ph. (617) 853-1000.

[24] Whittemore Perlite Company, Inc., Reading, MA., P.O.C.: Andrew Barten, Sales Representative, Ph. (617) 942-1333.

[25] Dynatech Research and Development Co., Cambridge, MA., P.O.C.: Andre Desjarlais, Technical Director, Thermoinsulation Evaluation, Ph. (617) 868-8050.

[26] RABINOWICZ, E., An Introduction to Experimentation, Addison-Wesley, Reading, MA., 1970.

[27] Q-Cell 200 Spherical Fillers, Manufactured by The PQ Corporation, Valley Forge, PA., P.O.C.: Tom Ruth, Sales Representative, Ph. (215) 293-7448.

[28] LÖF, G. and KARAKI, S., "System Performance for the Supply of Solar Heat", Mechanical Engineering 12, pp. 32-47, 1983.

[29] JORDAN, R. and LIU, B., eds., Applications of Solar Energy for Heating and Cooling of Buildings, American Society of Heating, Refrigerating, and Air Conditioning Engineers, ASHRAE GRP 170, 1977.

[30] KREITH, F. and KREIDER, J., Principles of Solar Engineering, Hemisphere Publishing Corp., Washington, D.C., 1978.

[31] GLICKSMAN, L., "Class Notes: 2.65J Fluidization", unpublished, M.I.T., 1983.

[32] MALIK, M. and BUELOW, F., "Heat Transfer in a Solar Heated Air Duct - A Simplified Analysis", in Heliotechnique and Development, (COMPLES 1975), Vol. 2, pp. 31-37, Development Analysis Assoc., Cambridge, MA.

[33] BROOKS, G., ECONOMIDES, L., and WINCKOWSKI, B., "Building Systems Engineering", Engineering Manual, McGraw-Hill, N.Y., p. 4-4, 1976.

[34] HAN, J., GLICKSMAN, L., and ROHSENOW, W., "An Investigation of Heat Transfer and Friction for Rib-Roughened Surfaces", Int. Journal of Heat and Mass Transfer 21, pp. 1-14, 1978.

[35] MOORE, A., ed., Electrostatics and Its Applications, John Wiley & Sons, N.Y., N.Y., 1973.

[36] POSTRIKOV, S., Electrophysical and Electrochemical Phenomena in Friction, Cutting, and Lubrication, Van Nostrand Reinhold, N.Y., N.Y., 1978.

[37] HARPER, W., Contact and Frictional Electrification, Oxford University Press, 1967.

[38] HARPER, W., "How Do Solids Become Charged?", Static Electrification, pp. 3-10, May 1967.

[39] SEARS, F. and ZEMANSKY, N., University Physics, Addison-Wesley, Reading, MA., 1970.

[40] ECKERT, E. and DRAKE, R., Analysis of Heat and Mass Transfer, McGraw-Hill, N.Y., N.Y., 1972.

[41] GLICKSMAN, L., Personal Communication, 1985.

APPENDIX A

WALL HEATER HEAT BALANCE AND INSULATION DIMENSIONS

This appendix details the analysis taken in determining the necessary insulation required to be placed around the wall heater to insure that the heat flux generated is transferred into the two-dimensional fluidized bed. Figure A-1 depicts a schematic cross-sectional view of the wall heater in which a heat balance analysis is conducted.

From symmetry and the geometry of the heater the following equalities exist:

$$q_{top} = q_{bottom}$$

$$q_{side\ 1} = q_{side\ 2}$$

$$A_{bed} = A_{back} = 1.5 \text{ in.} \times 6 \text{ in.} = .063 \text{ ft}^2$$

$$A_{top} = A_{bottom} = 1.5 \text{ in.} \times 0.25 \text{ in.} = .003 \text{ ft}^2$$

$$A_{side\ 1} = A_{side\ 2} = 6 \text{ in.} \times 0.25 \text{ in.} = .01 \text{ ft}^2$$

An energy balance around the heater yields

$$q_{in} = q_{bed} + q_{back} + q_{top} + q_{bottom} + 2q_{side} \qquad \text{(A-1)}$$

where

$$q_{bed} = h_{bed} A_{bed} (T_{wall} - T_{bed})$$

$$q_{back} = k_{styrofoam} A_{back} (T_{wall} - T_{amb.}) / \ell_{styrofoam,back}$$

$$q_{top} = k_{styrofoam} A_{top} (T_{wall} - T_{amb.}) / \ell_{styrofoam,top}$$

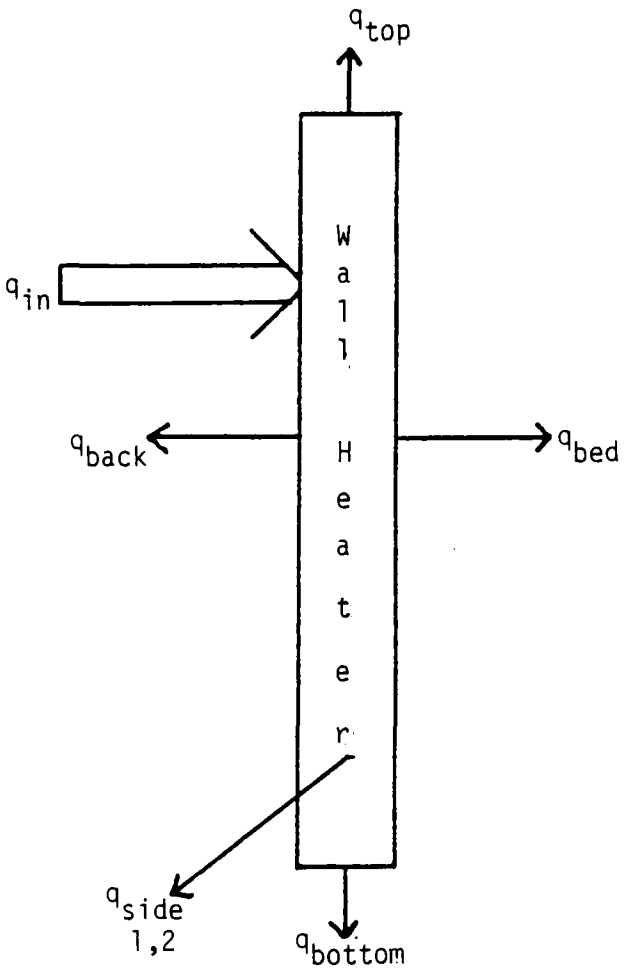

FIGURE A.1 Wall Heater Heat Balance

$$q_{bottom} = k_{rubber} A_{bottom}(T_{wall} - T_{amb.})/ \ell_{bottom}$$

$$q_{side} = k_{styrofoam} A_{side}(T_{wall} - T_{amb.})/\ell_{styrofoam,side} \cdot$$

To insure that $q_{bed} \cong q_{in}$ it is necessary to require that the remaining terms in Eq. (A-1) are negligible compared to q_{bed}. Thus,

(i) $\frac{q_{bed}}{q_{back}} >> 1$ or let $\frac{q_{bed}}{q_{back}} = 100$

$$\frac{q_{bed}}{q_{back}} = \frac{h_{bed} A_{bed}(T_{wall} - T_{bed})}{k_{styrofoam} A_{back}(T_{wall} - T_{amb.})/\ell_{back}} = 100$$

$$\ell_{back} = \frac{100(k_{styr.}) A_{back}(T_{wall} - T_{abm.})}{h_{bed} A_{bed}(T_{wall} - T_{bed})} \qquad (A\text{-}2)$$

(ii) $$\frac{q_{bed}}{q_{top}} = \frac{h_{bed} A_{bed}(T_{wall} - T_{bed})}{k_{styr.} A_{top}(T_{wall} - T_{amb.})/\ell_{top}} = 100$$

$$\ell_{top} = \frac{100(k_{styr.}) A_{top}(T_{wall} - T_{amb.})}{h_{bed} A_{bed}(T_{wall} - T_{bed})} \qquad (A\text{-}3)$$

$$\text{(iii)} \quad \frac{q_{bed}}{q_{bottom}} = \frac{h_{bed}\, A_{bed}(T_{wall} - T_{bed})}{k_{rubber}\, A_{bottom}(T_{wall} - T_{amb.})/\ell_{bottom}} = 100$$

$$\ell_{bottom} = \frac{100(k_{rubber})\, A_{bottom}(T_{wall} - T_{amb.})}{h_{bed}\, A_{bed}(T_{wall} - T_{bed})} \qquad \text{(A-4)}$$

$$\text{(iv)} \quad \frac{q_{bed}}{q_{side}} = \frac{h_{bed}\, A_{bed}(T_{wall} - T_{bed})}{k_{styr.}\, A_{side}(T_{wall} - T_{amb.})/\ell_{side}} = 100$$

$$\ell_{side} = \frac{100(k_{styr.})\, A_{side}(T_{wall} - T_{amb.})}{h_{bed}\, A_{bed}(T_{wall} - T_{bed})} \qquad \text{(A-5)}$$

Assumed values of $(T_{wall} - T_{amb.})/(T_{wall} - T_{bed}) = 5$, $h_{bed} = 20$ Btu/hr-ft^2-°F, $k_{styrofoam} = 0.02$ Btu/hr-ft-°F and $k_{rubber} = 0.09$ Btu/hr-ft-°F used in conjunction with Eqs. (A-2) through (A-5) yield the required insulation thicknesses:

$\ell_{back} = 0.5$ ft $= 6.0$ in

$\ell_{top} = 0.024$ ft $= 0.29$ in

$\ell_{bottom} = 0.11$ ft $= 1.29$ in

$\ell_{side} = 0.16$ ft $= 0.95$ in

APPENDIX B

FIN ANALYSIS FOR FINNED TUBE HEATER

This appendix details the particular characteristics of the fins used on the finned tube heater. These fins are circumferential fins of rectangular cross-section and the procedure used in analyzing these fins is outlined in reference [40].

As illustrated in Fig. 4.5 each fin has an outer radius, x_e, of 0.094 ft., an inner radius, x_b, of 0.031 ft, and a thickness, $2y_b$, of 0.0017 ft. The total fin area available for heat transfer may be calculated using

$$A_{fin} = (\text{No. of fins})(2 \text{ sides})\ \pi[x_e^2 - x_b^2] \qquad \text{(B-1)}$$

$$= 13\ (2)\pi\ [(.094)^2 - (.031)^2]$$

$$= 0.64\ ft^2$$

In order to determine the fin efficiency the term $\ell\sqrt{h/ky_b}$ has to be determined where:

$\ell = x_e - x_b$

$h = 10$ Btu/hr-ft^2-°F (Assumed, based on results of unfinned tube data.)

$k = 220$ Btu/hr-ft-°F for copper fins

$y_b = 0.00085$ ft.

Using these values,

$$\ell\sqrt{h/ky_b} = 0.46 \tag{B-2}$$

and

$$\frac{x_e}{x_b} = \frac{.094}{.031} \cong 3 \tag{B-3}$$

yields, from reference [40], a fin efficiency of approximately 0.90.

Further, to determine the finned tube heat transfer coefficient the results of a heat balance around the finned tube may be utilized

$$q_{total} = q_{bare\ tube} + q_{fin}$$

$$= h\, A_{bare\ tube}\, \Delta T + h\, \eta_{fin}\, A_{fin}\, \Delta T$$

$$q_{total} = h\, \Delta T[A_{bare\ tube} + (\eta A)_{fin}] \tag{B-4}$$

assuming that the heat transfer coefficient of the bare tube and the fins is approximately equal. From Eq. (B-4) and substitution of the known area and calculated efficiency values an expression for the heat transfer coefficient can be obtained

$$h = \frac{q_{total}}{(0.644)\Delta T} \tag{B-5}$$

Equation (B-5) is used in this experiment to determine the finned tube heat transfer coefficients.

APPENDIX C

THE THEORY OF STATIC CHARGING

In Chapters 5 and 6 the observance of electrostatic charging of the Perlite and styrofoam materials in contact with plexiglas was discussed. This appendix will outline, in general terms, the phenomena of electrostatic charging between two materials and what measures can be taken to reduce this effect. This discussion will aid in developing a better understanding of the phenomena as observed in this investigation and for future work with similar materials in fluidized beds.

The subject of electrostatic charging, frictional electricity, or "triboelectric charging" has a history of having been long recognized but not well understood. The production of electric charges that occurs when two solids are rubbed together (static cling of clothing for instance), the electrification of liquids such as gasoline when they are poured out of a container, the formation of charged droplets in spraying, and the attraction of the Perlite and styrofoam materials to the plexiglas bed wall are all examples of triboelectric charging of materials.

It has long been recognized that if two dissimilar metals are placed in contact there will be a potential difference between the metals. This is because electrons will find it easier to go from one metal to another. This potential difference between the metals is called the contact potential. If the two metals are then carefully separated one will be positively charged and the other negatively. The potential difference between

the metals will be at most 3 to 4 volts, but is usually around 2 volts [35]. Similarly, if two electrically nonconducting materials, insulators or dielectrics, are brought together they may also become charged. If a tangential mechanical force acts on the boundary of the contacting materials, the force must overcome, among other things, the electric attraction between the two dissimilar materials for motion occur. As a result of this motion the two materials become tangentially separated. A small, but finite, fraction of the total mechanical work expended is spent in producing the electrostatic energy of the separated charges. This electrostatic energy is called frictional electricity. It has generally been accepted that the process of material charging through contact and friction with another material is all considered triboelectric charging.

In general, conductors and insulators, when electrically isolated from the earth, can easily become charged as a result of interacting with another material. Friction may be involved, or just contact followed by separation.

Metals can transfer electrons from one surface to another based upon the metal's Fermi energy level. When two dissimilar metals are placed in contact, there will be a transfer of electrons from one to the other until the potentials of the metals are such that the Fermi levels are aligned. It is necessary to give electrons an amount of energy equal to the material's work function in order for them to escape from the material's surface. Consequently, the potential difference established between two metals is the difference in work functions. Electrons are transferred through the interface from the material with the lower work function to that with the higher work function. This mechanism of charge redistribution generally holds for metal-to-metal, metal-to-semiconductor

and semiconductor-to-semiconductor contact situations. However, for dielectrics, such as Perlite, styrofoam and plexiglas, there appears to be some uncertainty and conflict of opinion concerning the mechanism of their triboelectric charging.

Postnikov has postulated that in contact of a metal and a dielectric charging is due to the transfer of electrons from the metal to the dielectric and the transfer of positive or negative ions from the dielectric to the metal [36]. Whereas in the contact of two dielectrics charging results from the diffusion of "charge carriers" from one substance to another.

Harper, on the other hand, has suggested a more detailed account of the static charging mechanism of dielectrics [37,38]. He agrees that the transfer of ions plays an important role in the charging of solids, but emphasizes those mobile ions that have been formed through electrolytic dissociation in the surface films of moisture on solids. He suggests that there is a rupture of a double diffusional layer of electrolytic ions in the thin water film between two contacting dielectrics or between a metal and a dielectric that is responsible for the charging of the surfaces once they are parted from one another.

He additionally categorizes dielectrics into two classes. The first class consists of "electrophilic" dielectrics which acquire strong charges through contact with metal. These include glass, fused quartz, and magnesium oxide. The second class consists of "electrophobic" dielectrics. These materials take on a negligible charge when in contact with metal. This class includes polyethylene, polystyrene, nylon and Perlite. The observed discharging of electrophilic dielectrics and charging of electrophobic dielectrics when in contact with metal is a result of

electrolytic and greasy surface contamination. Harper states that as greasy (electrophobic) contamination is accumulated on an electrophilic dielectric the charge will decrease. Similarly, accumulation of electrolytic contamination on an electrophobic dielectric will increase its charge. He further considers the electrophilic/electrophobic character as an intrinsic, inherent property of a dielectric.

This conclusion seems well founded. According to classical electrostatic theory, the greater a material's ability to polarize the greater its ability to be charged and transfer that charge [39]. The extent to which a dielectric becomes polarized when in an electric field is a function of an intrinsic material property called its susceptibility, χ A dielectric coefficient, K , is defined as

$$K = 1 + \chi \qquad (C.1)$$

The larger a material's susceptibility, the greater is its ability to be polarized. Consequently, materials with a larger value of the dielectric coefficient will be polarized easier than those with a smaller value. Table C.1 is a listing of various materials and their corresponding dielectric coefficient value. Note that water, a good conductor, has a high K value whereas air, a poor conductor, has a low one. As identified through experimentation by Harper and shown in Table C.1, glass (electrophilic, K = 5-10) is more capable of being charged when brought in contact with a metal than polyethylene (electrophobic, K = 2.25). A similar electrophobic result was observed in this investigation with the Perlite and styrofoam contacting the metal walls and heater surface.

TABLE C.1 DIELECTRIC COEFFICIENT, K [39]

MATERIAL	K
VACUUM	1.00
AIR	1.0006
TEFLON	2.1
POLYETHYLENE	2.25
BENZENE	2.28
HEVEA RUBBER	2.94
VINYLITE	3.18
PLEXIGLAS	3.40
MICA	3-6
BAKELITE	5.50
GLASS	5-10
NEOPRENE	6.70
GERMANIUM	16
LIQUID AMMONIA	25
GLYCERIN	42.5
WATER	78.54

At this point it would appear that triboelectric charging results from various configurations of material contact charging alone. However, it has repeatedly been observed, such as in this investigation, that when certain materials are rubbed together they become electrically charged. Therefore, some mechanism must account for this and two hypotheses are commonly used to explain it.

One answer to the rubbing or "friction" question that has been proposed is the Volta-Helmholtz hypothesis [37]. This hypothesis also attributes all triboelectrification to contact. It states that the virtue of rubbing, however, is only to multiply the points of material contact. When two materials are brought together, initial contact is made. When the materials rub together, old contacts are broken and new ones are made.

Another theory accounting for frictional electrification is through material transfer [37]. When material is transferred from one surface to another via friction the material will be removed from asperities on the surface from which it comes. This material may not necessarily be typical of the surface as a whole and, in the case of a metal, may then have a different contact potential from the rest of the surface. This transferred material could, therefore, carry with it an electric charge to the other surface. If the material transferred comes from a dielectric hot spot created during frictional rubbing it may have lost electrons to the less hot material left behind and thus carry an electric charge to the new surface.

Thus, the mechanisms of triboelectrification presently understood entail some combination of contact and frictional effects. Depending upon the materials involved, their geometry, physical and electrical properties, state of cleanliness, nature of interaction, etc. one or both of these

processes may be controlling. Due to this variety of variables there is no universal, single criteria or relationship for determining "a priori" how much actual electricity is generated triboelectrically under known conditions between two materials in any situation. Numerous experiments have been conducted in search of this relationship, success being only in developing one that satisfies the particular conditions, materials, and controls of that experiment.

However, enough is known about this phenomenon in order to minimize its effect, if desired. As discussed earlier, electrically conducting materials have a large dielectric coefficient value. Thus, metallic fluidized particles, for example, would be expected to exhibit very little static electric problems in fluidized bed operations. Problems would be expected, on the other hand, if the bed walls were made of an electrophyllic material, such as glass. Similarly, electrophobic fluidized particles would be expected to exhibit little static electric problems in a bed made with metallic walls. In this investigation, problems occurred because electrophobic fluidized particles, Perlite and styrofoam, were in a bed that had an electrophobic material wall, plexiglas. Triboelectric charges were built up on the dielectrics, due to contact and friction, that were unable to be sufficiently transferred away. It is further suspected that the styrofoam has a lower K value than the Perlite since it exhibited the strongest triboelectric effect with the plexiglas.

In some engineering or laboratory applications it may be impractical to construct a fluidized bed or specify particular particles in order to reduce the triboelectric attraction phenomena. In these instances, applying the theory can again be helpful. For example, increasing the relative humidity of or using static neutralizers with radioisotopes in the

fluidizing air would substantially increase its dielectric coefficient value. Thus the fluidizing air may become conductive enough to control the accumulation of triboelectric charges. Adding special electrically conductive fillers, using commercially available antistatic preparations, or simply providing an electrical path to drain off charges on the dielectrics would aid in increasing their electrical conductivities.

In summary, this appendix has attempted to briefly discuss the general aspects of triboelectrification of solid materials. The mechanisms involved in this process are a combination of electrostatic charging due to contact and friction between two materials. There appears to be no definite agreement on the exact mechanism that explains triboelectric charging other than it is a function of the materials' characteristics involved, the environment in which they are contacted, their geometry and the nature of their contact.

Yet, despite this lack of knowledge of the exact mechanism involved, enough is known to satisfactorily prevent the effect of triboelectric charging. Additionally, as a result of experimentation and experience with triboelectricity certain general relationships or "laws" have been developed and are summarized in Table C.2.

TABLE C.2 SOME "LAWS" OF TRIBOELECTRICITY [36]

CONTACTING MATERIALS	SIGN OF CHARGE	
	+	-
Dielectric and fine particles of the same dielectric	Dielectric	Particles
Dielectric and Dielectric	Dielectric with with higher susceptibility	Lower susceptibility
	Harder Dielectric	Softer Dielectric
Metal and Dielectric	Dielectric	Metal
Metal and Metal	Lower Work Function	Higher Work Function
	Softer Metal	Harder Metal

APPENDIX D

SQUARE EDGED ORIFICE DATA

This appendix outlines the procedure used in determining the air velocity through the fluidized beds of this experiments. Two ASME square edged orifices with flange taps are utilized in making this determination. The specific orifice plate data presented here are based upon the general guidelines listed in reference [19].

The equation for the flow rate of a gas through the ASME square-edged orifice meter with flange taps is

$$\omega = 0.1145\, D_2^2\, K\, Y \left(\frac{P_1}{T_1} G_y \Delta P \right)^{1/2} \qquad \text{(D-1)}$$

where

ω = mass flow rate [lbm/sec]

D_2 = orifice diameter [in.]

K = flow coefficient

Y = expansion factor

P_1 = static pressure before orifice [in. H_g absolute]

T_1 = temperature before orifice [°R]

G = specific gravity of gas (air = 1.00)

y = supercompressibility factor

ΔP = pressure drop across orifice [in. H_2O]

Table D-1 lists the values obtained from reference [19] of these parameters for orifice A and orifice B.

PARAMETER	ORIFICE A	ORIFICE B
D_2	0.3	0.6
K	0.6056	0.6050
Y	0.99	0.99
P_1	to be measured	to be measured
T_1	to be measured	to be measured
G	1.0	1.0
y	1.0	1.0
ΔP	to be measured	to be measured

TABLE D-1 Orifice Parameter Value for Flow Rate Equation

Knowing that the air mass flow rate through the orifice can also be expressed as

$$\omega = \rho U_0 A \qquad \text{(D-2)}$$

where

ρ = density of the air at T_1 ($\rho \cong 0.075$ lbm/ft^3 for the operating conditions of this experiment)

U_0 = air velocity

A = cross-sectional area of a fluidized bed

yields a relationship for calculating the air velocity through the fluidized bed

$$U_0 = \left(\frac{0.1145\ D_2^2\ K\ Y}{\rho\ A} \right) \left(\frac{P_1}{T_1}\ G\ y\ \Delta P \right)^{1/2} \qquad \text{(D-3)}$$

Using the values listed in Table D-1, Eq. (D-3) can be modified for orifice A and orifice B use in the two-dimensional or three-dimensional fluidized bed. Table D-2 shows these modifications.

	ORIFICE A	ORIFICE B
Two-Dimensional Bed	$U_0 = 0.733 \left(\frac{P_1}{T_1} \Delta P \right)^{1/2}$	$U_0 = 2.86 \left(\frac{P_1}{T_1} \Delta P \right)^{1/2}$
Three-Dimensional Bed	(not used)	$U_0 = 1.317 \left(\frac{P_1}{T_1} \Delta P \right)^{1/2}$

TABLE D-2 ORIFICE PLATE VELOCITY EQUATIONS

APPENDIX E

TEST MATERIAL MINIMUM FLUIDIZATION VELOCITY RESULTS

This appendix presents, in both graphical and tabular form, the results of the test material's minimum fluidization velocity determination experiments. These experiments were conducted according to the procedure outlined in Chapter 5. The average U_{mf} for each particle is defined as the arithmetic mean of the two-dimensional and three-dimensional fluidized bed U_{mf} values. This average value is used in all of the analysis in Chapter 6 and in the applications of Chapter 7. Figures E.1 through E.7 illustrate the experimental results and Tables E.1 through E.7 list the tabulated results. Also, note from Figures 4.1 and 4.2 that all bed pressure readings are based on a pressure tap height of 8 in. for the two-dimensional bed and 4 in. for the three-dimensional bed.

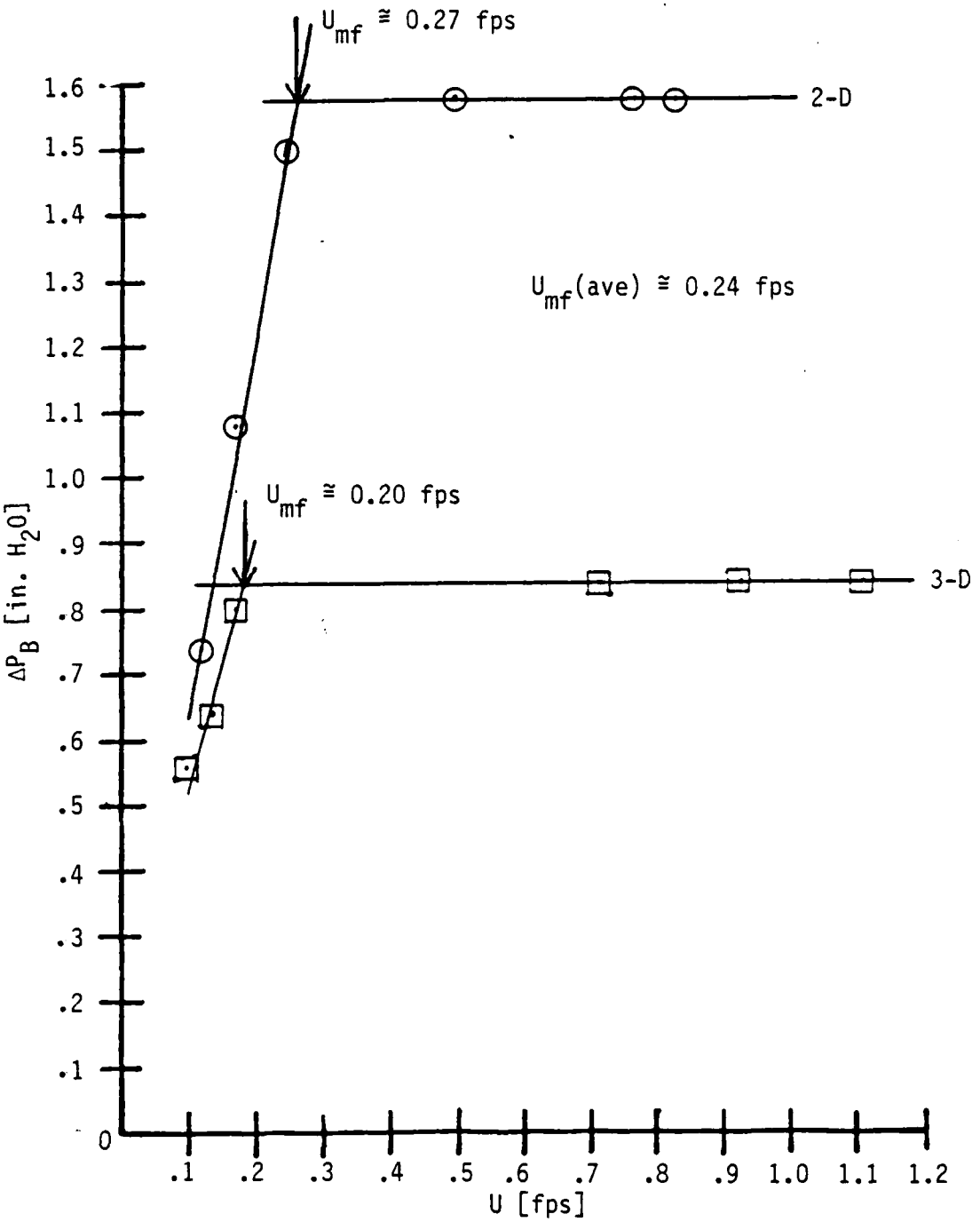

FIGURE E.1 Norton 650 U_{mf} Determination

TABLE E.1 NORTON 650 U_{mf} DATA

	ΔP_B [in. H_2O]	U [fps]
2-D Bed:	0.74	0.12
	1.08	0.17
	1.50	0.25
	1.59	0.50
	1.58	0.77
	1.58	0.83
3-D Bed:	0.56	0.10
	0.64	0.10
	0.80	0.17
	0.84	0.72
	0.84	0.93
	0.84	1.11

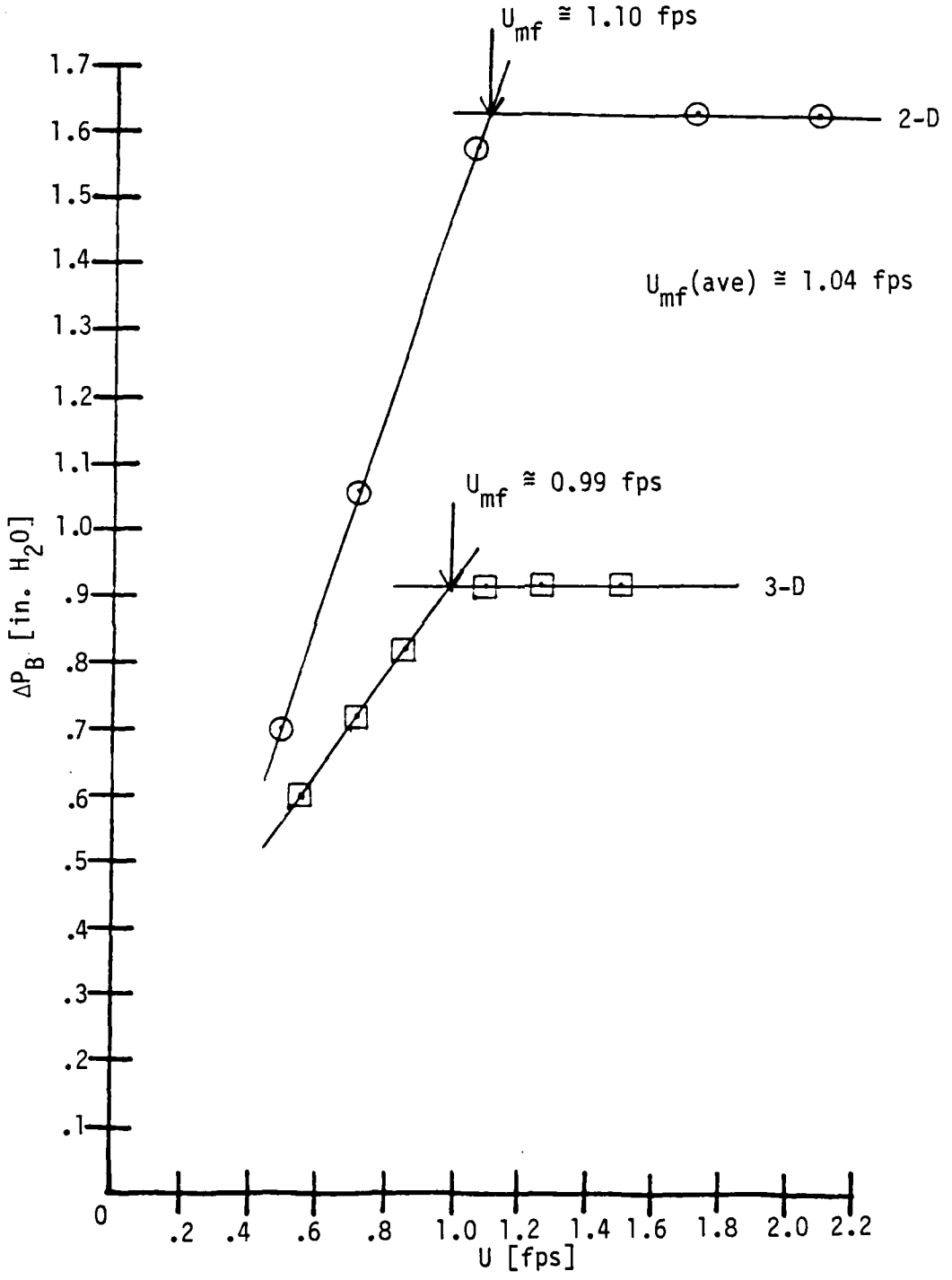

FIGURE E.2 Macro M40X U_{mf} Determination

TABLE E.2 MACRO M40X U_{mf} DATA

	ΔP_B [in. H_2O]	U [fps]
2-D Bed:	0.70	0.50
	1.06	0.72
	1.58	1.06
	1.65	1.71
	1.64	2.08
3-D Bed:	0.60	0.55
	0.72	0.72
	0.82	0.86
	0.92	1.10
	0.92	1.26
	0.92	1.50

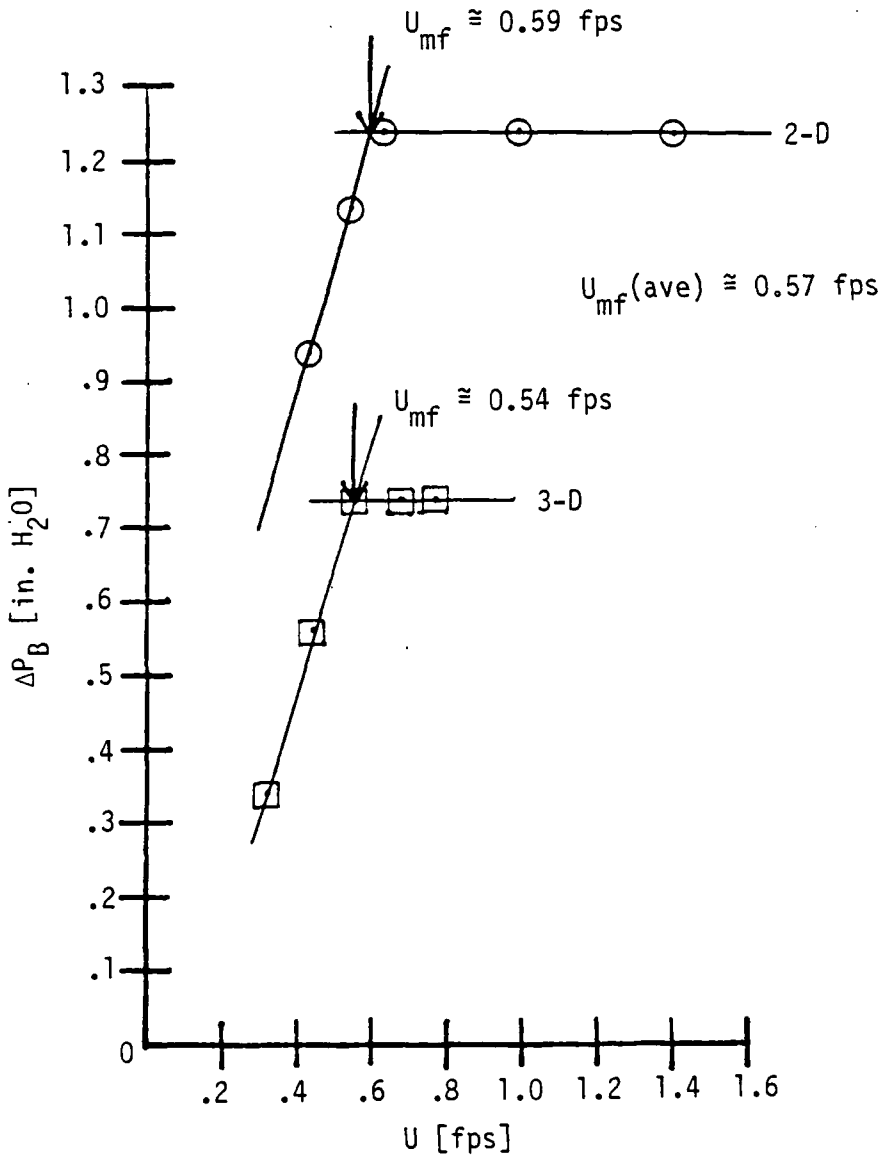

FIGURE E.3 Norton 1 U_{mf} Determination

TABLE E.3 NORTON 1 U_{mf} DATA

	ΔP_B [in. H_2O]	U [fps]
2-D Bed:	0.94	0.43
	1.14	0.54
	1.24	0.63
	1.25	0.98
	1.24	1.40
3-D Bed:	0.34	0.32
	0.56	0.44
	0.74	0.54
	0.74	0.68
	0.74	0.78

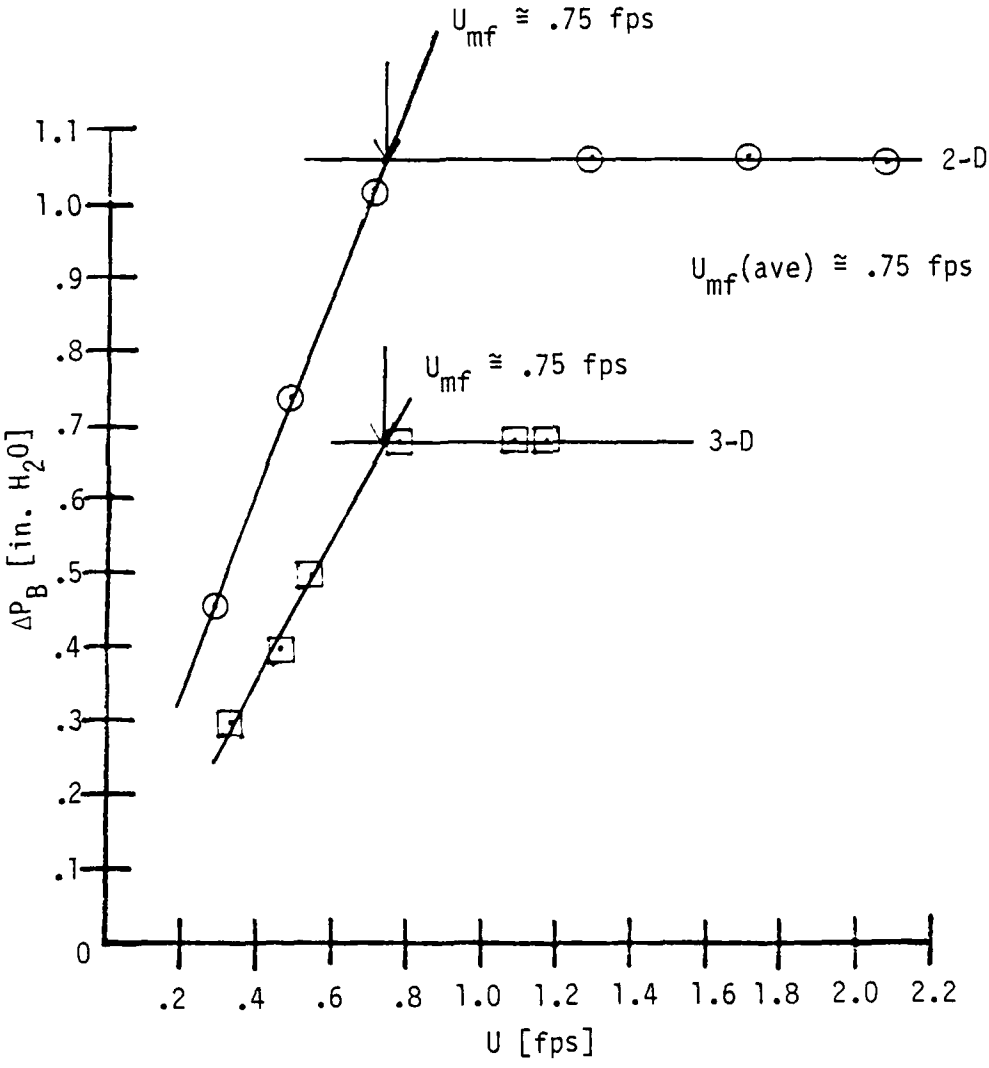

FIGURE E.4 Norton 1.5 U_{mf} Determination

TABLE E.4 NORTON 1.5 U_{mf} DATA

	ΔP_B [in. H_2O]	U [fps]
2-D Bed:	0.46	0.30
	0.74	0.50
	1.02	0.72
	1.06	1.30
	1.07	1.71
	1.06	2.08
3-D Bed:	0.30	0.34
	0.40	0.48
	0.50	0.55
	0.68	0.79
	0.68	1.10
	0.68	1.18

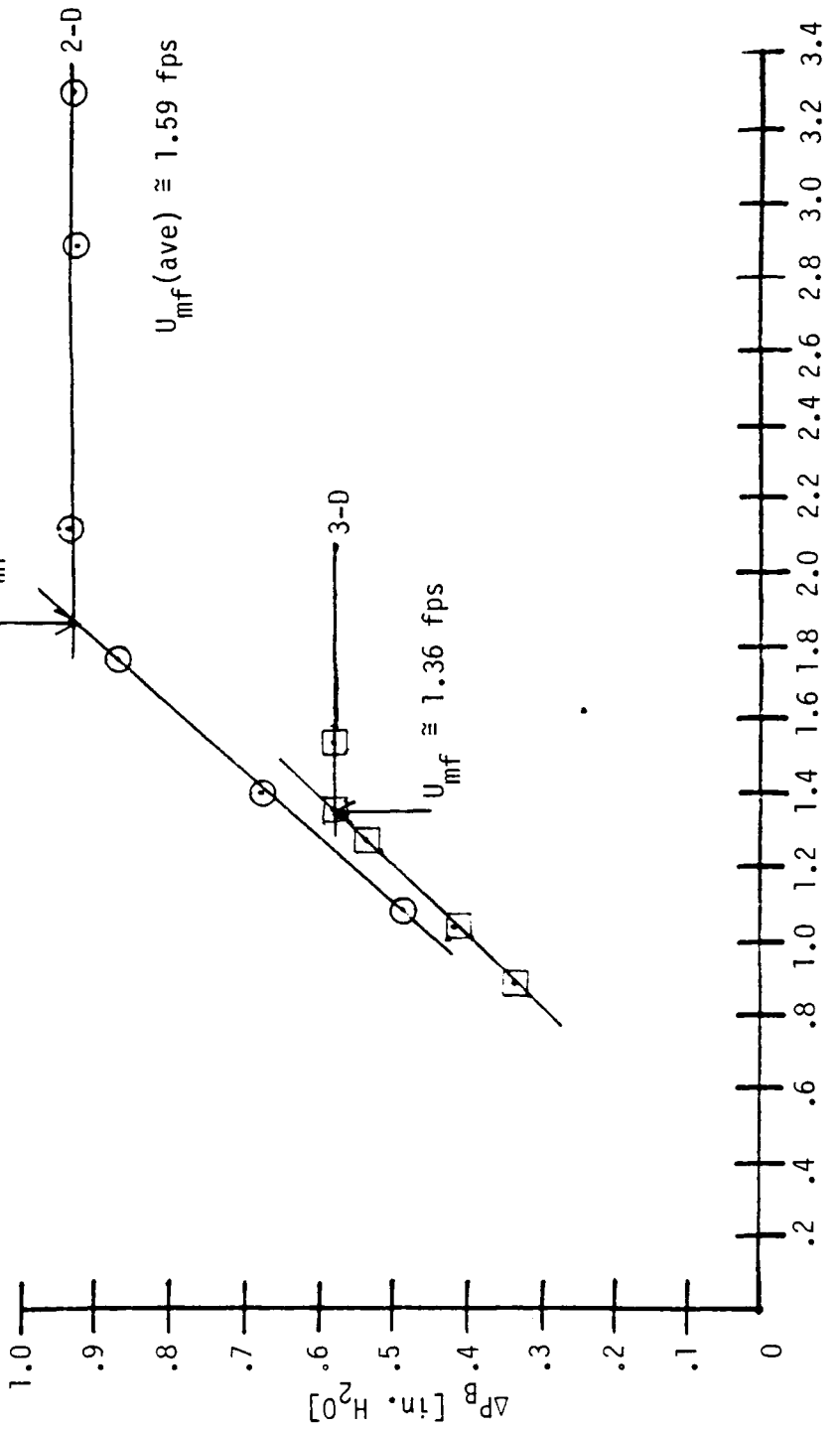

FIGURE E.5 Macro M27X U_{mf} Determination

TABLE E.5 MACRO M27X U_{mf} DATA

	ΔP_B [in. H_2O]	U [fps]
2-D Bed:	0.49	1.09
	0.68	1.41
	0.87	1.78
	0.94	2.13
	0.92	2.90
	0.93	3.32
3-D Bed:	0.34	0.89
	0.42	1.04
	0.54	1.28
	0.58	1.36
	0.58	1.54

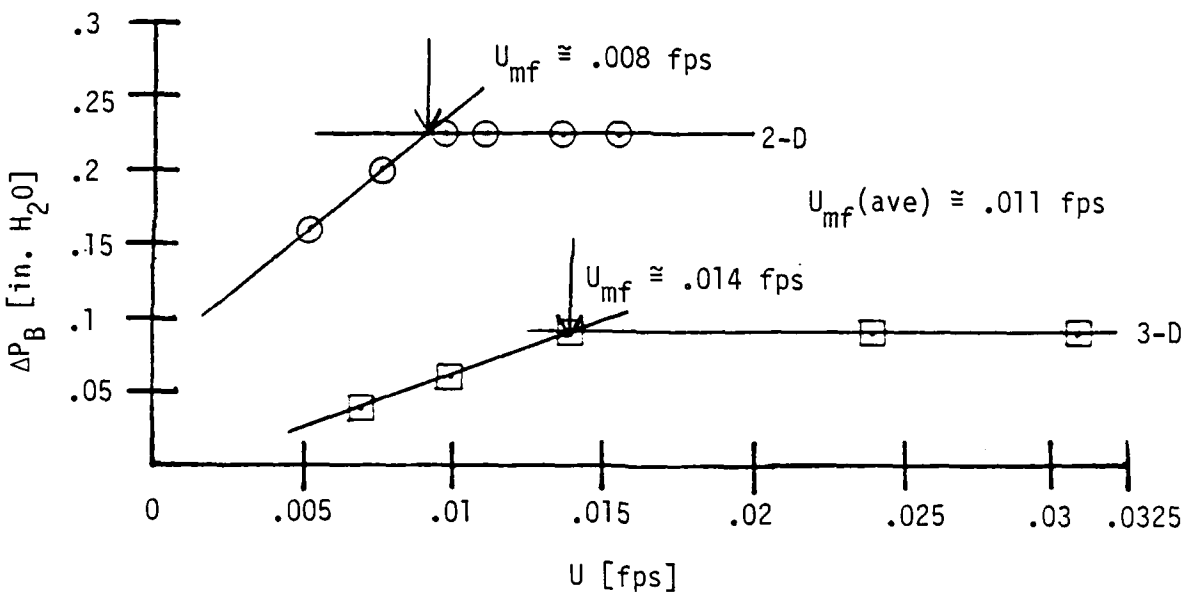

FIGURE E.6 Perlite 250 U_{mf} Determination

TABLE E.6 PERLITE 250 U_{mf} DATA

	ΔP_B [in. H_2O]	U [fps]
2-D Bed:	0.16	.0051
	0.20	.0076
	0.25	.0095
	0.25	.011
	0.25	.014
	0.25	.0155
3-D Bed:	0.045	.007
	0.051	.010
	0.095	.014
	0.095	.024
	0.095	.031

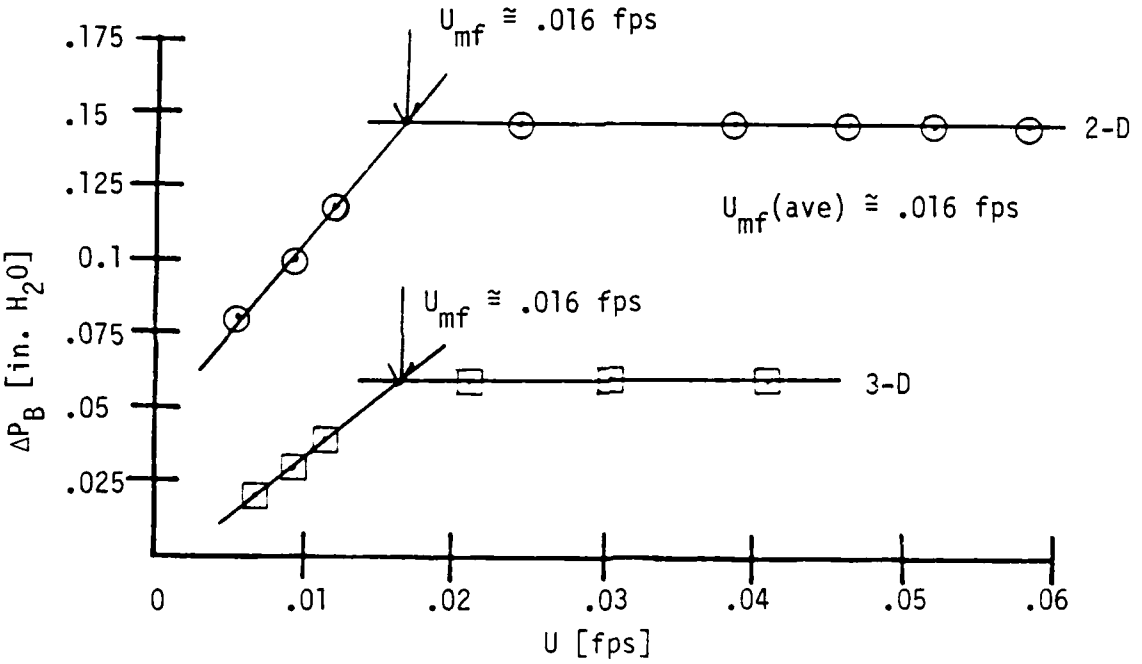

FIGURE E.7 Perlite 500 U_{mf} Determination

TABLE E.7 PERLITE 500 U_{mf} DATA

	ΔP_B [in. H_2O]	U [fps]
2-D Bed:	0.076	.0052
	0.10	.0095
	0.12	.011
	0.149	.0245
	0.149	0.038
	0.149	0.046
	0.149	0.052
	0.149	0.058
3-D Bed:	0.02	0.007
	0.03	0.0095
	0.04	0.012
	0.065	0.021
	0.065	0.031
	0.065	0.042

END

FILMED

8-85

DTIC